Development of a coherence-based transmissometer for the removal of scattering bias

PhD Thesis

A. Gribbon

Experimental Quantum Optics and Photonics Group
Marine Optics and Remote Sensing Group
Department of Physics
University of Strathclyde, Glasgow

Submission Date: 04/06/2026

Abstract

The measurement of the beam attenuation coefficient by transmissometers has long been negatively affected by the presence of errors due to the collection of light scattered at small forward angles. The magnitude of these errors is difficult to predict and account for, relying on characteristics of the transmissometer, such as the path length and collection angle, and also on the parameters describing the particle population, like the particle size distribution and refractive index, among other terms. This makes accounting for the errors in beam attenuation associated with scattered light very challenging. Researchers have focused on developing corrections for the beam attenuation coefficient after measurement. However, these approaches require further knowledge about the water sample, such as the volume scattering function. This thesis introduces the design of a novel, coherence transmissometer that utilizes the loss of spatial coherence associated with particle scattering to measure an increased beam attenuation coefficient compared to that measured by a standard transmissometer design that uses only a lens and pinhole. After optimization of the coherence transmissometer for sensitivity to various noise sources, it is found that combining the lens–pinhole arrangement with a coherence filter produces consistently higher attenuations values than a transmissometer that only uses a lens–pinhole arrangement for a range of polystyrene microspheres and spherical phytoplankton from approximately 1 to 50 µm. The difference in beam attenuation measurements between the two transmissometers increases with increasing particle size, as expected due to changes in the volume scattering function, and is reasonably consistent with expectations of the scattering errors from Mie scattering simulations at low particle sizes. These results suggest that the use of a coherence filter should be further explored for inclusion in future transmissometer designs, to substantially reduce the effect of scattering errors on beam attenuation measurements.

Acknowledgements

Although I enjoyed the research work of this thesis and discovered a love for working on the instrumentation side of science which I hope to continue to take forward with me into my future endeavours, the research process, and particularly the writing process, is never easy. I would like to thank all of the people who helped me to get to the finish line and made the process more enjoyable along the way.

To my supervisors, Griff and David, for their wise supervision and constant support through the development of the thesis. You pushed me to question and justify my work throughout, which endlessly frustrated me and also made me a much better scientist. In particular, I want to thank you both for supporting me and nurturing my love of research over many projects together since the start of my time at Strathclyde and for giving me the opportunity to do a PhD in something I loved.

To Cait, Ru, and Håkon, for their friendship and support, useful discussions about scattering, and for being a great group of fellow researchers to share an office and also some pints with.

To my good friends, Shannan, Mimi, and Gavin, for being there throughout the years to rant and cry to, problem solve with, and to remind me to forget about work and just enjoy life as much as possible.

To Rach, for always making me laugh and always being ready with an escape plan when I needed it. To Carolyn, for holding me up and making sure I never took it.

Finally, to Malcolm, for always being by my side, supporting me through the entire process, from Honour’s to PhD, across continents, and making sure I remembered how much I love the science even when it’s tough.

Contents

List of Figures

List of Tables

List of Acronyms

AOPs: Apparent Optical Properties

HWP: Half Wave Plate

IOCCG: International Ocean Colour Coordinating Group

IOPs: Inherent Optical Properties

LED: Light Emitting Diode

LISST: Laser In-Situ Scattering and Transmissometry

ND: Neutral Density

nPBS: non-Polarizing Beam Splitter

OAM: Orbital Angular Momentum

PSICAM: Point Source Integrating Cavity Absorption Meter

PBS: Polarizing Beam Splitter

SLM: Spatial Light Modulator

SPP: Spiral Phase Plate

UV: Ultraviolet

VSF: Volume Scattering Function

List of Symbols

α: standard error

$\beta(\Psi; \lambda)$: spectral volume scattering function

$\tilde{\beta}(\Psi; \lambda)$: volume scattering phase function

θ_c: standard transmissometer collection angle

θ_i: angle of incidence

θ_r: angle of diffraction

Θ: beam divergence

Δr: unit distance

ΔV: unit volume

σ: standard deviation

cov_{AB}: covariance between variables A and B

ε: random error in a given variable

Ψ: scattering angle

ρ_{AB}: correlation coefficient between A and B

ω: angular frequency

φ: relative phase of a wave

λ: wavelength

$\hbar$: reduced Planck’s constant

v: speed of light in a medium

A: wave amplitude

$A(\lambda)$: spectral absorptance

$B(\lambda)$: spectral scatterance

$a(\lambda)$: spectral absorption coefficient

$b(\lambda)$: spectral scattering coefficient

c: speed of light in vacuum

$c(\lambda)$: beam attenuation coefficient

$D(\lambda)$: spectral absorbance

d: Young’s double slit spacing

ξ: range of particle sizes in Mie modelling

ξ_{peak}: central particle size in Mie modelling

d_0: dimension of coherence area

DR: signal dynamic range

$DoLP$: degree of linear polarization

$E_{\mathrm{i}}(\Psi)$: incident irradiance

f: focal length

f_{c}: scattering error due to finite collection angle

g: asymmetry parameter for scattering functions

I: transmitted light intensity

I_0: incident light intensity

$I_{\mathrm{s}}(\Psi; \lambda)$: scattered intensity

I_{TOT}: total scattered intensity

k: wave number

l: OAM mode number

m: relative refractive index

n: refractive index in medium

p: diffraction order

Q: extinction efficiency

Q_{b}: total scattering efficiency

Q_{bb}: backscattering efficiency

r_{pinhole}: pinhole radius

r_{sphere}: sphere radius in particle modelling

R: ratio between c_{COH} and c_{STD}

S: calibrated voltage signal for changes in intensity of laser

$S_1(\vec{\theta})$, $S_2(\vec{\theta})$: scattering wave amplitude functions

t: time

T: wave period

$U(\mathbf{r}, \mathrm{t})$: description of a propagating wavetrain across spatial dimensions $\mathbf{r}$ and at a given time t

V_{COH}: voltage measured by the coherence transmissometer

V_{REF}: reference voltage for intensity corrections during transmissometry measurements

V_{STD}: voltage measured by the standard “lens-and-pinhole” transmissometer

x: spatial dimension in 1D

z: path length

Chapter 1: Introduction to the scattering problem

Understanding and accurately measuring underwater light propagation is vital for understanding key processes in the ocean. Light scattering and absorption provide key information regarding oceanic constituents, allowing measured changes in light propagation to be linked to cycles of phytoplankton behaviour, sediment analysis (Agrawal & Mikkelsen, 2009), and carbon dissolution in the ocean (Coble et al., 1990), among others. For example, understanding the distribution of light in underwater environments is important for understanding ecosystem dynamics which exhibit light-driven behaviour, such as the daily migration of zooplankton in response to light (Häfker et al., 2022).

The beam attenuation coefficient is an important parameter of interest in ocean waters for a variety of applications, measuring the amount of light attenuated after passing through a region of interest with a given path length. For example, the beam attenuation coefficient is an important input parameter for radiative transfer modelling, which describes the relationship between the underwater light field and the measurable optical constituents of the water (Mobley, 1994). Measurements of the beam attenuation coefficient can also be used as a proxy for measurements of phytoplankton biomass which is relatively stable to changes in light levels, nutrients, and temperature (Behrenfeld & Boss, 2006). Measurements of the spectral beam attenuation coefficient can also be used to determine the particle size distribution in natural waters, which in turn is important for understanding ecological dynamics and predicting sediment flux and transport (Boss et al., 2001).

For decades, the standard method for measuring the beam attenuation coefficient has utilized a design known as a direct-path transmissometer (Figure 1).

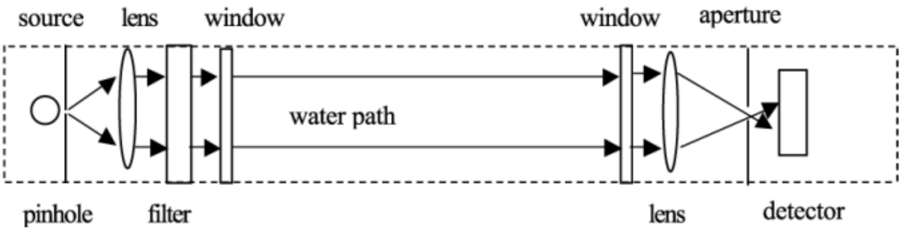

Figure 1: View of a standard direct-path transmissometer from IOCCG Protocol on beam transmission and attenuation (Boss et al., 2019).

The fundamental concept underlying the use of a direct-path transmissometer is the use of a focusing lens and a pinhole to block off light scattered at large angles from reaching a detector. This device calculates the attenuation coefficient for a given path length through the device, z, as follows:

$$I = I_0 e^{-c(\lambda)z}, \tag{1}$$

where I is the transmitted light intensity, I_0 is the initial light intensity, $c(\lambda)$ is the wavelength-dependent beam attenuation coefficient, and z is the path length through the sample.

The beam attenuation coefficient is composed of components due to light scattering and light absorption along the beam path. Direct-path transmissometers are limited in their measurement of the attenuation due to scattering along the beam path due to their finite collection angle, θ_c, defined by the geometry of the lens, pinhole, and detector in a given device, alongside the refractive index of the medium, as follows.

$$\theta_c = \sin^{-1}\left[\frac{1}{n}\sin\left[\tan^{-1}\left(\frac{r_{\text{pinhole}}}{f}\right)\right]\right], \tag{2}$$

where n is the refractive index of the medium, typically taken to be that of water ($n = 1.33$), r_{pinhole} is the radius of the pinhole, and f is the focal length of the lens (Boss et al., 2009). The above equation assumes that the pinhole is placed at exactly the focal length of the lens and that the optical set-up is in air ($n = 1$).

The finite collection angle of the transmissometer cannot be brought to zero, with commercial values typically on the order of 1°, allowing forward-scattered light at angles within this collection angle to reach the detector and influence the attenuation measurement. The collection of scattered light by the detector results in the beam attenuation coefficient being systematically underestimated in these devices. The magnitude of scattering error introduced by the non-zero collection angle is not easily quantified or corrected for. It is dependent on multiple parameters such as the collection angle, path length, and particle characteristics, such as the size, shape, structure, and refractive index of the particles. However, it is generally accepted that there is a substantial and ever-present scattering bias introduced to the measurement of beam attenuation by the finite collection angle of the transmissometer. Accurate reporting of the beam attenuation coefficient cannot be achieved without accounting in some way for this bias.

Despite recent advances towards developing correction algorithms for the scattering error (McKee et al. 2013), the issue of scattering errors remains a key problem that does not have a universally agreed-upon solution. In fact, as per the IOCCG Protocol on "Beam Transmission and Attenuation Coefficients: Instruments, Characterization, Field

Measurements and Data Analysis Protocols", the official advice for addressing scattering errors in beam attenuation measurements is to not tackle them at all, and to simply state the device characteristics and acknowledge their effect on the attenuation, as follows:

"*One approach to dealing with the effects of scattered light in measured beam attenuation coefficients is that proposed by both Voss and Austin (1993) and Pegau et al. (1995). That is, do not try to apply any scattering corrections to the measured determination of c(λ). Simply report the acceptance angle characteristics of the transmissometer used to make the measurements and leave all considerations of how to handle scattering artifacts to the user of the data.*" – IOCCG Protocol Series Volume 2.0, 2019 (Boss et al., 2019).

There is a strong need for novel solutions to the collection of scattered light in transmissometers in order to produce unambiguous and accurate measurements of the beam attenuation coefficient (Boss et al. 2019).

Throughout the discussion of scattering errors, the majority of approaches have focused on the correction of beam attenuation estimates after the initial measurements with a direct-path transmissometer, requiring the further measurement of other optical parameters such as the volume scattering function to achieve an accurate beam attenuation value. To the best of our knowledge, solutions to these scattering errors that suggest a redesign of the direct-path transmissometer have not been seriously considered. Development of a new transmissometer design that can account for the collection of scattered light as a feature of its design in order to make more accurate beam attenuation measurements would provide a simpler and more elegant solution to current approaches, removing the need for additional optical measurements and potentially facilitating greater uptake by researchers in the field.

The aim of this thesis research is to develop and test a novel transmissometer design that is capable of overcoming the systematic underestimation of beam attenuation due to the collection of scattered light. The scheme involves utilizing the change in spatial coherence that occurs as a result of scattering at the particle sizes typical in natural waters, which has so far been almost completely unexploited, with direct-path transmissometers only accounting for the change in light direction on scattering. This thesis proposes the use of a diffraction grating that acts as a filter for the degradation of spatial coherence that occurs due to light scattering, in addition to the changes in light direction currently accounted for by the lens and pinhole set-up.

The structure of this thesis is as follows. Chapter 2 will discuss the relevant theory to this research, including an overview of the beam attenuation and scattering coefficients in natural waters, transmissometers and the nature of the forward-scattering problem, the spatial coherence properties of light, and how these properties have been utilized thus far and can be developed to address the collection of scattered light in transmissometers. Chapter 3 will cover the proposal and development of an initial prototype transmissometer design using a diffraction grating as a spatial coherence filter to reduce the collection of scattered light in attenuation measurements. Chapter 4 will discuss the further development of this initial transmissometer design, covering the identification of noise terms in the attenuation measurements and their reduction. Finally, Chapter 5 will present the final coherence-based transmissometer design and characterise its performance for polystyrene microspheres and spherical phytoplankton species over approximate size ranges from 1 to 50 micrometers. The potential contribution of coherently forward-scattered light to the attenuation measurements and how this transmissometer design (and that of other instruments) should be adjusted to account for this will also be discussed.

Chapter 2: Theory

This chapter will describe the key theory underlying the principles of transmissometry, interactions of optical fields with water, and the importance of spatial coherence to these measurements.

2.1. Inherent Optical Properties

The theory presented in this section follows the discussion of Mobley, Light and Water (Mobley, 1994).

The optical properties of a body of water can be described by the combination of the inherent optical properties (IOPs) and apparent optical properties (AOPs) of the volume of water. AOPs of the water volume describe all optical properties that are dependent on both the directional structure of the incident light field and the properties of the medium itself. On the other hand, IOPs are those properties that depend solely on the properties of the medium without being affected by the angular distribution of the light. Some examples of AOPs are the diffuse attenuation coefficient and the average cosines describing the symmetry of scattered light. Some examples of the IOPs include the absorption of the medium and the volume scattering function. A description of the absorption, scattering, and attenuation coefficients and how they are commonly measured in the marine optics community will be provided in the following subsections.

2.1.1. Absorption

The spectral absorptance ($A(\lambda)$) is the fraction of incident power absorbed within a given volume as a function of the incident field's wavelength. This should not be confused with the spectral absorbance ($D(\lambda)$), otherwise known as the optical density of the medium, which is the quantity measured by a spectrophotometer.

The spectral absorption coefficient (m^{-1}) is the spectral absorptance per unit distance in the medium:

$$a(\lambda) = \lim_{\Delta r \to 0} \frac{A(\lambda)}{\Delta r}, \tag{3}$$

where Δr is the distance over which the incident light is absorbed. A particular challenge for absorption measurements is the ability to remove or distinguish changes in the incident light field due to scattering in order to measure only the effects of absorption in the medium.

Absorption has commonly been measured using the filter pad method with a spectrophotometer, based on modifications of the technique proposed by Yentsch in 1962 (Yentsch, 1962). A sample is filtered to concentrate the particulate matter on a filter pad, then the spectral absorption is measured by recording the light transmitted through the matter on the pad. However, this can't account for the intense scattering that occurs through the dense particle layer on the filter pad which increases the apparent absorption by increasing the path length to the detector. Making accurate measurements of absorption using a filter pad technique requires the application of corrections to account for this change in path length, which may empirically depend on the particle type (Finkel and Irwin 2001; Lefering et al., 2016; Roesler 1998). Other errors associated with filter pad measurements include absorption by dissolved matter on the filter pad, decomposition of particles, and the loss of particles from the filter pad.

Alternate methods for measuring absorption have been proposed to improve upon filter pad-based techniques, such as reflecting tube absorption meters (W. H. Slade et al., 2010), but these still require a final scattering correction to obtain accurate absorption estimates (McKee et al., 2013; Röttgers et al., 2013). A solution for making absorption measurements without the need for any scattering correction exists in the form of an integrating cavity measurement, such as that made by the point-source integrating cavity absorption meter (PSICAM) (Röttgers et al., 2005). This approach uses a diffuse light source inside a spherical integrating cavity such that scattered light is reflected from the cavity walls repeatedly until either absorbed by the medium or measured as transmitted at the detector. This prevents the loss of scattered light from the measurement system that leads to the overestimation of absorption in other devices.

2.1.2. Scattering

The following discussion follows a combination of that of Light and Water, Mobley (Mobley, 1994) and the Ocean Optics web book (Mobley, 2020).

Where the spectral absorption coefficient (Eq. (3)) is the spectral absorptance per unit distance in the medium, the analogous spectral scattering coefficient is the spectral scattering per unit distance in the medium, i.e.:

$$b(\lambda) = \lim_{\Delta r \to 0} \frac{B(\lambda)}{\Delta r}, \tag{4}$$

where $B(\lambda)$ describes the proportion of the incident beam that is scattered out of the beam as it passes through the medium as a function of the incident field's wavelength, known as the spectral scatterance.

2.1.2.1 Volume scattering function

The spectral scatterance per unit distance and unit solid angle is the spectral volume scattering function. The spectral volume scattering function (VSF) ($\mathrm{m}^{-1}\mathrm{sr}^{-1}$) is the term given to the scattered intensity ($I_s(\Psi;\lambda)$) per unit incident irradiance ($E_i(\Psi)$) per unit volume of water (ΔV):

$$\beta(\Psi;\lambda) = \lim_{\Delta V\to 0}\frac{\mathrm{I}_s(\Psi;\ \lambda)}{\mathrm{E}_i(\Psi)\Delta \mathrm{V}}, \tag{5}$$

where λ is the wavelength of the incident light and Ψ is the scattering angle ($0 \leq \Psi \leq 90°$) with a scattering angle of 0° equivalent to no angular deviation from the incident light direction. This can also be thought of as the differential cross-section of scattered light per unit volume.

The spectral volume scattering function is linked to the spectral scattering coefficient $b(\lambda)$ as $b(\lambda)$ can be found by integrating the spectral volume scattering function over all solid angles, as follows:

$$b(\lambda) = 2\pi\int_0^{\pi}\beta(\varphi,\lambda)\sin\varphi\ d\varphi, \tag{6}$$

where $\beta(\varphi,\lambda)$ is the VSF at a given wavelength, λ, and scattering angle, φ, as defined above.

This calculation is relatively simple in the case of randomly oriented scatterers and an unpolarized light source. In the case of a linearly polarized light source, such as a laser, this calculation becomes more complex and must consider the Stokes vectors (Bickel & Bailey, 1985). The azimuthal symmetry of scattered light that is generally the case for unpolarized light scattering from an isotropic medium is broken in the case of a linear polarization direction, as the azimuthal scattering directions differ from the unpolarized case. The assumption of symmetric azimuthal scattering can also break down in the presence of an anisotropic medium, for both linearly polarized and unpolarized light. There are clearly multiple factors that can affect the symmetry of the volume scattering function. Other factors include the size of particles from which the light is scattered and the degree of scattering present in the system (Piskozub & McKee, 2011).

The volume scattering phase function, $\tilde{\beta}(\Psi;\lambda) = \beta(\varphi,\lambda)/b(\lambda)$, is the volume scattering function normalized by the scattering coefficient. Splitting the volume scattering function into these two terms provides us with a term describing only the angular distribution of the scattered light ($\tilde{\beta}(\Psi;\lambda)$) and another term describing only the magnitude of the scattered light ($b(\lambda)$). It is important to be aware of the difference in these terms, since some studies may describe changes to the volume scattering phase function alone and not account for magnitude changes. In this case, it would be a mistake to assume that the study also encompasses changes to the magnitude of scattered light.

The combined magnitude and angular distribution of scattered light is fundamentally important to the performance of the standard lens-and-pinhole arrangement used by commercial transmissometers. The magnitude of light scattered at small angles less than the collection angle of the transmissometer is an important factor in the scattering error recorded by transmissometers, and is given by the following equation:

$$f_c = 2\pi \int_0^{\theta_c} \tilde{\beta}(\varphi;\lambda) \sin\varphi \, d\varphi, \tag{7}$$

where $\tilde{\beta}(\varphi;\lambda)$ is the volume scattering phase function for angle φ and wavelength λ, and θ_c is the collection angle of the transmissometer. This can be understood as the amount of light that is able to pass through the directional filtering provided by a lens-and-pinhole set-up and thereafter be indistinguishable from transmitted light, leading to underestimates of the beam attenuation coefficient and variation in beam attenuation measurements depending on the collection angle used. This effect has been illustrated by the differences in beam attenuation coefficient that have been measured for a range of commercial transmissometers with different collection angles. For example, (Boss et al., 2009) observed that, for a range of different commercially available transmissometers with four different collection angles between them, the measured beam attenuation varied with the collection angle of the transmissometer. Instruments with smaller collection angles measure higher beam attenuations due to the variation in the amount of scattered light captured within a smaller angle. The exact values can vary depending on the path length and acceptance angle of the transmissometers used, alongside the water type, but this effect of higher attenuation for smaller acceptance angle is consistent. For example, in the above-referenced study of Boss et al. (2009), they report ratios of beam attenuation coefficient measurements for transmissometers with acceptance angles of 1.2° compared to those with angles of 0.0269° in one location that varied between 0.55 and 0.9 as a function of tidal variation. Other areas in the study reported different ratio values due to variations in the water type but in general showed the same behaviour where transmissometers with larger acceptance angles measured smaller attenuations.

One can understand that it is possible to see this change in measured beam attenuation by either changing the collection angle of the device to collect a wider angular distribution of scattered light, or by any effect that causes an increase in the magnitude component of the volume scattering function at the angular distribution of light captured by the device. Both actions effectively cause the same result, that is, more light passing through a pinhole to the measurement device. When making comparisons between transmissometers, it is important to keep in mind how the volume scattering function may interact with different device specifications and what sort of effects this may produce in the data.

The scattering coefficient $b(\lambda)$ can be determined by measuring the VSF of a given water volume and integrating over all solid angles. Although the measurement of the VSF is theoretically simple in the case of randomly oriented scatterers and an unpolarized light source, as discussed above, in practice it is difficult to design such an instrument due to the large dynamic range required. For example, the intensity of scattered light decreases by 5–6 orders of magnitude from $\Psi = 0.1°$ to $\Psi = 90°$ in natural waters, which are predominantly forward-scattering. Furthermore, for any given scattering angle Ψ, the expected scattering intensity can vary by up to two orders of magnitude in natural waters depending on the particle composition. Since there is a steep rate of change of the volume scattering function at small angles, small changes in alignment of the optics within the instrument are capable of producing a substantial change to the scattering measurements – a realistic problem for in-situ devices. Although these sensitivities to alignment are not quantified in the literature, they are generally accepted to be a limiting factor and often considered in the design of measurement devices (Boss et al., 2019). Historically, this limited the measurement of the volume scattering function *in-situ*. The LISST-VSF from Sequoia Scientific has allowed the measurement of the VSF from 0.1° to 150°, with earlier LISST products, such as the LISST-200X, measuring the VSF at smaller angular ranges < 13°. Performance evaluations of the LISST-200X and the LISST-VSF recommend *in-situ* usage alongside additional laboratory calibrations, although the LISST-VSF remains limited by multiple scattering errors (Sandven et al., 2020).

Due to limitations on measuring the VSF *in-situ*, the most common method for determining the scattering coefficient is via the relation between the beam attenuation, absorption, and scattering coefficients:

$$c(\lambda) = a(\lambda) + b(\lambda). \tag{8}$$

The absorption coefficient can be measured as described in Section 2.1.1.Absorption. Measurements of the beam attenuation coefficient will be discussed in the following section.

There are considered to be three categories of causes of scattering in natural waters. When the scale is << λ, scattering is attributed to density fluctuations associated with random molecular motions. When the scale is > λ, scattering is associated with large (i.e., with particle size parameters typically between 1 and 50 (Kidder & Vonder Haar, 1995)) organic and inorganic particles. For >> λ, changes in the real refractive index associated with turbulence cause scattering. At a minimum, scattering occurs from the water molecules (and salt ions for seawater) themselves. This small-scale scattering occurs due to changes in the molecular number density in a given encapsulated volume. This leads to changes in the refractive index across the water sample which causes scattering. In seawater, this effect is enhanced due to the addition of variations in the concentration of ions such as Cl^- and Na^+.

Changes in the scattering coefficient of natural seawaters are associated most strongly with changes in parameters such as particle concentration, the particle size distribution, the relative refractive index of the particles with respect to the medium, particle internal structure, and particle shape in the size regime of 0.1 to 10s of micrometers (Koestner et al., 2018). As such, several studies have measured the scattering coefficient at forward- and backward-scattering angles in order to determine useful particle characteristics, such as particulate organic carbon, particulate inorganic carbon, and suspended particulate matter (Babin et al., 2003; Koestner et al., 2022; Slade & Boss, 2015; Volten et al., 1998). Approximately half of all scattering in natural waters occurs at scattering angles below a few degrees, making the behaviour of the VSF at small angles very important for determining the scattering coefficient via the VSF. Furthermore, 69–83% of particulate scattering occurs at $\Psi < 15°$ (Petzold, 1972). In waters with particles of many different sizes, diffraction-dominated scattering occurs, meaning that the scattering is dominated primarily by the particle size rather than the shape or composition. This type of scattering is most prevalent at small forward angles (Jerlov, 1968).

Slade and Boss (2006) demonstrated that a LISST-100 (Laser In-Situ Scattering and Transmissometry) meter from Sequoia Scientific could be used to measure the shape and magnitude of the VSF at near-forward scattering angles. They developed a methodology for obtaining instrument-specific scaling factors for determining the VSF from the angular scattering data measured by the LISST-100, showing good agreement with Mie theory simulations. There have since been multiple studies focusing on the development and calibration of a further range of LISST-series devices for measuring angular scattering and the VSF (Agrawal and Mikkelsen 2009; Sandven et al. 2020).

All discussion so far of scattering in natural waters has been based on research that only considers the change in light direction due to scattering, i.e., changes to the volume scattering phase function. However, scattering events can result in a change of light direction, a change in the phase of the light, or both. In the case of scattering at 0°, where the light is scattered at an angle on-axis with the direction of propagation, the scattering event cannot be distinguished by a change in angle. However, the change in phase associated with scattering still occurs and can be measured. For a suspension of completely identical particles, scattering at 0° is considered to be coherent (Fry et al., 1992).

Fry, Padmabandu, and Choonghoon (1992) measured coherent scattering effects in the near-forward direction by designing a set-up that allowed separation of the transmitted beam from the scattered beam at 0°. The set-up utilized a photorefractive crystal in which beam fanning (otherwise known as asymmetric self-defocusing) occurred which allows un-deviated transmission of a beam that exhibits spatial phase perturbations associated with scattering.

Spherical particles do not need to be identical to create identical phase shifts on scattering which will lead to constructive interference in the forward direction. At 0°, although the amplitude of scattering strongly depends on the sphere radius, the phase shift associated with scattering does not. When variations in the scattered phase are small with changes in sphere radius, even an arbitrary particle size distribution can result in coherent scattering effects at 0°. Fry et al. (1992) showed that scattered phase variations are small and coherent scattering is possible at sphere radii greater than a few micrometers (Figure 2).

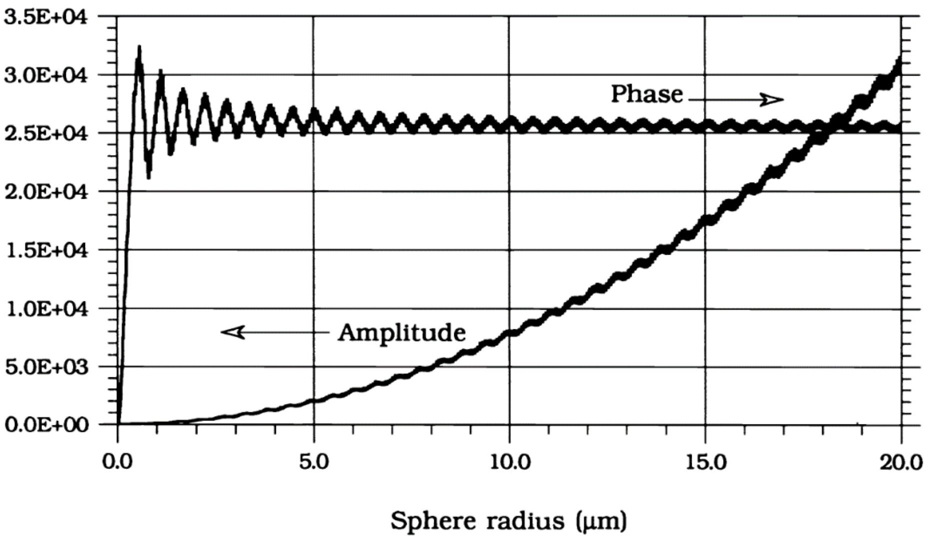

Figure 2: Variation in phase and squared amplitude of the scattering matrix element at 0 degrees for spherical particles with a refractive index of 1.46, from (Fry et al., 1992), Figure 2.

2.1.2.2. Mie theory of scattering

The description of the Mie theory of scattering given in this section follows the descriptions given in the Ocean Optics Web Book, unless otherwise referenced (Mobley, 2020).

The angular distribution of scattering from the particle sizes typically found in marine waters is described by Mie theory, which deals with scattering from particles with sizes on the order of the wavelength of the incident light and is considered a useful tool for understanding optical properties in marine waters to the first order (Slade et al., 2013). Mie theory is the description of the solutions to the Maxwell’s equations for a plane wave interacting with a homogenous sphere (particle) stuck within a medium with a different index of refraction from the sphere. These solutions provide information about the electric field inside and outside of the particle, giving information about the scattered distribution of light and also about changes to the polarization. Although Mie theory can be applied to all sizes of particles, it is most commonly used in the particle size regime defined by a particle size parameter between 1 and 50 (or a particle size on the order of 0.1 to 10 times the incident wavelength) (Kidder & Vonder Haar, 1995). At smaller size scales, scattering behaviour can be well-described by Rayleigh scattering, and at larger sizes it can be described by geometric optics via diffraction.

To implement Mie theory accurately to describe angular scattering distributions, several assumptions must be met. First, the scattered light is assumed to have the same wavelength as the incident light (i.e., scattering is assumed to be elastic). A second assumption is that all particles are assumed to act as independent according to the definition of Van de Hulst

(1957). This assumption of independence ignores the effect of multiple scattering events and also assumes that the density is such that all particles are separated by at least three particle diameters from their nearest neighbour (Jerlov, 1968). Mie theory is also based on the theory of propagation of a plane electromagnetic wave, as in Maxwell's equations, meaning that the light source must also be assumed to be a plane wave. This condition is easy to satisfy when considering a coherent light source such as a laser or a point source used far away from its origin.

Assumptions about the particles and medium that are necessary for Mie theory include that all particles must be modelled as homogenous spheres with a refractive index different from the surrounding medium, where the medium must be assumed to be homogenous, non-absorbing, and infinite. Mie theory calculations take in the particle size parameter, which includes information about the radius of the sphere and the wavelength of the incident light, the refractive index of the particle and that of the surrounding medium, and the angular range of interest. Outputs of Mie theory implementations include the elements of the amplitude scattering matrix $S_i(\vec{\theta})$, efficiencies Q_i describing the rate of extinction, total scattering, and backscattering, for example, and the average cosine of the scattering angle, g.

The equations involved in the implementation of Mie scattering calculations will be described in more detail in Section 5.4.1., where the exact details of the Mie theory implementation used in this thesis will be discussed.

Although Mie theory is commonly and successfully used in many scenarios to describe scattering in marine waters, it has some associated limitations. Mie theory technically only considers scattering from spherical particles but it has been found to provide a good approximation for all particles that are considered to be "roughly spherical" too. It is possible that the predictions of Mie theory can greatly vary from observations for irregularly shaped particles, but these differences are most significant in the backscattering directions, which are not under consideration in this thesis (Curtis et al., 2008). Slade et al. (2013) state that approximations to the scattering phase function by Mie theory can be affected in both small, moderate, and large backscattering angles when particles with irregular (non-spherical) shapes are used, which limits the accuracy of Mie theory as an approximation to the scattering phase function. Even for spherical particles, roughness on the surface of these particles can cause substantial changes in the predicted scattering especially in backwards directions. These limitations to Mie theory approximations of the scattering angle are considered to be smallest at forward scattering angles and increase with the angle of scattering. Therefore, although these limitations should still be considered, they are considered to be less substantial for this study involving the effect of forward scattering compared to instruments that measure backscattering.

Another limitation to Mie theory is that it is difficult to make accurate estimations of both the beam attenuation coefficient and the backscattering coefficient simultaneously, which may be limiting in some applications (Organelli et al., 2018). This study also found that at least 75% of marine particles contained a structure or morphology too complex to be accurately represented by a homogenous sphere model, although they also state that this effect is most significant in the backscattering direction and that the forward scattering direction is better represented by the average characteristics of a homogenous sphere. Nonetheless, the effects of aggregation of particles in realistic marine environments should be considered when implementing Mie theory to approximate scattering models.

As discussed, implementations of Mie theory to non-spherical particles must be treated carefully and may be inaccurate when scattering at large angles is considered. Furthermore, the computational complexity of Mie theory implementations scales with the size parameter of the simulation. However, the work discussed within this thesis will focus on forward scattering effects from particles considered to be well-approximated by homogenous spheres, and so Mie theory is an appropriate method in this use case for approximating scattering in our system to the first order.

2.1.3. Beam attenuation

The beam attenuation coefficient (m^{-1}) can be calculated via the Beer-Lambert law as described in Eq. (1). Spectrophotometers have been used to indirectly measure the beam attenuation coefficient of suspended particles in laboratory set-ups, since they measure absorbance which can then be corrected to attenuation (Bateman et al., 1959). However, the most commonly accepted method for measuring the beam attenuation coefficient is using a direct-path transmissometer.

2.1.3.1. Transmissometry

The following discussion on transmissometers will follow that defined by the IOCCG Protocol on “Beam Transmission and Attenuation Coefficients: Instruments, Characterization, Field Measurements and Data Analysis Protocols” (Boss et al., 2019).

As described in Chapter 1: Introduction to the scattering problem, the most commonly adopted type of transmissometer is the direct-path transmissometer (Figure 1), which is comprised of the following: a point source and focusing lens to create a collimated beam; an optional interference filter to select a particular waveband of light (assuming a white light source); a liquid attenuating medium contained between two transparent windows; a focusing lens and a pinhole to block off scattered light; and a detector.

Although the most common choice of source light is a white light or light-emitting diode (LED), other instruments, such as the range of LISST devices, use a laser as the light source which can be expanded to the appropriate beam size for interaction with the sample (Agrawal & Mikkelsen, 2009; Slade & Boss, 2006). The choice of laser light as a source can potentially introduce polarization-based effects to the attenuated light field, primarily due to polarization changes that occur on scattering, which must be considered (Bickel & Bailey, 1985; Cochenour et al., 2010; Koestner et al., 2018). The significance of these effects vary between instruments, dependent on factors such as the angular range of scattered light being measured, the initial polarization of the incident laser light, and the polarizing/depolarizing properties of the sample contents (Koestner et al., 2020).

Although the transmissometer set-up depicted in Figure 1 is conceptually simple, maintaining the alignment of such a device, particularly in field conditions, is difficult and even small changes in alignment can result in large changes to the beam attenuation coefficient. Although this thesis will describe a lab-based transmissometry set-up, sensitivity to changes in alignment was still a critical concern and efforts to minimize changes to alignment throughout measurement campaigns will be discussed in Chapter 4: Optimization of a spatial-coherence based transmissometer.

Devices with longer path lengths have been created by using several reflective optics to create a folded-path geometry, which is particularly beneficial in areas with clear waters to make more sensitive measurements at low beam attenuations (Jerlov, 1957). An idealized transmissometer would be that with a variable path length that could be adjusted to perform optimally for its environment. The ability of such an instrument to make measurements at multiple path lengths would also allow it to be self-calibrating, assuming the optical alignment of the device can be maintained constant (Barth et al., 1997). However, this requirement for a constant optical alignment under changing path lengths is exactly what makes this type of device so difficult to produce and maintain. Factors that can introduce a change in alignment include: changes to alignment of the optics or detector due to a shift in beam focal position; and divergence of the beam leading to different optical areas being covered for different path lengths.

To accurately measure the beam attenuation coefficient, without introducing errors associated with losses from beam interactions with the optical set-up and the response of the detectors, measurements of the beam attenuation coefficient of a known medium must be determined for calibration. In most cases, this is taken to be the attenuation measured through pure water; however, in cases where the particulate beam attenuation in marine waters is desired without the influence of the medium, filtered seawater may instead be used (W. H. Slade et al., 2010).

2.1.3.2. The problem: measurement of forward scattered light in commercial transmissometers

Although the idealized design of the direct-path transmissometer involves only the measurement of directly transmitted light, in reality the detector area of a transmissometer is illuminated by a solid cone of light scattered at angles within $0 \leq \theta \leq \theta_c$, where θ_c is the collection angle of the combined lens, pinhole, and detector arrangement as shown in Figure 3 and described in Equation (2).

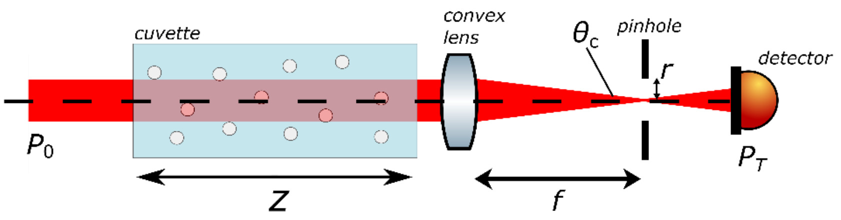

Figure 3: Standard transmissometer forward scattering problem. Light enters the transmissometer with a power P_0, where it passes through a sample volume with a path length of z. The light that exits the sample volume is focused down using a lens with focal length, f, through a pinhole with finite radius, r, onto the detector where the "transmitted" power is measured as P_T. The finite size of the pinhole allows light scattered at angles less than θ_c to also be detected.

Since the pinhole of the transmissometer cannot be made infinitely small, some amount of scattered light contained within the angle subtended by θ_c will always be detected in a direct-path transmissometer. There is a trade-off between decreasing the size of the pinhole to reduce the collection of scattered light and the increase in alignment sensitivity as the pinhole size gets smaller. As discussed previously, the measurement of the beam attenuation coefficient in a direct-path transmissometer is especially sensitive to changes in device alignment. In commercial devices, a collection angle on the order of 1° has conventionally been chosen. For example, the WetLabs C-Star devices have a collection angle of 1.2°, the WetLabs ac-9/s series of devices have a collection angle of 0.93°, and the collection angle of the SeaTech transmissometer was 1.03° (Baker & Lavelle, 1984; Boss et al., 2009).

The collection of scattered light by the detector results in the beam attenuation coefficient being systematically underestimated in these devices. The degree of error that this results in is dependent on the transmissometer design, since transmissometers with larger collection angles will result in larger estimated errors associated with the collection of scattered light. For example, Boss et al. (2009) observed that the attenuation measured by eight different transmissometers with different path lengths and collection angles varied substantially, generally following the rule that those with larger collection angles measured lower attenuations. For example, in one area a C-Star instrument with 1.2° collection angle measured 55−90% of the beam attenuation coefficient of a LISST-B instrument with 0.029° collection angle, and an ac-9 instrument with 0.93° collection angle measured between 60−104% of the coefficient measured by the same LISST-B. Voss and Austin (1993) estimated an average attenuation error of 19% for a transmissometer with a 1° collection angle at 670 nm. On the other hand, Boss et al. (2009) and McKee et al. (2013) both measure and predict errors between 50–80% in ac-9 beam attenuation measurements as a result of scattering bias. Although there is a lack of clarity on the exact value of attenuation errors introduced by the collection of scattered light, there is consensus that this is a substantial effect.

To accurately correct the beam attenuation coefficient for these scattering errors, the volume scattering function, describing the angular distribution of scattered light, must be known for the sample. Although it is possible to measure the volume scattering function from 0.1° to 150° using the LISST-VSF, the behaviour of the volume scattering function in the near-forward direction is difficult to measure due its steep rate of change, which creates uncertainty in the accuracy of any corrections using this approach. An alternate approach involves the development of iterative scattering correction schemes, such as that developed by McKee et al. (2013) for ac-9/s transmissometer measurements that utilizes Monte Carlo simulations. This approach requires the additional concurrent measurement of backscattering coefficients and independent, validated absorption measurements for comparison, but has shown agreement with corrected attenuation estimates made using the LISST-100X, which was chosen as the best commercially available attenuation comparison due to its small scattering collection angle of approximately 0.027°.

However, the current most-common and recommended approach for dealing with scattering errors in the measurement of beam attenuation coefficients is to make no attempt to correct for these errors but instead to report the uncorrected results alongside the parameters of the transmissometer (i.e., path length, collection angle, etc.). The IOCCG protocol regarding beam transmission and attenuation measurements highlights the need for new approaches that can provide unambiguous measurements of the beam attenuation coefficient that are free from scattering errors (Boss et al. 2019).

2.2. Spatial Coherence

An important property of light fields that has not often been considered is their wave-like nature and the associated temporal and spatial coherence of the field. This property is capable of producing large changes in the intensity of the light field in specific directions, which can affect readings of IOPs. Examples of this phenomenon will be explored later in this thesis.

In this section, the broad concept of coherence, particularly that of spatial coherence, and how it can be utilized will be detailed in brief.

2.2.1. Theory of coherence

The qualitative description of coherence herein follows the description provided in Modern Classical Optics by Brooker (Brooker, 2003).

Imagine a typical representation of a plane light wave propagating in time, t, and one spatial dimension, x. The wave periodically oscillates between maxima and minima known as peaks and troughs with a given amplitude A and wave period T. The distance between adjacent peaks or troughs is given by the wavelength λ. A wave of this form with constant period and amplitude can be described by the wave equation, as follows:

$$\Psi(x,t) = A\cos(kx - \omega t + \varphi), \tag{9}$$

where k is the wave number given by $2\pi/\lambda$, ω is the angular frequency given by $2\pi/T$, and φ is the phase difference or relative phase of the wave.

The absolute phase of a wave itself is a description of the position of the peaks and troughs of the wave. However, this is a difficult concept to imagine and quantitatively measure in isolation for a single wave. Generally, when the phase of a wave is discussed, we are referring to the relative phase of a wave, measured as the difference in the wave’s peak positions relative to those of some reference standard or another wave. This relative phase is easier to measure and describes how well the peaks and troughs of the waves line up with each other. For example, if the maximum values of the first wave line up with the minimum values of the second wave, these waves have a phase difference of π, commonly referred to as out-of-phase. To be able to detect a measurable, constant phase difference between multiple waves, these waves must have constant, matched wave periods. This is known as waves being coherent with respect to each other.

The above description of a wave with a single frequency is an oversimplification. In reality, most waves are sums of multiple different frequencies which introduces some degree of randomness to the wave behaviour. The coherence of a wave is correlated with this randomness. Furthermore, a single light source cannot be described as coherent with itself. However, it can be considered to be made up of multiple wavetrains which can exhibit coherence with each other, where an entire wavetrain is a sum of waves of different frequencies that make up the light signal. Wavetrains are coherent with each other if there is a statistical correlation between their random variations with time. On the other hand, they are incoherent with respect to each other if these variations are uncorrelated. Another way of looking at this is that the wavetrains are coherent with each other if they have a fixed phase difference that is independent of time.

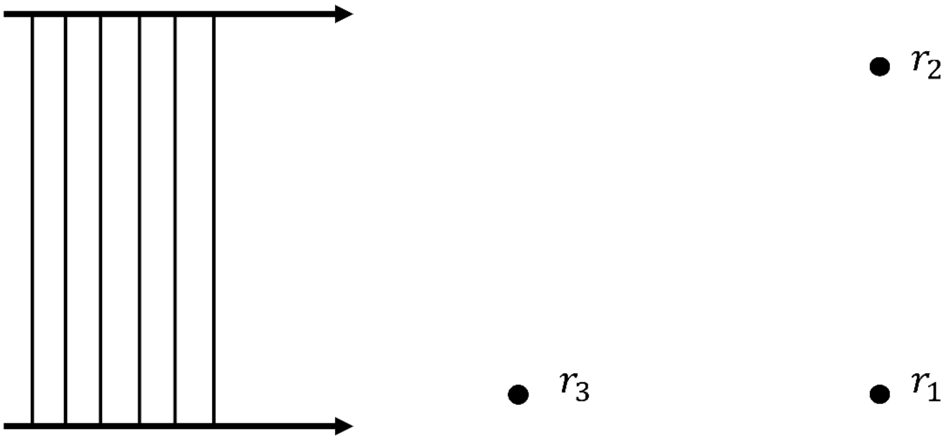

*Figure 4: Diagram depicting three points in space (r_1, r_2, and r_3) between which the correlations between the plane wavefronts described by U(**r**, t) can be considered. Recreated after Brooker Fig. 9.3. (Brooker, 2003)*

Although all coherence between wavetrains at different points is a measure of statistical correlation, this definition contains two different types of coherence that are analogous but independent of each other: temporal (or longitudinal) coherence; and spatial (or transverse) coherence. The difference between these types of coherence can be visualised simply by looking at Figure 4. Consider wavetrains that are depicted as plane wave fronts propagating from the left of the page to the right and can be described at any given point and time as *U*(**r**, t). Whereas transverse coherence is defined as whether or not *U*(r_1, t) is correlated with *U*(r_2, t), longitudinal or temporal coherence is defined as whether or not *U*(r_1, t) is correlated with *U*(r_3, t).

2.2.2. Techniques utilizing spatial coherence

There are multiple techniques that rely on the incident light field exhibiting either spatial or temporal coherence in order to produce the desired result. Experiments using spatial interference can be considered as “division of wavefront” and include examples such as the Young’s double slits and Rayleigh refractometers. For spatial interference to occur, a small angular spread of the incident beam is required, alongside transverse or spatial coherence and a sufficient coherence area. Experiments utilizing temporal interference are known as “division of amplitude” techniques and include examples such as the Michelson interferometer and Fabry-Perot cavities. For these experiments, the collimation of the beam is unimportant but a small bandwidth is required. Longitudinal or temporal coherence is necessary for which a sufficient coherence time or length is required. In this thesis, we will focus on techniques that require spatially coherent light sources. Typically, optical elements or techniques that require a coherent incident field rely on the phenomenon of interference to produce the required effect.

2.2.2.1. Interference and Young’s Double Slit experiment

The following description of the interference of electromagnetic waves is based on the discussion in From Fourier to Fresnel (Adams & Hughes, 2018).

Two waves can be superimposed and their amplitudes added together depending on the phase difference between the waves, following the principle of linear superposition. Waves that have a well-defined relative phase difference between each other are able to interfere either constructively or destructively, depending on if they are in phase or out of phase, respectively. *I.e.*, when the peaks of two waves are superimposed, constructive interference occurs; however, if the peak and the trough of two waves are superimposed, destructive interference occurs and the intensity of the light is nullified.

When two waves, each with an intensity of I_0, interfere constructively, the intensity at the interference maxima becomes 4 times that for a single wave ($4I_0$), as intensity varies as the square of the amplitude of the electric field. However, since the intensity at the minima where destructive interference occurs is 0, the average intensity over the system is $2I_0$. Interference causes the effective redistribution of the incident electromagnetic field; however, the total amount of energy (typically measured as intensity in a given system) must remain fixed.

Interference of light waves was first established by Young, who demonstrated that light originating from two point-sources (apertures) would form sequential patterns of constructive and destructive interference (Young, 1804), when the aperture size is much smaller than both the spacing between apertures and the distance from the apertures to the image plane. It can be shown that the only parameters that contribute to this pattern of constructive and destructive interference is the relative phase between the light emanating from the point sources and the aperture spacing.

Taking this concept further, the interference between point sources originating from two apertures can be extended to *N* apertures, where *N* is large. The Young's double slit experiment scaled up to *N* apertures is the underlying principle of a diffraction grating.

Brooker further discusses the requirement for coherence in the Young's double slit experiment in Chapter 9 of Modern Classical Optics (Brooker, 2003). Young's double slit experiment is a particularly important case for measuring spatial coherence; through this experiment, the concept of a coherence area can also be introduced.

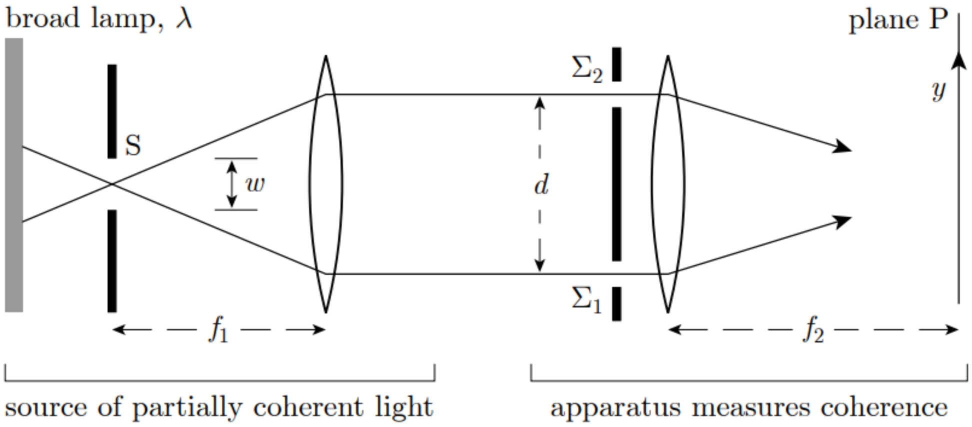

Figure 5: A diagram used to illustrate the dependence of the Young's double slit experiment on the range of angles ω and coherence of the incident light source from point S. The aperture spacing is given by d and the two slits are referred to as Σ_1 and Σ_2. The author states that the lenses are added to make the derivations simpler but that the conclusions regarding the effect of light collimation and partial coherence are general. Taken from Fig. 9.1 from Chapter 9 of Modern Classical Optics (Brooker, 2003).

Using the diagram in Figure 5, Brooker explains that the intensity pattern at plane P is given by:

$$intensity \propto \cos^2\left(\frac{\frac{1}{2}kdy}{f_2}\right), \tag{10}$$

when the light originates from the centre of source S. Light that arrives at plane P from different locations on the source S will introduce a phase shift (of a maximum of $\frac{1}{2}\omega(f_2/f_1)$)

to the argument inside the cosine in Eq. *(10)*. This can be considered equivalent to a range of different angles of the incident light, indicating that the beam is not perfectly collimated.

The collimation of the beam incident on the Young's slit experiment is important for the following reasons. If the range of arrival directions of light at the experiment is greater than the angular width of a singular fringe, then discrete Young's fringes cannot be formed and are instead blurred out. This is equivalent to if the phases within the cosine squared intensity pattern in Eq. *(10)* cover a range greater than 2π. In the case of blurred fringes, interference is still happening but the wavetrains passing through each slit are all incoherent with respect to each other, resulting in interference nulls. For no fringes to occur, all wavetrains must have completely random phases with respect to each other. This means that all phase differences between the individual wavetrains must be spread out in a random pattern over a range of 0 to 2π. The presence and contrast of fringes in a Young's slit experiment is itself a way to measure the coherence of different wavetrains with respect to each other. Incoherence can essentially be viewed as the smearing out of the fringes in a Young's slit experiment, or the randomization of the phase difference between wavetrains coming from a light source.

The coherence area can be calculated in the following manner for a Young's slit experiment with a slit spacing d. The range of angles that light travels within a beam collimated by a lens with focal length f_1 from a point source with angular width ω can be defined as $\theta_s = \omega/f_1$. Then, $d_0 = \lambda/\theta_s$ (which is equivalent to the slit separation at which fringes disappear). The coherence of the light with respect to the fringe set-up can then be defined as:

1. Fully coherent when $d << d_0$;
2. Partially coherent when $d < d_0$;
3. Incoherent when $d >= d_0$.

For the fringes to be observed from Young's slits, then the wavetrains from one slit to another must be within each other's coherence areas which is given by $(2d_0)^2$ for a square source area. The parameter d_0 always defines some dimension of the coherence area with the exact form dependent on the form of the source beam.

In simpler terms, the coherence of the beam across the grating area is proportional to the wavelength divided by the spread of angles reaching the grating relative to the grating spacing. For example, for a uniform circular source, radius of the coherence area is given by:

$$d_0 = 1.22\,\lambda/\theta_s. \qquad (11)$$

In practice, the coherence area of a source may be measured by adjusting the fringe spacing until the fringes just begin to blur out. This can be used to estimate the spread of angles reaching the grating.

2.2.2.2. Orbital angular momentum

The production of complex spatial structures is another technique requiring the input of a spatially coherent incident field; an example of this type of structure is a light field carrying an orbital angular momentum (OAM). All light beams with an azimuthal phase dependence carry an OAM, which can either be understood in terms of a rotating Poynting vector caused by the beam's helical phase fronts or derived from Maxwell's equations (Yao & Padgett, 2011). The helical phase fronts of an OAM-carrying beam have a number of twists given by the mode number l. OAM is quantized in integer units of $l\hbar$ per photon, where $\hbar$ is the reduced Planck's constant (Allen et al., 1992). In comparison, Gaussian beams have flat phase fronts with no azimuthal phase dependence. All OAM beams are characterized by a singularity at their centre where the phase is not well-defined, leading to zero intensity to satisfy the wavefunction (Figure 6). The width of the intensity null associated with the phase singularity at the centre of the OAM mode increases with increasing OAM mode number l. OAM beams are inherently orthogonal with a theoretically infinite number of eigenstates and can be characterized by a set of Laguerre-Gaussian modes (Allen et al., 1992; Chen et al., 2020).

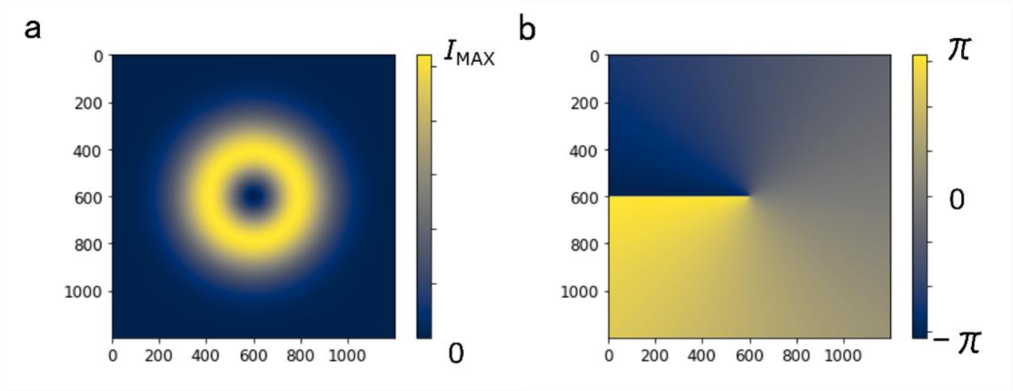

Figure 6: a. Intensity, and b. phase profiles for an OAM beam with mode number = 1.

OAM modes can be produced using a variety of methods, with varying advantages depending on the desired application. A couple of examples of types of convertors include refractive optics, such as spiral phase plates (SPPs), and forked gratings (Bazhenov et al.,

1992) loaded on diffractive optics such as spatial light modulators (SLMs) (Yao & Padgett, 2011). Spiral phase plates have high conversion efficiencies (Chen et al., 2020) compared to other methods but can only produce a single OAM mode due to their fixed physical characteristics. On the other hand, SLMs can produce OAM beams with varying mode numbers via programmed liquid crystal displays that change parameters like the beam phase (Maurer et al., 2007). Both refractive and diffractive optics like these rely on a spatially coherent incident field. Diffractive optics rely on the phenomenon of interference to provide new wave patterns, as described in the previous subsection. Refractive optics alter light patterns by refraction of the incident field from many small structures — creating the intended new structure typically relies on the assumption of a Gaussian input field, rather than the rapidly changing phase associated with noise or speckle.

An example of the spatial coherence requirement for light structures like OAM is their sensitivity to degradation upon scattering. This sensitivity to scattering events has been widely explored in the field of communications, where the use of OAM to carry information has been proposed. Scattering from atmospheric turbulence has been both modelled (Tyler & Boyd, 2009) and observed (Ren et al., 2013) to limit free-space OAM communications by altering the helical phase fronts of OAM beams and introducing crosstalk (i.e., energy leakage between adjacent OAM modes) that becomes increasingly severe with increasing turbulence strength.

2.3. Transmissometers and spatial coherence

Changes in spatial coherence associated with scattering have been exploited to improve attenuation and transmission measurements, primarily using OAM beams (Alley et al., 2018; Li et al., 2023; Watnik et al., 2023). OAM-based transmissometers rely on the theory that, although all incident light will experience a change in phase when passing through a phase plate, the randomized phase distribution of scattered light prevents the formation of a stable optical vortex. However, spatially coherent light will create a stable vortex when passed through a phase plate. The concept assumes that spatially coherent, transmitted light forms a ring about a vortex null, where spatially incoherent, scattered light remains. These signals can then be separated, either using image processing techniques or by introducing additional optics prior to signal detection. For example, Li et al. (2023) created enhanced spatial separation between the coherent and incoherent light by imparting a large OAM mode and focusing the beam down such that the incoherent light formed a spot in the centre of the coherent ring. Watnik et al. (2023) simulated a scheme that could minimize the effect of scattered light on the transmitted signal by placing a beam block after the phase plate, designed to block out the spatially incoherent portion while allowing the spatially coherent light to pass through and be focused via lens onto a detector.

These techniques make the assumption that scattering events are linked with a loss in spatial coherence, with any remaining spatial coherence after scattering being negligible. This assumption, which will be tested in this thesis, is required for the separation of coherent and incoherent light to be accurately used as a proxy for the separation of transmitted and scattered light.

A particular example of this approach attempting to solve the scattering bias in transmissometry is presented by Alley et al. (2018) have demonstrated an optical vortex transmissometer to try and distinguish between scattered and unscattered light for large scale turbulence in the multiple scattering regime, utilizing the concept that only coherent, unscattered light can be given a stable OAM (Cochenour et al., 2017). They performed transmissometry by passing a Gaussian beam through a sample before encoding an OAM mode using an SPP. When the beam passed through a clean water sample, a negligible amount of light was scattered, causing it to become spatially incoherent, such that the spatially coherent light with an unperturbed phase front produced an OAM mode. However, light that was incoherently scattered from the highly scattering sample did not become encoded with an OAM mode and instead raised the background signal compared to that of clean water. This raised background level was used to determine the amount of forward scattering and was effectively removed from the directly transmitted signal, leading to higher $c(\lambda)$ measurements compared to a standard transmissometer.

The set-up used by Alley et al. (2018) is shown in Figure 7. They used a 532-nm diode-pumped laser, attenuated using a beamsplitter and picked off pre-sample for power monitoring. The scattering samples were produced using solutions of Equate-brand antacid and clean water, with attenuation coefficients ranging from $c = 0$ m^{-1} to $c = 33$ m^{-1} determined using a WetLabs C-Star transmissometer, where c > 5 m^{-1} describes high turbidity. The sample path length was $z = 30.5$ cm. An OAM mode with $\ell = 16$ was encoded after scattering using an SPP. A diverging lens expanded the result onto a ThorLabs CCD camera, with ND filters available to keep the signal within the camera's dynamic range. They measured a difference in attenuation between their proposed OAM-based transmissometer and a commercial C-Star on the order of 10% for attenuations between approximately 10 m^{-1} and 35 m^{-1}.

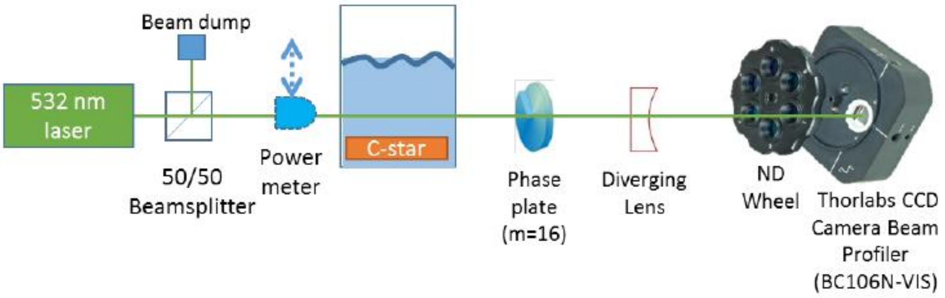

Figure 7: Set-up of the OAM transmissometer of Alley et al. (2018), where a 532-nm beam is scattered before an SPP encodes an OAM mode. The coherent, unscattered beam produces an OAM mode, whereas the incoherent, scattered light contributes to a diffuse background signal. Both components remain on-axis and are imaged using a ThorLabs CCD camera. A WetLabs C-star transmissometer is used for comparison. Taken from (Alley et al., 2018).

As discussed previously, OAM modes can be encoded on incident coherent light fields by both refractive and diffractive methods. The SPP used by Alley et al. (2018) to produce a working transmissometer offers a relatively low-cost solution. Alternate methods that could be used in a similar OAM-based transmissometer include a forked diffraction grating to encode an OAM structure on an incident light field. This forked diffraction grating can be loaded onto an SLM to allow the user to easily change and explore the optimal diffraction parameters for separation of the transmitted and scattered light.

2.3.1. Trial of an OAM-based transmissometer

Using a forked diffraction grating loaded on an SLM, we encoded OAM modes on an incident field that had passed through scattering media containing liquid antacid. Our set-up is shown in Figure 8, designed to mimic that in Figure 7, excepting the use of an SLM rather than an SPP to produce the OAM mode. The SLM produces an OAM mode in the first-order diffracted mode, separated from the Gaussian component remaining in the zeroth order. We used a 521.2-nm single-mode fibre-pigtailed laser, propagated through a polarizing beamsplitter (PBS) and half waveplate (HWP) prior to the scattering sample for optimizing the polarization incident on the SLM. The scattering samples were produced using Milk of Magnesia and clean water solutions. The OAM modes were encoded using an SLM that produces the desired OAM mode in the first diffracted mode. Two cameras were used for imaging for inter-comparison (FLIR Chameleon CCD and ThorLabs CMOS).

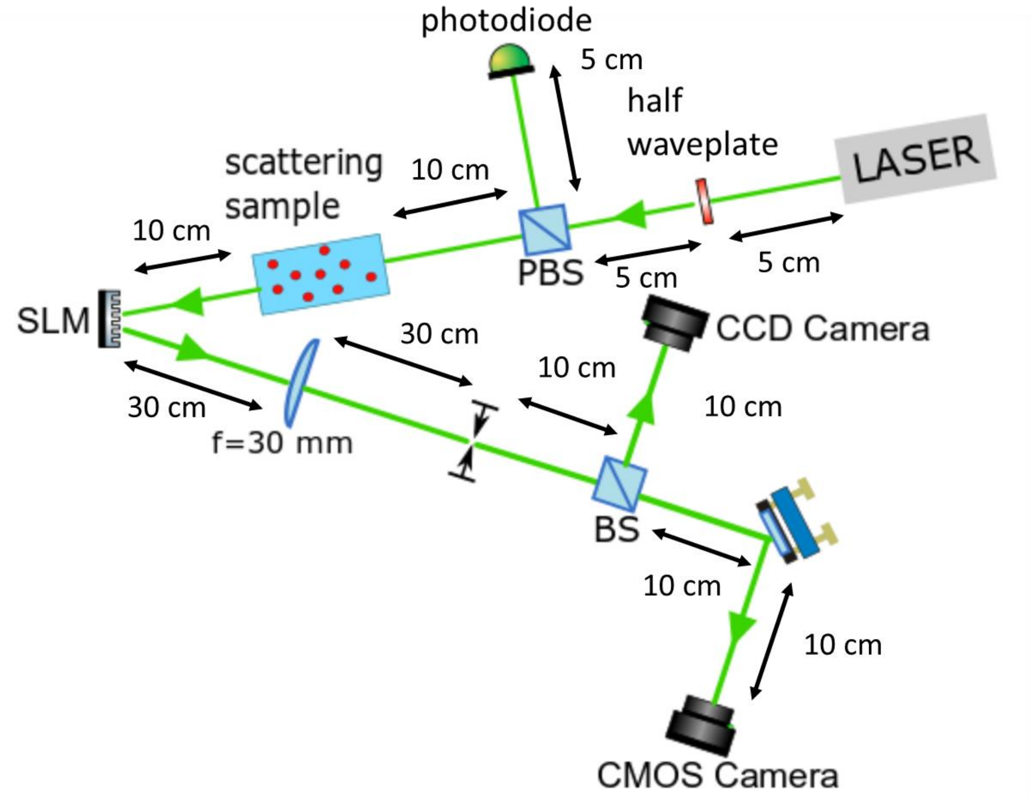

Figure 8: Experimental set-up roughly reproducing the OAM transmissometry set-up of Alley et al. (2018). The primary difference is the use of an SLM to encode an OAM, as opposed to an SPP. Diagram not to scale but dimensions given. Note: the lens was chosen to be greater than several focal lengths away from the SLM to minimise collection of stray light scattered from the SLM.

Scattering samples at three optical densities were used and OAM modes were produced after scattering for $\ell = 0$ to $\ell = 16$. Reference measurements through both clean water and free space were taken. For each data point, an image stack of 20 frames was taken. In data processing, these stacks were averaged, the measured dark level of the camera was removed, and 1D profiles through the centre of the OAM mode were taken for analysis. The OAM mode and zeroth order modes for each case were imaged separately and then stitched together in processing to allow for comparison of both modes. The results of this process for three attenuations can be seen in Figure 9 a–c on a log intensity scale. The OAM mode encoded on spatially coherent (assumed purely transmitted) light and the incoherent light over the 0th diffractive order is indicated in Figure 9b.

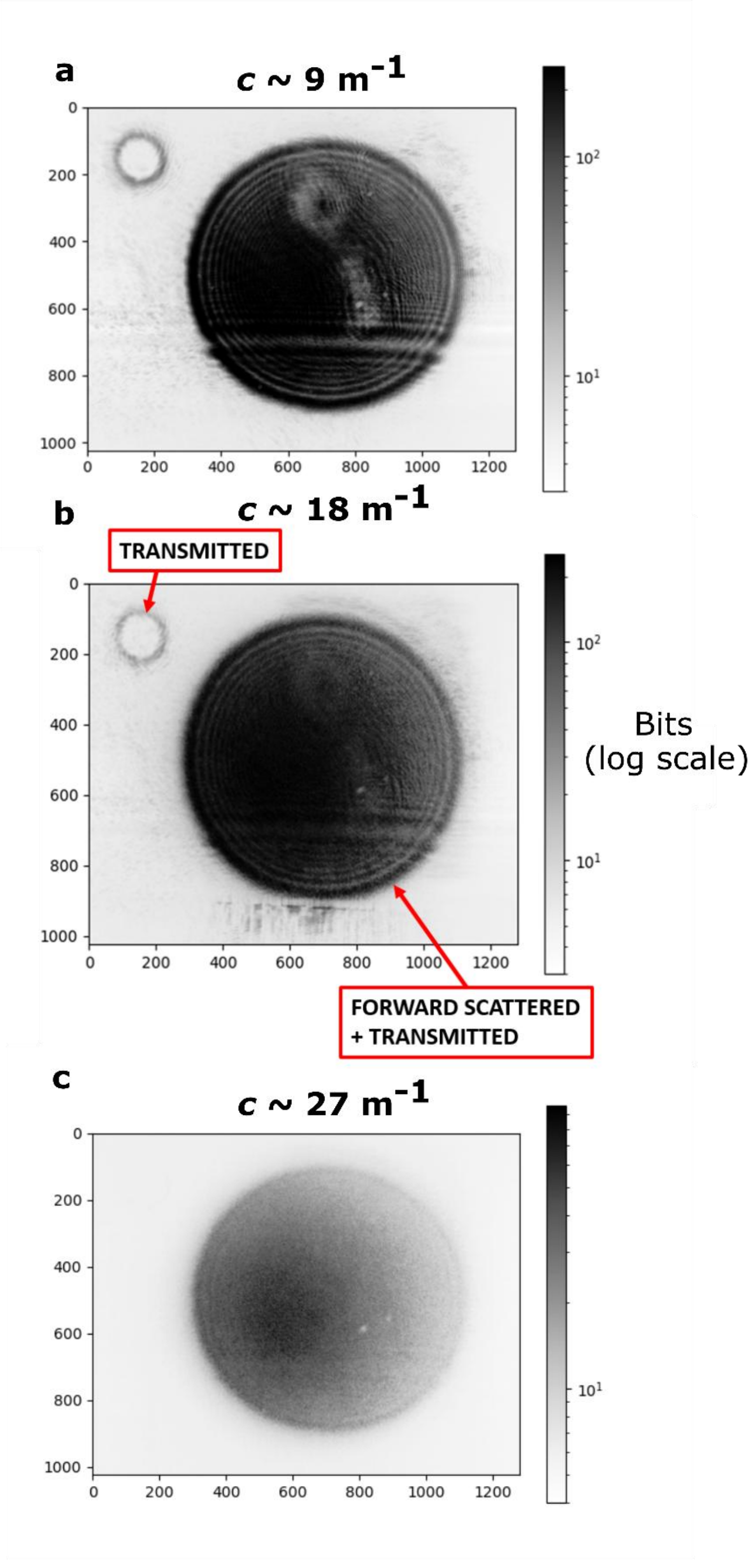

Figure 9: Stitched images of OAM mode and 0th order mode produced by diffraction from SLM after passing through an attenuating sample with approximate attenuation values of a. $c = 9\ m^{-1}$, b. $c = 18\ m^{-1}$, and c. $c = 27\ m^{-1}$. All images were plotted on a log intensity scale to image both OAM mode and 0th order simultaneously. Based on the theory presented by Alley et al. (2018), only transmitted light should be used to produce the OAM mode due to the spatial coherence requirement.

Across all three scenarios, as the attenuation of the sample increases, the light diffracted into the OAM mode decreases until it cannot be imaged at c = 27 m^{-1}. This highlights that, as the degree of scattering increases, less coherent light is available to form the OAM mode. This was hypothesized to be due to an increase in spatial incoherence with the increasing degree of scattering in a more optically thick sample. It can be seen in Figure 9c that some amount of light is still able to reach the 0th order diffraction mode. Looking at the 0th order at c = 27 m^{-1} on a linear intensity scale (as in Figure 10), a speckle-like pattern that is typically associated with some non-negligible degree of spatial incoherence can be seen. This suggests that while spatially incoherent light is able to reflect and propagate to remain in the 0th diffraction order, it has a lower ability to reach higher order diffraction modes.

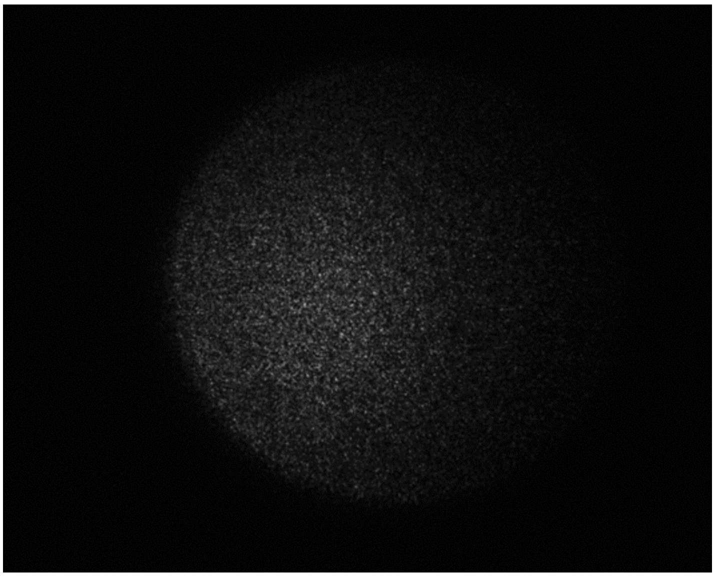

Figure 10: Experimental image capture of 0th order diffraction mode from SLM after light has passed through a sample with c = 27 m^{-1}. The above image shows a single frame rather than an average d picture and the intensity is plotted on a linear scale. A speckle-like pattern is present over the 0th diffraction order, suggesting the presence of spatially incoherent light.

This separation of primarily coherent light into the higher order diffraction modes while the majority of spatially incoherent light remains in the 0th order mode can be tuned via the parameters of the diffracting optic. The period of the forked diffraction grating can be altered such that the OAM mode position moves further away from the speckle-like cloud associated with scattering, which remains in the same position over the 0th diffractive order. This is unlike the case for producing an OAM mode using an SPP, where the mode must always be produced concentric with the incident field.

Therefore, using a diffractive optic such as a grating rather than a refractive optic such as a phase plate allows for greater separation of a portion of the coherent, transmitted light from the scattered speckle. This will allow for the design of systems with minimal effect of scattering on coherent light measurements without having to utilize image processing techniques after real-time measurements. Furthermore, this concept is not dependent on the use of a forked grating that produces an OAM mode; the separation fundamentally relies on the inability of spatially incoherent light (which is comprised of multiple random phase terms and differing beam angles) to interfere to create higher-order structures via refractive or diffractive optics. This application should hold for any form of diffraction grating. This thesis proposes that this separation can be performed using a commercial, off-the-shelf high-efficiency holographic linear diffraction grating, allowing more substantial spatial separation between the coherent and incoherent light portions than provided using an optical vortex method. This removes the need for image processing to extract the transmitted signal, allowing for real-time processing of results, and produces substantial spatial separation. This allows for a simpler transmissometer set-up than an OAM-based system, which can be technically challenging and requires specialized optics. This thesis will explore and characterize the performance of this diffraction grating-based transmissometer across a wider range of particle types and sizes than has yet been explored for OAM-based transmissometers.

Chapter 3: Initial transmissometer performance using a diffraction grating

The separation of spatially coherent and incoherent light is a technique that is not unique to OAM-based optics. In fact, this approach can be generalized to any optic or technique that has a requirement for spatial coherence in order to operate as intended.

In this chapter, the use of a diffraction grating as a filter for spatial coherence and its application in a novel transmissometer will be discussed.

3.1. Specific theory: Diffraction and coherent light

The lines on a linear diffraction grating can be considered as equivalent to a scaled-up version of the slits in Young's double slit experiment (Adams & Hughes, 2018), such that each line in the grating then acts as a point source for light that can interfere constructively or destructively at the higher diffracted orders.

For light incident on the grating that is 100% spatially incoherent, a linear diffraction grating then produces N sources of light (where N is the number of lines on the grating) that are all out of phase with each other, creating completely destructive interference at diffraction modes with a non-zero order.

This scenario becomes more complicated in the case of light that is partially spatially coherent. In this case, two points that are closer on the wavefront are more likely to be spatially coherent with each other than two points that are further away. This means that the period, related to the line spacing, of the grating affects the degree of spatial coherence perceived by the grating. For example, when the period of the grating is lower, these point sources are spaced further on the wavefront and more likely to be out of phase with each other, leading to an increased likelihood of destructive interference at the diffracted order, compared to a grating with a higher period (more lines/mm). This could potentially make the choice of grating period important in the case of light that is not 100% spatially incoherent on scattering.

However, the initial assumption in this project was that that light from scattering from particles is 100% spatially incoherent, such that it should not be possible to sample the beam in such a way that a varying amount of coherence can be observed and the grating period is not important. This assumption would suggest that the phase difference added to each scattered photon is effectively random and not related to particle characteristics like the size or geometry. This assumption is yet to be tested and will be commented on later in the thesis, but this initial assumption was made based on the OAM transmissometer design of Alley et al. (2018). As such, the first prototype of the coherence transmissometer chose a grating with 1800 lines/mm.

In addition to the coherence requirement for interference from a diffraction grating, the position of the principal maxima formed also rely on the wavelength of the incident light, the aperture spacing, and the angle of incident light. For a reflective grating, as used for the coherence transmissometer design, the grating equation is:

$$d(\sin\theta_i + \sin\theta_r) = p\lambda, \tag{12}$$

where d is the grating spacing, θ_i is the angle of incidence, θ_r is the diffraction angle, p is the diffraction order, and λ is the incident wavelength.

Other factors that can be tuned by the design of the grating are the diffraction efficiency into the primary order, the sensitivity of the grating to polarization changes, the sensitivity of the grating to angle of incidence changes, the amount of stray light reflected from the surface of the grating towards the primary diffraction order, and the separation provided between diffraction orders (ThorLabs, 2024). Although these parameters can vary within certain “types” of gratings (e.g., transmissive gratings with different diffraction angles can be selected), in general, reflective gratings tend to offer greater separation than transmissive gratings. As another example, blazed gratings typically exhibit greater diffraction efficiencies into diffractive orders greater than zero, compared to their non-blazed alternatives. The choice of grating in a given experiment should consider these factors and choose the option best suited to the experimental limitations and requirements.

In the coherence transmissometer prototype, a holographic reflective grating was chosen for its high diffraction efficiency, low amounts of stray light reflected, and relative lack of sensitivity to angle of incidence changes compared to other grating types.

3.2. Methods

To assess the performance of a diffraction grating-based transmissometer, hereafter called the coherence transmissometer, we made simultaneous optical power measurements, registered as voltages on the photodetectors, of a range of samples using this scheme and a set-up based on the design of a standard transmissometer with a collection angle of 0.9° in water, based on the WETLABS ac-9/s series of instruments which are considered a de facto standard in the marine optics community.

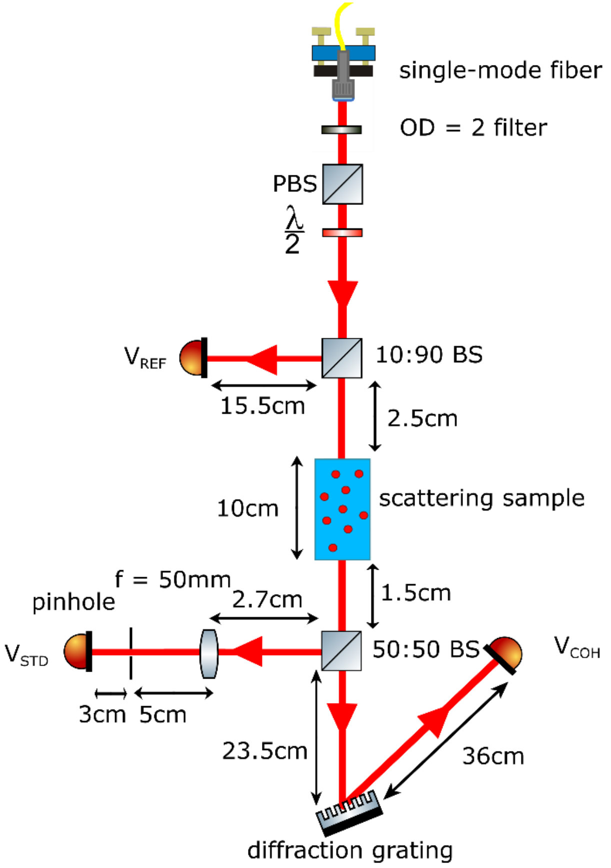

Figure 11: Initial prototype experimental set-up used to simultaneously measure attenuation through a sample using a standard lens and pinhole transmissometer and by measuring attenuation in the -1st diffraction order to filter out spatially incoherent light.

The description that follows relates to the first prototype iteration of the coherence transmissometer and simultaneous standard transmissometer system (Figure 11). For each sample, the beam was measured incident on photodetectors at three points, corresponding to the standard transmissometer, the coherence transmissometer, and a point prior to the sample used to measure changes in the output laser power. Simultaneous voltage logs were saved at all three points using a Picoscope analog-to-digital converter with 14-bit resolution.

To provide a reference for calculating beam attenuation, the cuvette was filled with pure water (Milli-Q, taken from a Millicore Simplicity water purification system with 18 MΩ resistivity, 0.2 µm filtration, and UV treatment, fed with distilled water and de-ionised) and the signal at all three measurement points was recorded.

3.2.1. Experimental set-up

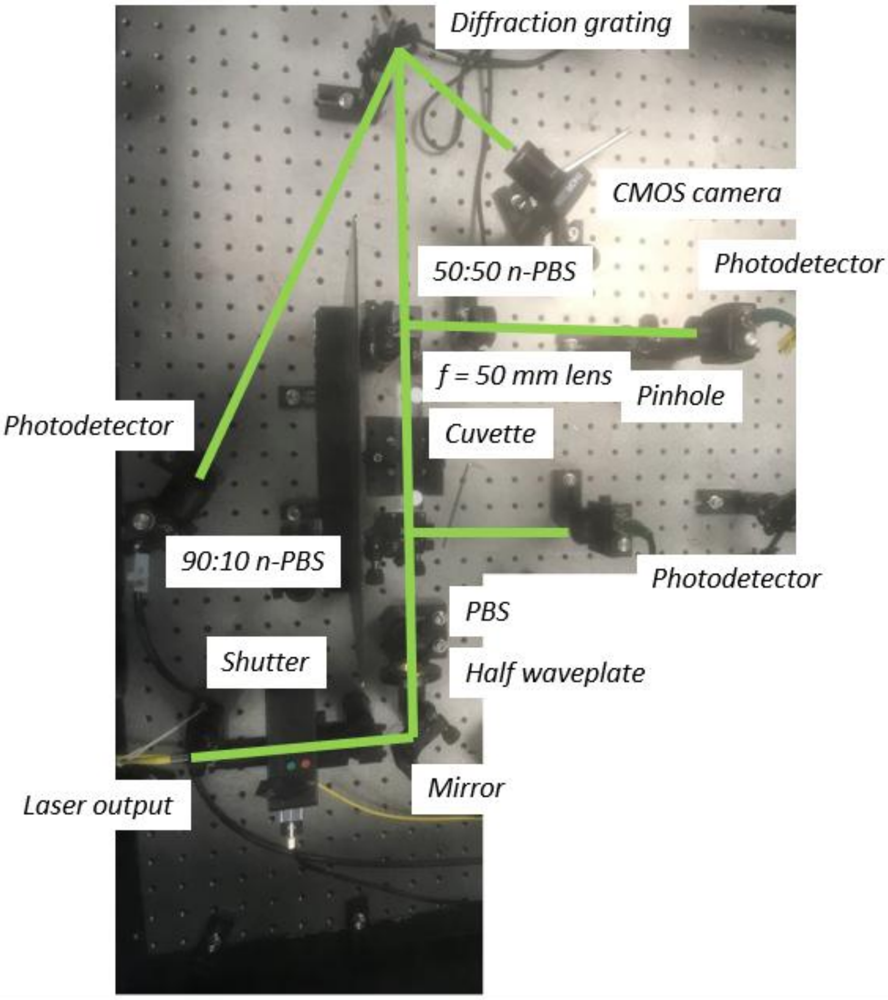

Figure 12: Photo of the laboratory set-up corresponding to the experimental diagram in Figure 11.

The experimental set-up used in the first iteration of the coherence transmissometer design is shown in Figure 11. The corresponding photo of the lab set-up is shown in Figure 12, with all components labelled.

A 662.5-nm diode laser was coupled into a single-mode fiber to produce the incident beam then collimated after the fiber output. The laser was driven at sufficiently high current to minimize temporal incoherence that occurs near the lasing threshold, then attenuated using a neutral density filter with an anti-reflective coating between 350 – 700 nm (OD = 2, ThorLabs NE20A-A) to bring the incident light levels within the dynamic range of the photodetectors (ThorLabs DET36A2, 3.6 x 3.6 mm active area, 14 ns rise time). A combined half waveplate (HWP) and polarizing beamsplitter (PBS) were used to control the incident beam polarization, which was chosen to optimize the diffraction efficiency of the holographic diffraction grating. The beam use had a clipped Gaussian profile (see Appendix A), a beam diameter of approximately 5 mm, and the divergence over the approximate path length of the full experimental set-up was calculated to be $\Theta = 7.69\mathrm{E}^{-4}$ mrad, which was calculated by comparing the $1/e^2$ beam width between two different points separated by 1 m for the beam propagating in free space. All lenses and filters used in this set-up had a diameter of 25.4 mm, unless specified otherwise, which is several times larger than the beam diameter. Prior to entering the scattering medium, 10% of the incident beam was picked off using a 10:90 non-polarizing beamsplitter (n-PBS) and recorded using a photodetector to monitor changes in the laser output power during the attenuation measurements (V_{REF}) (Figure 13).

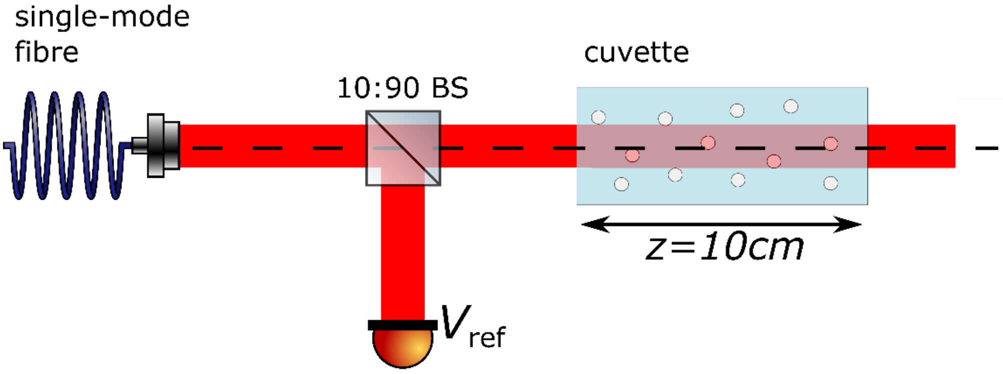

Figure 13: Zoomed-in, simplified view of the power calibration stage prior to the cuvette. Approximately 10% of the incident beam prior to the cuvette is picked off using a non-polarizing beamsplitter and measured using a photodetector. Any variations in this signal over the course of a measurement are used to calibrate changes in the transmissometer signals. The neutral density filter, PBS, and HWP have been excluded for simplicity, as their presence is not relevant to the power monitoring stage.

The scattering medium was held inside a cylindrical quartz glass cuvette with a 10-cm path length (Hellma 120-QS). The cuvette was mounted using a magnetic lock system that allowed the cuvette to be removed for sample changes and cleaning and subsequently replaced with minimal position changes.

After passing through the scattering medium, the beam was split into two experiment arms using a 50:50 n-PBS. The first arm contained the standard transmissometer (Figure 14). An $f = 50$ mm convex lens was used to focus the beam onto a pinhole that was placed at the focal plane, immediately followed by a photodetector for detection (V_{STD}). The collection angle of this set-up was chosen as 0.9° in water, approximately replicating the configuration used in the WETLabs/Seabird Scientific ac-9/s series of instruments which use an acceptance angle of 0.93° (Seabird Scientific, 2022).

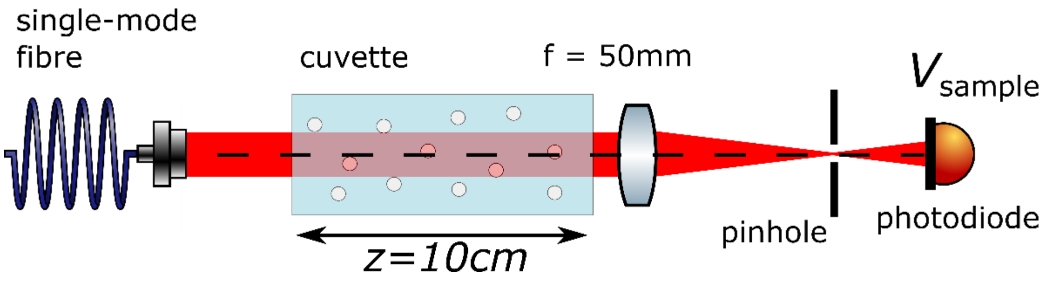

Figure 14: Zoomed-in schematic of the key parts of the standard transmissometer. After the cuvette, the light captured by the lens is focused down such that some collected angle of light passes through the pinhole to be collected by the photodetector. In the results presented in this chapter, the cuvette is 10cm long, there are elements for polarization control and power calibration prior to the cuvette, and a beamsplitter after the cuvette to direct some light to the coherence transmissometer.

The second arm passed the beam to a holographic diffraction grating with 1800 lines/mm (Figure 15). A set proportion of the coherent beam determined by the input beam polarization was diffracted into the –1st order diffraction mode and measured using a photodetector (V_{COH}). The rest of the coherent beam and all of the incoherent beam remained in the 0th diffraction order – separated from the –1st order. The initial hypothesis of this work was that all of the scattered light would be spatially incoherent with respect to the transmitted coherent light, preventing it from passing the diffraction grating used as a coherence filter. The position of the photodetector for the coherence transmissometer measurement was chosen based on logistical constraints of space relative to the other optics and the diffraction angle of the –1st order.

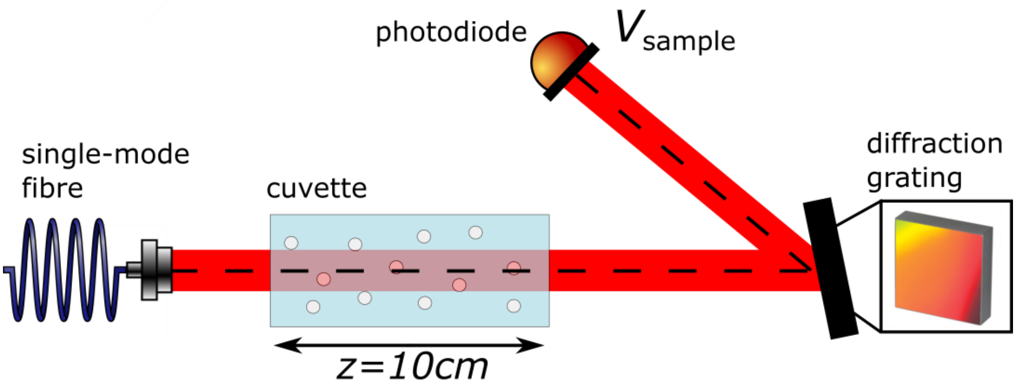

Figure 15: Zoomed-in schematic of the key parts of the coherence transmissometer. All that is required is a spatially coherent light source, a cuvette, a diffraction grating, and a photodetector. In the results presented in this chapter, the cuvette is 10cm long, there are elements for polarization control and power calibration prior to the cuvette, and a beamsplitter after the cuvette to direct some light to the standard transmissometer.

The zeroth order diffracted light was recorded using a CMOS camera (not shown in figure). This was monitored during the experimental process to check for any large misalignment problems after sample changeover. However, the intensity recorded at this point was not used for any of the attenuation calculations.

3.2.2. Sample handling

For the initial investigation into the transmissometer performance, two sample types were used: antacid solutions; and diatom solutions. For the antacid solutions, a highly attenuating stock of liquid antacid (Milk of Magnesia brand) and Milli-Q was made. This highly attenuating stock was then added in increasing concentrations to Milli-Q to make dilutions with attenuations ranging from 0.27 m^{-1} to 12.1 m^{-1}, as measured by the standard lens-and-pinhole transmissometer. It is important to note here that in general, the attenuation measured by the standard transmissometer has been taken as the fixed reference, since we did not have an independent way of measuring attenuation in the lab. All measurements made by the coherence transmissometer will later be compared to the reference measurement made by the standard transmissometer, which may have limitations in its exact alignment and calibration since this is not a commercial instrument. The antacid samples were chosen as they are commonly used to simulate the scattering behavior of natural water samples (Cochenour et al., 2016).

For the diatom samples (*Thalassiosira sp.*), an initial attenuation of 48.2 m^{-1} was obtained. The diatoms had an expected particle size range from 10 – 15 µm and were expected to be spherical, although imaging of their geometry was not performed for this initial proof-of-concept test of the transmissometer. Later, species with confirmed spherical geometries were used to characterize the transmissometer performance (Chapter 6). This original sample was then diluted using artificial seawater as a growth medium to cover a range from 2.9 m^{-1} to 48.2 m^{-1}.

For the attenuation measurements for each sample, the cuvette was filled with the sample of interest. Between each sample measurement, the cuvette was flushed out with fresh Milli-Q. The outer cuvette windows were cleaned and dried between measurements using methanol.

3.2.3. Data processing and analysis

3.2.3.1. Attenuation calculations

Simultaneous measurements of attenuation at the standard and coherence transmissometers are made by simultaneously acquiring voltage signals at two separate channels using the Picoscope. A third channel is used to measure approximately 10% of the laser power prior to the attenuating medium, to calibrate the voltages measured at each transmissometer to any changes in the laser power independent of changes in the attenuation of the sample.

The attenuation at each transmissometer is calculated following the same procedure. The procedure for calculation the attenuation at a given transmissometer from the initial, raw voltage signal is as follows.

The raw voltage signals at the standard transmissometer, coherence transmissometer, and power referencing point are saved as V_{std}, V_{coh}, and V_{ref}, respectively, for a total number of data points given by N. The average and standard deviation of these signals are saved as $\overline{V_{std}} \pm \sigma_{std}, \overline{V_{coh}} \pm \sigma_{coh}, \overline{V_{ref}} \pm \sigma_{ref}$. After each sample measurement, the shutter on the laser is closed, eliminating the incident light in the system. Under these conditions, background light measurements are acquired for N data points following the same procedure and processed to obtain: $\overline{V_{std,dark}} \pm \sigma_{std,dark}, \overline{V_{coh,dark}} \pm \sigma_{coh,dark}, \overline{V_{ref,dark}} \pm \sigma_{ref,dark}$.

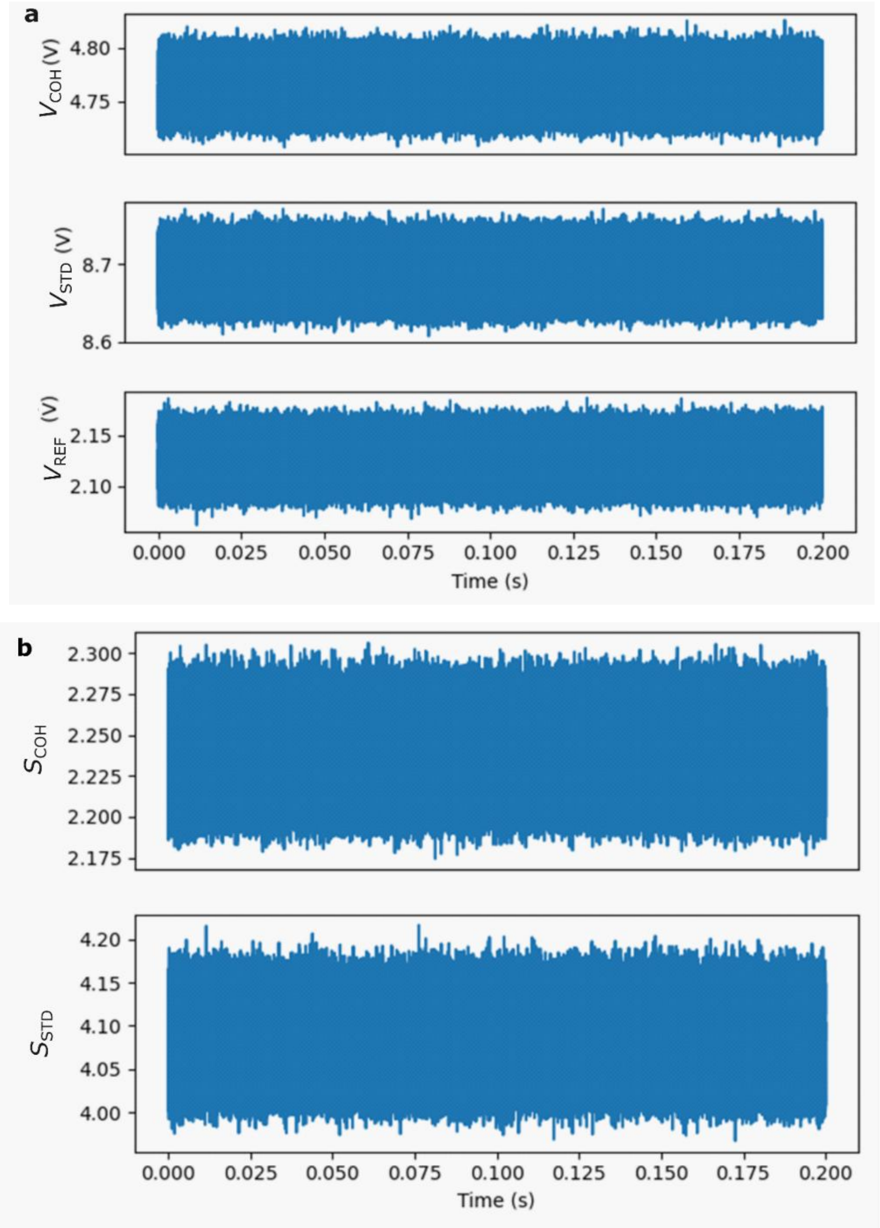

Figure 16: Voltage signals recorded during attenuation measurements. a. Unprocessed voltage signals recorded at 3 photodetector positions corresponding to the coherence transmissometer, standard transmissometer, and reference power prior to the cuvette (top to bottom). b. Voltage signals at the coherence transmissometer (top) and standard transmissometer (bottom) when calibrated to the change in laser power prior to the cuvette, for the case of a Milli-Q sample in the cuvette.

For each channel, the voltage associated with the background light is subtracted from the corresponding sample measurement. For example, for the standard transmissometer: $\overline{V_{STD}} = \overline{V_{std}} - \overline{V_{std,\,dark}}$, with the other terms following the same process and notation conventions.

To calibrate these voltage averages for each sample to any change in the incident laser power, the voltages are converted to calibrated signal values via:

$$\overline{S_{STD}} = \frac{\overline{V_{STD}}}{\overline{V_{REF}}} \tag{13}$$

The above procedure is performed for both the voltage signals measured with a scattering sample in the cuvette and those measured with fresh Milli-Q (MILLI-Q) in the cuvette as a blank. The attenuation at a given transmissometer is then calculated as follows:

$$c_{\text{STD}} = -\frac{1}{z} ln\left(\frac{\bar{S}_{\text{STD}}^{sample}}{\bar{S}_{\text{STD}}^{MQ}}\right), \tag{14}$$

where the above equation applies to the standard transmissometer and *z* is the path length through the cuvette.

To understand the behaviour of the coherence transmissometer with respect to the standard method, the ratio ($c_{\text{COH}}/c_{\text{STD}}$) of the two transmissometers is plotted as a key metric for performance.

3.2.3.2. Error estimation

Each voltage signal has a random error associated with it, alongside a resolution error due to the minimum change in voltage that can be measured by the Picoscope. The resolution limit of the Picoscope is a function of the bit depth of the scope and the dynamic range (*DR*) of the measurement, as follows (Parker, 2017):

$$resolution = \frac{DR}{2^{bit\ depth}}. \tag{15}$$

The Picoscope operates at 14-bit resolution when 3 channels are acquired simultaneously. For a dynamic range of 10 V, this corresponds to a minimum voltage resolution of 0.61 mV.

The standard error was taken for each voltage measurement, given by the standard deviation of the signal (σ) over the number of data points (N) (Hughes & Hase, 2010):

$$\alpha = \frac{\sigma^{N-1}}{\sqrt{N}}. \tag{16}$$

To get the total error in each voltage measurement, the standard error is propagated in quadrature with the resolution error of the Picoscope to get an overall error. For example, for the standard transmissometer:

$$(\varepsilon_{std})^2 = (\alpha_{std})^2 + (resolution_{std})^2. \tag{17}$$

To calculate the total errors in the attenuation measurements made by each transmissometer, the errors, ε, in each voltage must be propagated through the calculations. When errors are added to the same term (as above) or when the function is additive or subtractive, errors in each term can be added in quadrature. Any function with more complex operations requires a different approach. Using a calculus-based approach, as described by Hughes & Hase (2010), the general form for propagating error through a multi-variable function is given by:

$$(\varepsilon_Z)^2 = \left(\frac{\partial Z}{\partial A}\right)^2 (\varepsilon_A)^2 + \left(\frac{\partial Z}{\partial B}\right)^2 (\varepsilon_B)^2, \tag{18}$$

for a multi-variable function Z = f(A, B).

Eq. *(18)* relies on the key assumption that each term in the function is independent such that the errors in each term are uncorrelated. For correlated errors, the cross-terms between variable A and variable B must be included in the error propagation. For each stage of the error propagation for the attenuation calculations, two questions must be answered: if the errors can be propagated in quadrature or if they must follow Eq. *(18)*; and if the errors in each stage are independent or correlated.

To determine if any given two variables are independent, the correlation coefficient between the two variables must be calculated. Given a correlation coefficient, ρ_{AB}, the covariance between variables A and B can be calculated as (Bhandari, 2023):

$$cov_{AB} = \rho_{AB}\sigma_A\sigma_B. \tag{19}$$

These covariance terms can be replaced with error, ε.

The choice of correlation coefficient is dependent on a set of assumptions about the data. It is appropriate to use the parametric Pearson’s r only if: all data follows a normal distribution; the data has no outliers; the data is from a random or representative sample; both variables are on an interval level of measurement; and the relationship between the two variables is linear. If any of these assumptions fail, the non-parametric Spearman’s rho method can be used instead, which measures monoticity between the two variables as opposed to linearity.

For all channels, the measured voltage signals with the laser on were found to have normally distributed errors (Figure 17). A similar result was found for the corresponding background light signals.

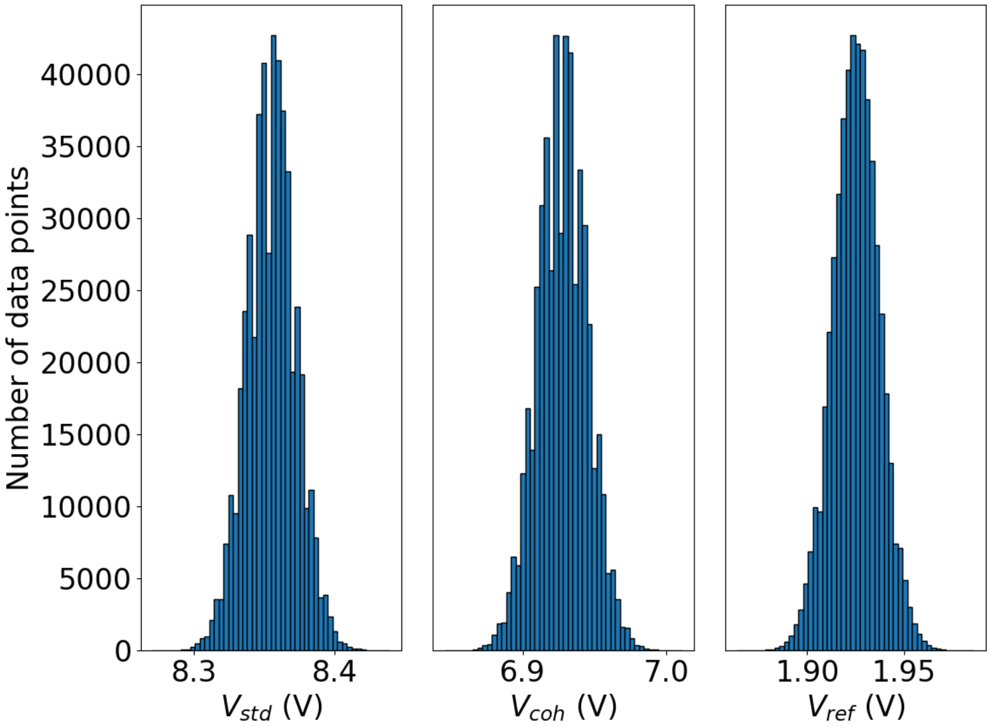

Figure 17: Distribution of voltage signals measured at each Picoscope channel during measurement of a representative scattering sample.

For the relationship between variables V_{std} and $V_{\mathrm{std,\ dark}}$, V_{STD} and V_{REF}, and $\bar{S}_{\mathrm{STD}}^{\mathrm{MILLI-Q}}$ and $\bar{S}_{\mathrm{STD}}^{\mathrm{Sample}}$, the Pearson's r coefficient can be used. For the relationship between c_{COH} and c_{STD}, the Spearman's rho coefficient must be used since linearity between the values cannot be assumed.

The error propagation calculations were split into subsequent steps, following the procedure for the attenuation calculations.

For the subtraction of background light from each voltage signal, the errors are propagated in quadrature since this is a subtractive relationship. For a representative channel (i.e., the standard transmissometer), the correlation between V_{std} and $V_{\mathrm{std,\ dark}}$ was found to be 0.0025 for a scattering sample measurement, such that cross-terms were not included in this error propagation stage. A correlation coefficient an order of magnitude lower was obtained with Milli-Q in the cuvette.

For the calibration step described in Eq. *(13)*, the correlation coefficient between V_{STD} and V_{REF} was found to be 0.0062 for a scattering sample and two orders of magnitude lower for Milli-Q. As such, the errors were propagated as in Eq. *(18)*, ignoring cross-terms between the variables.

For the attenuation calculation described in Eq. *(14)*, the correlation coefficient between $\bar{S}_{\mathrm{STD}}^{\mathrm{MILLI-Q}}$ and $\bar{S}_{\mathrm{STD}}^{\mathrm{Sample}}$ was found to be –0.00081, such that the errors were propagated without cross-terms as in Eq. *(18)*.

The final calculation step involves finding the ratio of $R = c_{\mathrm{COH}}/c_{\mathrm{STD}}$. For this step, the correlation coefficient between c_{COH} and c_{STD} was found to be large at 0.87. As such, cross-terms in the error propagation could not be ignored and Eq. *(18)* expands to become:

$$\left(\frac{\varepsilon_R}{R}\right)^2 = \left(\frac{\varepsilon_{c_{COH}}}{c_{COH}}\right)^2 + \left(\frac{\varepsilon_{c_{STD}}}{c_{STD}}\right)^2 - 2\left(\frac{\varepsilon_{c_{COH}c_{STD}}}{c_{COH}c_{STD}}\right) \tag{20}$$

for this specific calculation, based on Table 7.2 from (Hughes & Hase, 2010).

At this initial stage, variations in the absolute values of attenuations measured due to the quality of the Milli-Q sample could not be quantified, nor could changes in measured voltage due to changes in experiment alignment over the course of a data run. The effect of these variations will be discussed in Chapter 4: Optimization of a spatial-coherence based transmissometer.

3.2.3.3. Electronic and optical noise characterisation

Measurements of voltage are made for each transmissometer via a photodetector, which is connected via a BNC cable to a Picoscope, with a sampling rate of 1.98 MHz, which then captures voltage signals simultaneously for each transmissometer.

The inherent noise for each channel associated with this photodetector, BNC cable, and Picoscope set up when the laser is turned off such that no light should be present in the system is shown in Figure 18.

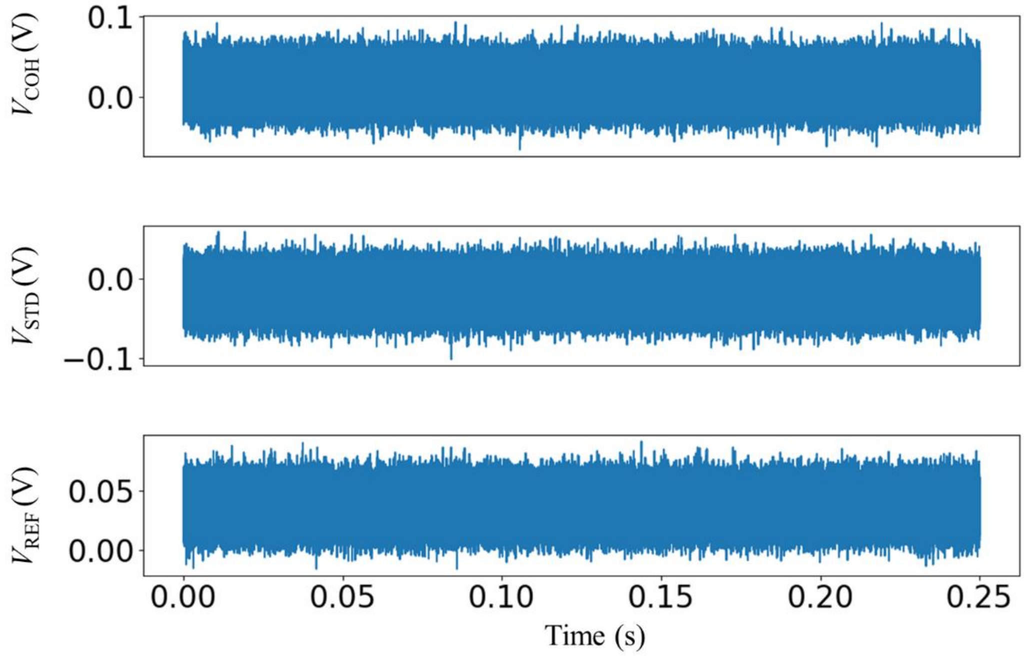

Figure 18: Unprocessed voltage signals measured at the coherence transmissometer, standard transmissometer, and power reference points by the photodetectors, BNC cables, and Picoscope channels when the laser is turned off.

For V_{coh}, the value of the background signal measured is 0.015 ± 0.017 V, with the error being due to the standard deviation of the background signal. For V_{std}, the measured background signal is –0.017 ± 0.017 V. For V_{ref}, this value is 0.037 ± 0.012 V.

The magnitude of this background signal can be dealt with by taking a dark measurement by blocking the incident laser power with a closed beam shutter. This background measurement for each channel is saved as a subfolder to the sample measurement and subtracted accordingly.

The source of this noise could be either electronic or optical. For example, a background light source with a standard deviation of this magnitude could be present in the system, despite efforts to eliminate background noise, and could be dominating the measured signal. Alternatively, this could be electronic noise inherent to either the photodetector, BNC connection, or Picoscope channel itself. To evaluate the source of this noise, voltage signals were acquired over the same time period for the case where the photodetector is disconnected from the system (measuring the noise inherent in the BNC and Picoscope channel combined) and for the case where the BNC cable is also disconnected from the system (measuring the noise inherent in the Picoscope channel only).

For the case with the BNC cables connected to the Picoscope channels, the measured voltages are V_{coh} = 0.011 ± 0.017 V, V_{std} = –0.019 ± 0.017 V, and V_{ref} = 0.030 ± 0.012 V. The magnitudes and standard deviations of the signal at each channel have not substantially changed, indicating that the primary source of noise in the voltage signals is due to electronic noise rather than optical noise.

For the case with nothing connected to the Picoscope channels, the measured voltages are V_{coh} = 0.009 ± 0.017 V, V_{std} = –0.020 ± 0.017 V, and V_{ref} = 0.026 ± 0.012 V. Again, there is not a substantial change in either the magnitude or standard deviation of the background signals measured at each channel.

The values of these background signals for each channel are summarized in Table 1.

Table 1: Background signals associated with the Picoscope, BNC cables, and photodetectors.

	Picoscope with BNC cables and photodetectors	Picoscope with BNC cables	Picoscope only
V_{COH} (V)	0.015 ± 0.017	0.011 ± 0.017	0.009 ± 0.017
V_{STD} (V)	–0.017 ± 0.017	–0.019 ± 0.017	–0.020 ± 0.017
V_{REF} (V)	0.037 ± 0.012	0.030 ± 0.012	0.026 ± 0.012

The above results indicate that the dominant source of signal noise in our system is due to the inherent noise associated with the Picoscope itself. To reduce the noise inherent in the unprocessed signals, a lower noise measurement device would need to be used. Another alternative approach which we choose to employ is to average over a large amount of data in order to reduce this inherent error (Hughes & Hase, 2010). This approach is appropriate if the data in question has a large standard deviation but is well-behaved over a large number of data points. The details of this approach and the final error magnitudes for a typical sample were described in Section 3.2.3.2.

3.3. Initial beam attenuation results

The attenuation values measured by each transmissometer for the liquid antacid and *Thalassiosira sp.* samples are discussed in this section. To evaluate the performance of the novel coherence-based method compared to the standard lens-and-pinhole method, the ratio of $c_{\mathrm{COH}}/c_{\mathrm{STD}}$ was plotting against c_{STD} as a key metric. Evaluating the performance of the coherence transmissometer against the standard transmissometer in this way, it could be seen that there was some nonlinearity to the relationship between the two transmissometers as a function of attenuation, rather than a fixed offset.

3.3.1. Liquid antacid attenuation measurements

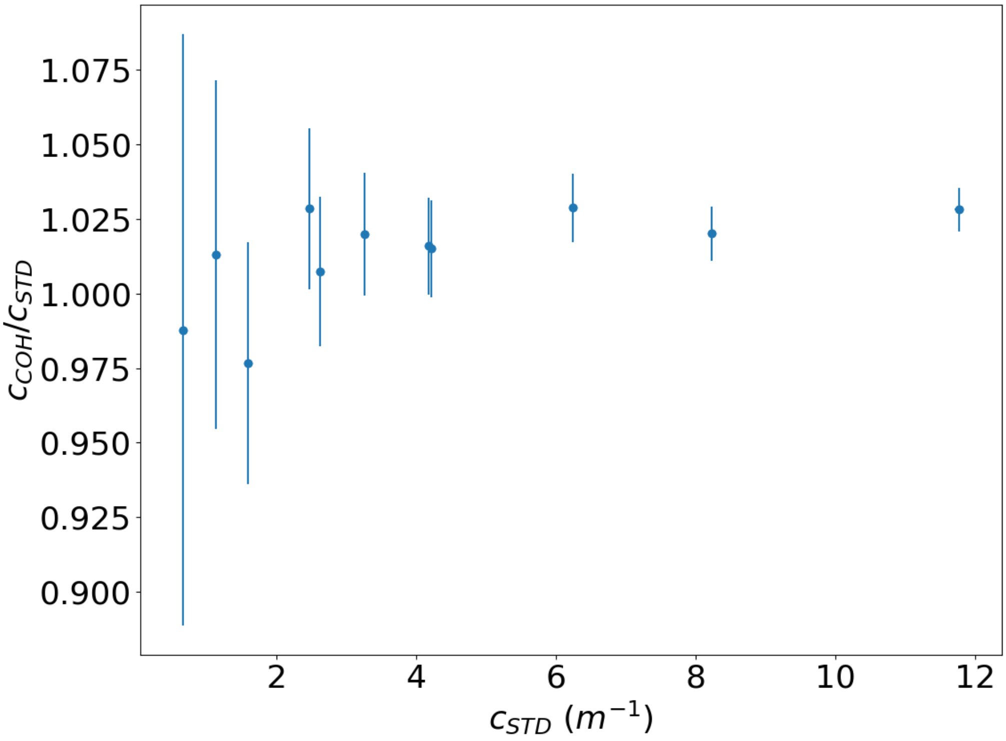

Figure 19:Ratio of attenuation estimates (c_{COH}/c_{STD}) made by the standard versus coherence transmissometers in a c_{STD} range from 0.66 ± 0.05 m^{-1} to 11.76 ± 0.05 m^{-1} for liquid antacid samples.

The ratio of the attenuations calculated for the two transmissometers for the liquid antacid samples was plotted as $c_{\mathrm{COH}}/c_{\mathrm{STD}}$ on the y-axis as a function of c_{STD} (Figure 19). If the transmissometers behaved the same and measured no difference in attenuation, a fixed ratio equal to 1 would have been expected. However, our initial hypothesis suggested that the coherence transmissometer should measure a higher attenuation than the standard transmissometer, due to the hypothesized elimination of forward-scattered light from the collection angle of the detector.

For a range of antacid samples with attenuations from 0.66 ± 0.05 m^{-1} to 11.76 ± 0.05 m^{-1}, the ratio of c_{COH} to c_{STD} varied from approximately 0.99 ± 0.10 to 1.03 ± 0.01. If the relationship between the transmissometers was to be fit across all attenuations, the coherence transmissometer measured a 2.32 ± 0.19% higher attenuation than the standard transmissometer over the measured range. Alley et al., (2018) similarly showed higher attenuation measurements (on the order of 10% higher) using their optical vortex-based transmissometer, although with a different scaling. However, this improvement becomes less clear at attenuations lower than approximately 3.5 m^{-1}, where the mean performance of the coherence transmissometer starts to gradually become worse with respect to the standard transmissometer. This behavior is also associated with a large increase in the error associated with these data points, suggesting that noise terms in the set-up are becoming increasingly dominant and lowering confidence in predictions of the coherence transmissometer performance at the lower end of the scattering regime.

3.3.2. Diatom attenuation measurements

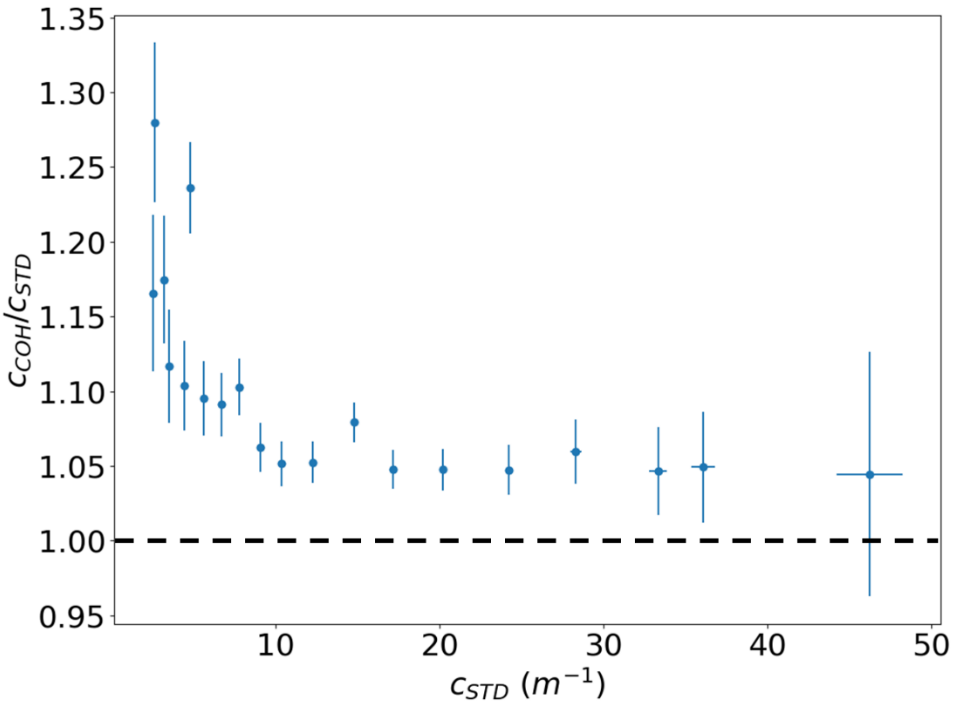

Figure 20: Ratio of c_{COH}/c_{STD} as a function of c_{STD} for Thalassiosira species diatoms with an estimated particle size between 10 and 15 microns. The correction from the standard to coherence transmissometer is highest at the lowest values of c_{STD} in the range, decreasing nonlinearly until approximately c_{STD} = 10.3 m^{-1} where a linear relationship between the standard and coherent transmissometers is achieved with a correction of approximately 4-5%. The black dashed line represents where c_{COH}/c_{STD} = 1.

Similar to the previous data for the liquid antacid samples, the attenuations calculated by the standard and coherence transmissometers were compared for a range of diatom samples (*Thalassiosira sp.*) with an expected particle size range from 10 – 15 µm (Figure 20).

The relationship between the two transmissometers is initially nonlinear at low c_{COH}, before stabilizing to a linear regime at approximately c_{STD} = 10 m^{-1}. Whereas at c_{STD} > 10 m^{-1}, the coherence transmissometer measures approximately 4–5% higher attenuation than the standard transmissometer, this difference is enhanced at lower c_{STD}. At c_{STD} = 2.6 m^{-1}, the coherence transmissometer measures approximately 22% higher attenuation than the standard transmissometer.

Interestingly, this nonlinearity at low attenuations appears in both Figure 19 and Figure 20 for the liquid antacid and diatom sample measurements, respectively. However, while this nonlinearity slopes towards a reduction in coherence transmissometer performance for the liquid antacid data, the performance curves up in the opposite way for the diatom data with an increasingly higher attenuation measured by the coherence transmissometer. This nonlinearity also appears over an increased attenuation range for the diatom samples, with a stable linear region only being reached at approximately 10.3 m^{-1} compared to at approximately 3.5 m^{-1} for the liquid antacid data. The difference in the sign of this trend, alongside the difference in range it covers for different datasets, points towards the presence of unbalanced noise or systematic error in the transmissometer system that is preferentially picked up by one transmissometer compared to the other. The differences between the liquid antacid and diatoms datasets also indicate that this source of noise may not be consistent from one dataset to another, resulting in markedly different transmissometer behaviours at low attenuations. However, clear conclusions cannot be drawn solely from this data since the error bars are also large at low attenuations. The origin of this noise will be investigated further in Chapter 4: Optimization of a spatial-coherence based transmissometer alongside a reduction in the error bars associated with the transmissometry measurements.

However, both datasets do demonstrate eventual stabilization of the coherence transmissometer performance past some threshold, where a linear relationship between the coherence and standard transmissometers can be obtained. In both of these cases, the coherence transmissometer measures a higher attenuation than the standard method once this stable, linear regime has been reached.

3.4. Discussion and next steps

3.4.1. Effect of particle size on transmissometer performance

Overall, there appears to be an increased bias measured for the diatom samples compared to the antacid samples. There is limited information available regarding parameters of the liquid antacid material, such as the size distribution of the sample. However, in the general case, we would expect to see the coherence transmissometer measuring an increasingly higher attenuation than the standard method for samples of increasing particle size.

It is a known effect that, for natural water samples, the magnitude of the volume scattering function at scattering angles < 1° is higher for larger particles. For example, in Figure 21, taken from Mobley (1994), large particles are shown to have a volume scattering function that is between 1–2 orders of magnitude stronger than that for small particles at scattering angles < 1°. In this case, small particles are defined as those with a diameter < 1 μm and large particles are defined as those with a diameter > 1 μm. The strength of the volume scattering function is theoretically expected to increase further in the micrometers to tens of micrometers range, particularly at small angles (Spinrad et al., 1978).

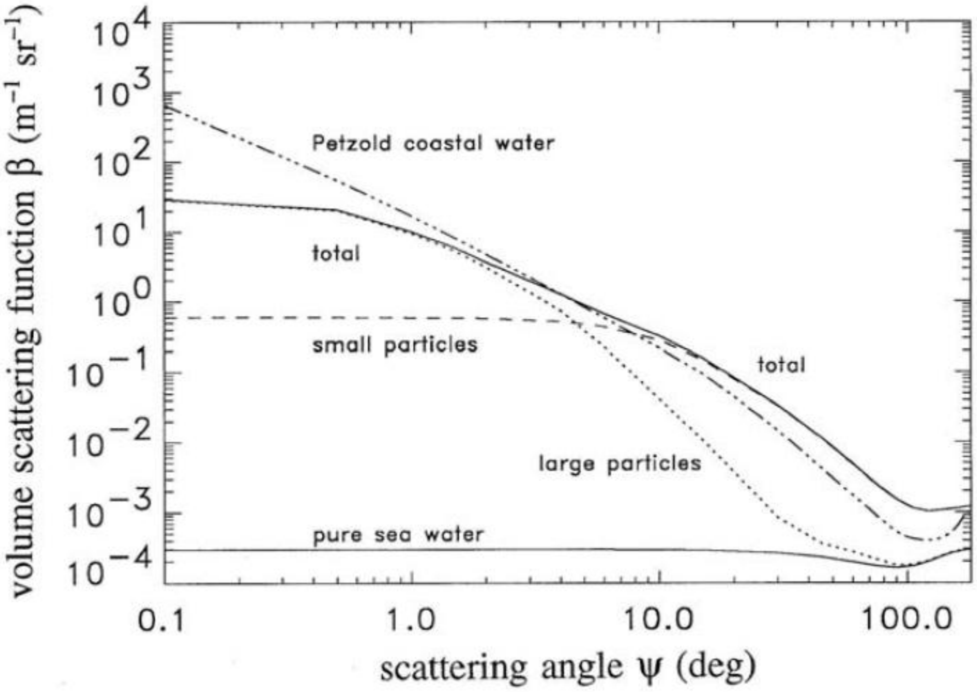

Figure 21: Figure taken from Light and Water by Mobley (Fig 3.18). It describes that large particles (dotted line) with a diameter greater than 1 micron have a steeper volume scattering function with a magnitude between 1 and 2 orders of magnitude greater at a scattering angle below 1 degree than that for small particles with a diameter less than 1 micron (dashed line) in natural water samples.

Since the volume scattering function becomes stronger at small angles for larger particle sizes, analyzing a sample with a larger average particle size would result in a larger difference in attenuation measured by the two transmissometers. This would be due to the standard transmissometer measuring an increased amount of forward scattered light for larger particles, whereas the coherence transmissometer would theoretically not detect any forward scattered light. However, it is not possible to conclude if this is the source of the difference in performance between the liquid antacid and diatom datasets in Figure 19 and Figure 20, since the liquid antacid samples do not have a well-defined particle size. Although the above data types were considered sufficient for a first rough indicator of the performance of the coherence transmissometer prototype, the amount of information about the coherence transmissometer performance that can be extracted from them is fundamentally limited without further knowledge of the sample properties. This limitation motivated the switch to a range of polystyrene bead samples with well-defined characteristics, including particle size, for the remainder of the research work of this thesis.

3.4.2. Effect of degree of scattering on transmissometer performance

As indicated in the previous section for particle size, we expect to be sensitive to changes in the volume scattering function when making a comparison between the coherence transmissometer and the standard transmissometer, due to the hypothesis that the coherence transmissometer will not pick up on angular distribution changes of scattered light. Therefore, other factors that could change the nature of the volume scattering function should be discussed for their potential effect on the attenuation measurements.

Piskozub & McKee (2011) showed that the scattering phase function is expected to broaden when moving from the single scattering to multiple scattering regime, when starting with an initially asymmetrical, steep scattering function. This is due to the relation between the asymmetry parameter for the *n*th degree of scattering (g_n) and the initial asymmetry parameter (g_1), which is:

$$g_n = g_1^n, \tag{21}$$

for $-1 < g < 1$. Values closer to a magnitude of 1 represent an increased asymmetry, whereas $g = 0$ indicates a completely symmetric, broad phase function. Eq. *(21)* tells us that an initially asymmetrical function with $g_1 = 0.99$ must eventually tend to an asymmetry parameter of 0 as the degree of scattering n increases. The degree of scattering needed to reach a broad, relatively flat scattering function is dependent on how asymmetric the initial scattering function is for single scattering ($n = 1$).

If this change in volume scattering function were to be present and picked up in our c_{COH}/c_{STD} measurements, we would expect it to appear as the coherence transmissometer measuring the highest difference in attenuation compared to the standard method at the lowest attenuation in the range. This difference would decrease with increasing scattering degree and eventually plateau at some fixed difference. Notably, this is the trend exhibited in Figure 20. However, the transition from the single to multiple scattering regime is approximately expected to occur between optical depths of 0.1 and 0.3 (Mobley, 2021), where the single scattering approximation diverges from observed behaviour, which in the current system with a path length of $z = 0.1$ m would occur at attenuations from 1 m^{-1} to 3 m^{-1}. The trend in Figure 20 does not plateau until approximately 12 m^{-1}, well into the multiple scattering regime. Although these comparative attenuation plots could theoretically be used to measure the transition from single to multiple scattering, we must ensure that we are free from the influence of any other bias terms that could cause the same behaviour in the attenuation regime of interest before drawing any conclusions regarding this phenomenon.

Chapter 4: Optimization of a spatial-coherence based transmissometer will focus on the optimization of this initial prototype of a spatial-coherence based transmissometer in order to identify and reduce sources of potential bias. Potential candidates for bias include the quality of the Milli-Q reference used and any changes in alignment as the cuvette is moved in and out of the set-up between sample measurements. These areas will be explored and optimized to attempt to improve the current set-up's sensitivity to noise and the relationship between the coherence and standard transmissometers will be monitored. The goals immediately after this initial set of measurements were to extend the stable linear $c_{\mathrm{COH}}/c_{\mathrm{STD}}$ regime to lower attenuations, investigate the nature of any nonlinearities in repeating datasets going forward, and to continue the analysis with a well-defined set of particles of known sizes.

Chapter 4: Optimization of a spatial-coherence based transmissometer

This chapter will focus on the identification and subsequent improvement of the coherence transmissometer prototype’s sensitivity to systematic bias and noise in the system. Addressing the appearance of systematic bias in the $c_{\mathrm{COH}}/c_{\mathrm{STD}}$ measurements is important such that changes in either transmissometer performance are not inaccurately attributed to a change in the measurement of scattering errors. Reducing the sensitivity of the experimental set-up to noise allows the measurement of attenuations at the extremes of the measurement regime where signals become more sensitive to noise: at high attenuations, where light levels are low; and at low attenuations, where the difference in light level between the sample and reference values are small.

Potential sources of systematic bias in the simultaneous transmissometer system include any effects which do not affect both transmissometers in the exact same way. For example, changes in the alignment of the cuvette could unequally affect the coherence and standard transmissometers due to the different optics and path lengths in each transmissometer arm. The presence of different optics in each transmissometer set-up could lead to one device being more affected by stray light than another. Additionally, due to the polarization-dependent efficiency of the diffraction grating, the coherence transmissometer is expected to be sensitive to any changes in the polarization of the light, whereas the standard transmissometer is not.

Several relatively simple changes could be made to optimize the signal-to-noise ratio, the accuracy, and the precision of the transmissometer measurements. For example, the signal-to-noise ratio at the coherence transmissometer was increased by choosing a diffraction grating with a higher efficiency of diffraction into the -1^{st} order. This allowed the voltage signal measured at the coherence transmissometer to be increased without increasing the overall laser power and saturating the photodetector at the standard transmissometer. The accuracy of the attenuation measurements was increased by taking background light readings immediately after every ultrapure water and sample measurement, as opposed to using a universal background light measurement for a full dataset to account for the possibility of a shifting background light level throughout the course of the measurements. The precision of the attenuation measurements was increased by time-averaging over a longer period (from an initial 50 ms to 500 ms), corresponding to an increased number of data points, which reduced the error in the voltage measurements via Eq. (16). The details of this chapter will focus on the sources of systematic bias and noise that required further evaluation to determine their effects on the system.

Prior to addressing the transmissometer sensitivity to any source of systematic bias, it is important to understand how sources of systematic bias are expected to appear in the results. The first part of this chapter will focus on the simulation of systematic bias in the $c_{\mathrm{COH}}/c_{\mathrm{STD}}$ results and efforts to identify these effects in the system.

Characterisation of the system is performed using a series of standardized polystyrene microspheres with known characteristics (Thermo Scientific Duke Standards 4000 Series Microsphere Size Standards and Thermo Scientific Duke Standards 2000 Series Uniform Polymer Microspheres). This also allows the performance of the transmissometers to be compared to Mie scattering calculations for homogenous polystyrene bead samples with these known characteristics, which will be carried out in Chapter 5: Observation of coherent scattering. This approach has been previously used in similar ways in the literature for evaluating, calibrating, and characterizing alternative instruments for measuring light scattering (Koestner et al., 2018; Sullivan and Twardowski 2009; Volten et al. 1998).

Prior to any of the transmissometer optimization techniques that will be detailed in this chapter, the performance of the coherence transmissometer with respect to the standard transmissometer was measured for polystyrene microspheres with a diameter of 0.994 ± 0.01 μm for c_{STD} values ranging from 0.35 m^{-1} to 58.77 m^{-1} (Figure 22). This provided a benchmark of the sensitivity and performance of the device against which the success of the optimization techniques could be compared. It can be seen that the error associated with the transmissometer measurements substantially increases as the attenuation values decrease below 5 m^{-1}. Similarly, the ability of the set-up to make comparative attenuation measurements at attenuations greater than 30 m^{-1} degrades as the absolute voltage signals measured decrease and become more susceptible to noise. The steps taken in this chapter will focus on reducing the noise sensitivity at low attenuations rather than that at high attenuations, since the low attenuation regime is considered to be more interesting and relevant to the typical values measured for natural waters. For example, maximum attenuation values for the Southern North Sea, which is considered to be highly turbid relative to other areas, can reach as high as 36.0 m^{-1} but more typical values lie in the regime of 10 – 20 m^{-1} (Astoreca et al., 2012). Comparatively, beam attenuation coefficients in relatively clear waters such as the Aegean sea are on the order of 0 – 0.8 m^{-1} (Anagnostou et al., 2024).

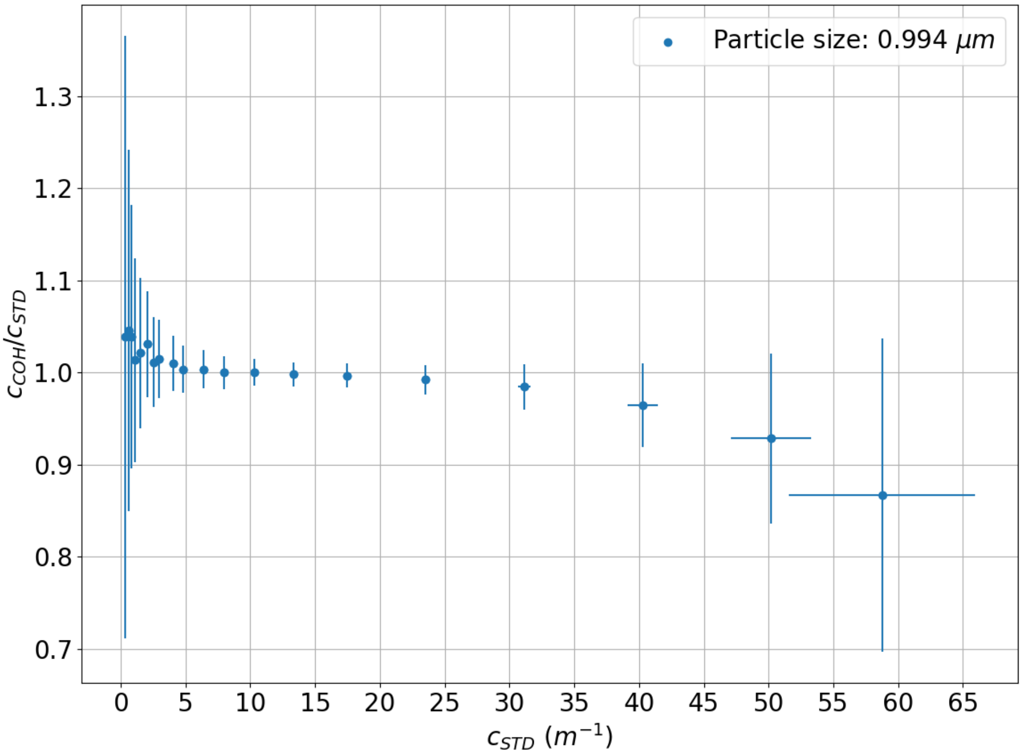

Figure 22: Performance of the coherence transmissometer with respect to the standard transmissometer for c_{STD} *values ranging from 0.35 m*$^{-1}$ *to 58.77 m*$^{-1}$*, for 0.994 µm polystyrene microspheres.*

Before moving forward, it is worth discussing the effect of the path length of the transmissometer on the sensitivity of attenuation measurements to noise. It is well known that the path length of the transmissometer is inversely related to the ability of the device to measure low attenuations. For example, devices with longer path lengths are better suited to making low attenuation measurements in relatively clear waters, whereas devices with smaller path lengths are better suited to more turbid waters (Boss et al., 2019). There will always be an ideal operating regime and water type for a given transmissometer, since it is inherently difficult to produce a transmissometer that works equally well over an extremely large dynamic range, such as that covered in Figure 22. If the sole purpose of this optimization procedure was to improve the transmissometer resolution at low attenuations, it would be appropriate to increase the path length of the cuvette above 10 cm, at the expense of sensitivity at higher attenuations. However, the main purpose of this optimization is to instead increase the range of attenuations covered by the regime where the $c_{\mathrm{COH}}/c_{\mathrm{STD}}$ measurements are linear with relatively low errors, to enable precise comparisons of the coherence transmissometer behaviour to that of the standard transmissometer. Changing the path length of the device would simply shift this window rather than extend it.

4.1. Identifying systematic bias

4.1.1. Attenuation of absorptive neutral density filters

In order to identify the presence of any systematic bias affecting the attenuation measurements, reference measurements through samples with well-known and predictable scattering and absorption behaviour can be used. At present, it is unknown if the scattering behaviour of the previous samples changed across the measured attenuation regime, resulting in the curvature in c_{COH}/c_{STD} at low attenuations, or if this curvature is the result of a systematic bias producing an offset in one or both transmissometers. This is because the expected scattering behaviour of the samples and the effect this would produce on the simultaneous transmissometer measurements is not well known. Although we expect that the observed curvature is not related to changes in the volume scattering function due to the persistence of the effect well into the multiple scattering regime, more investigation of the transmissometer performances for samples with well-known scattering and absorption behaviour can increase our confidence in this conclusion.

In practice, it is not trivial to obtain a set of standardized scattering samples whose effect on the attenuation measurements can be exactly predicted. Since this is a novel measurement system, the effect of changing scattering function on each transmissometer would have to be modelled to obtain an exact prediction. However, despite this limitation, it is possible to investigate the behaviour of a set of samples of known absorption (with negligible scattering contributions) on the attenuation measurements. This cannot provide us with information about how scattered light progresses differently through the two transmissometers. However, the presence of noise components unrelated to the angular or coherence variations in scattered light can be assessed using purely absorptive samples. For example, if the photodetector gain or noise level on each transmissometer differed, we would expect to see c_{COH}/c_{STD} substantially different from 1.

In measurements of absorption in marine optics, the use of Nigrosine as a known absorbing reference is common due to its broad absorption across the UV and visible spectrum. For example, calibrations of instruments designed to measure absorption such as the point source integrating cavity absorption meter (PSICAM) have been performed using calibration solutions composed of dilutions of Nigrosine in pure water (Lefering et al., 2018). However, using sets of Nigrosine samples of varying absorption introduces the need for bleaching of the cuvette after each sample measurement to prevent the dye from adhering to the cuvette walls. Additionally, producing a fixed set of absorption references across multiple datasets and substantial time periods via Nigrosine requires precise solution preparations to produce reproducible absorptive samples. For simplicity, we instead used a set of absorptive, neutral density (ND) filters in place of the cuvette, which could be moved easily in and out of the optical path and provided a fixed set of absorptive references across multiple datasets. Deviations to the beam path due to the introduction of each ND filter were assumed to be negligible, when the ND filter was placed orthogonal to the original beam path. This could be checked via the position of the beam on a camera placed at the 0th order before and after addition of the filter. In general, when placing the optics they were checked to be orthogonal to the direction of beam propagation by looking for the back-reflection to overlap with the incident beam exactly by eye.

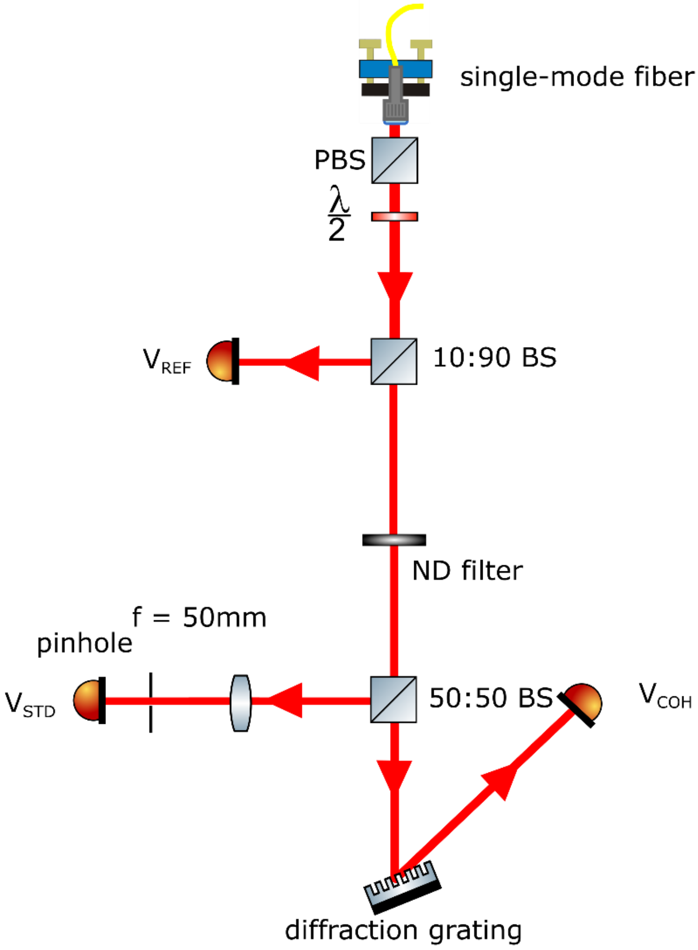

Figure 23: Transmissometry set-up for making simultaneous attenuation measurements through a standard lens-and-pinhole and novel coherence-based method, with an adaptation to remove the cuvette and replace with absorptive ND filters of varying optical density.

Table 2: Details of neutral density filters used in bias analysis.

ThorLabs Item Number	Optical density
NE01A-A	0.1 ± 0.01 @ 633 nm
NE02A-A	0.2 ± 0.01 @ 633 nm
NE03A-A	0.3 ± 0.015 @ 633 nm
NE04A-A	0.4 ± 0.02 @ 633 nm
NE05A-A	0.5 ± 0.025 @ 633 nm
NE06A-A	0.6 ± 0.03 @ 633 nm
NE10A-A	1.0 ± 0.05 @ 633 nm

The addition of the ND filters into the beam path in place of the cuvette altered the experimental set-up to that detailed in Figure 23: Transmissometry set-up for making simultaneous attenuation measurements through a standard lens-and-pinhole and novel coherence-based method, with an adaptation to remove the cuvette and replace with absorptive ND filters of varying optical density. A set of highly absorptive ND filters were obtained from ThorLabs (Table 2). Filters with optical densities of 0.2, 0.3, 0.4, 0.5, 0.6, and 1 were used as samples, with a filter with an optical density of 0.1 used as the reference measurement.

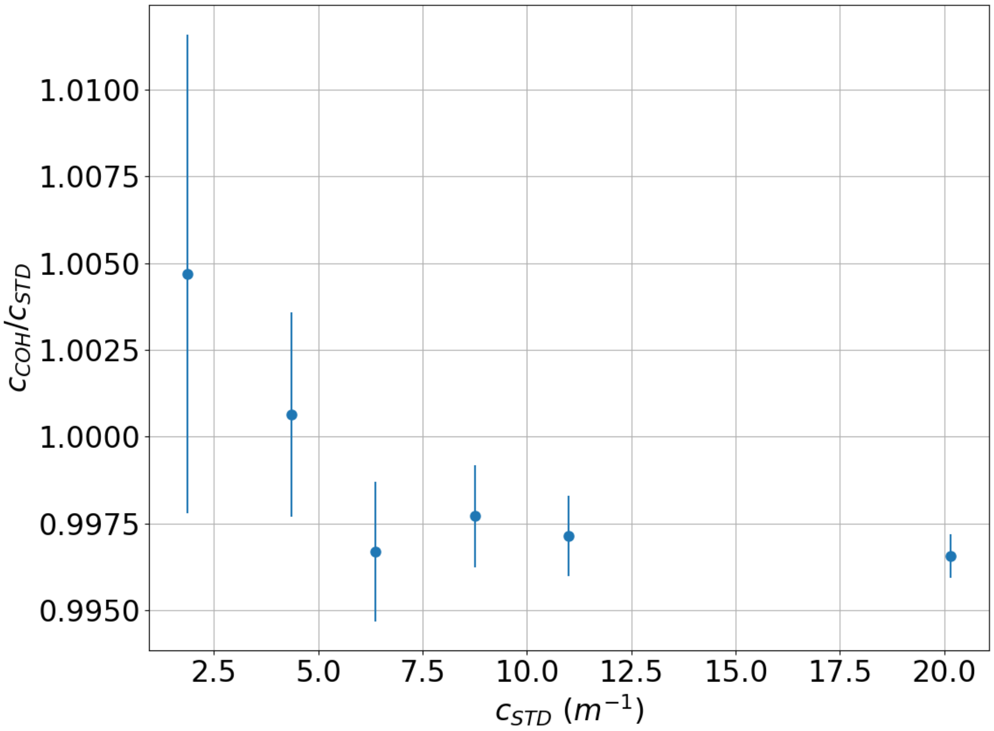

Figure 24: Ratio between transmissometer performance (c_{COH}/c_{STD}) as a function of attenuation (c_{COH}) when absorptive neutral-density filters are used in place of a cuvette containing a liquid scattering sample. Deviations on the order of ≈ 1% from perfect transmissometer agreement are seen, indicating the absence of offsets unrelated to scattering or coherence effects.

In Figure 24, we see that the ratio of c_{COH}/c_{STD} remains close to unity, with deviations approximately on the order of a percent at maximum. This indicates that we can be confident that any deviations of c_{COH} from c_{STD} greater than a percent point cannot be attributed to noise terms related to the photodetector gain or other fixed signal offsets in either transmissometer.

This does not suggest that the dual transmissometer system is perfectly calibrated and free from offsets, as there could still be unintended bias introduced associated with how each transmissometer propagates and measures attenuated light. For example, the above measurements were taken outwith the presence of the cuvette and do not account for deviations to the beam path due to cuvette movement. Additionally, any effects of a varying Milli-Q reference are not accounted for by this measurement.

4.1.2. Simulations of bias propagation

To give an insight into if a systematic bias introduced into the system would be capable of producing the nonlinear steep curve in $c_{\mathrm{COH}}/c_{\mathrm{STD}}$ observed in Figure 20, simulations of the effect of propagating a variety of errors through the system were performed.

The attenuation measured at the standard transmissometer can be expanded from that described in Eq. *(14)* as follows:

$$c_{\mathrm{STD}} = -\frac{1}{z} ln\left(\frac{V_{\mathrm{STD}}^{sample} + \varepsilon_{\mathrm{STD}}^{sample}}{V_{\mathrm{STD}}^{water} + \varepsilon_{\mathrm{STD}}^{water}}\right), \tag{22}$$

where $\varepsilon_{\mathrm{STD}}^{sample}$ and $\varepsilon_{\mathrm{STD}}^{water}$ are offsets associated with an undesirable bias added to the sample measurements and water measurements, respectively. In this case, the reference laser power V_{REF} is assumed constant such that the voltages do not need to be calibrated to S_{std} and S_{coh}.

The attenuation at the coherence transmissometer is calculated following the same expansion:

$$c_{\mathrm{COH}} = -\frac{1}{z} ln\left(\frac{V_{\mathrm{COH}}^{sample} + \varepsilon_{\mathrm{COH}}^{sample}}{V_{\mathrm{COH}}^{water} + \varepsilon_{\mathrm{COH}}^{water}}\right). \tag{23}$$

An investigation into the effect of adding an offset to the sample and water voltage measurements for each transmissometer was performed by increasing each offset term from zero independently, while the other terms remained fixed at zero (Figure 25). For example, in Fig. Figure *25*a, the effect of increasing the value of $\varepsilon_{\mathrm{COH}}^{water}$ from 0 to 10 mV in five steps on the $c_{\mathrm{COH}}/c_{\mathrm{STD}}$ measurements was mapped out. The same absolute offset values were added to $\varepsilon_{\mathrm{STD}}^{water}$ (b), $\varepsilon_{\mathrm{COH}}^{sample}$ (c), and $\varepsilon_{\mathrm{STD}}^{sample}$ (d). These simulations were carried out for fixed values of V_{STD}^{water}= 9 V and V_{COH}^{water}= 8 V, similar to real experimental values typically measured at each transmissometer. The effect of adding an increasing offset to the sample and water measurements in each transmissometer was evaluated for true attenuation values from 0.1 m^{-1} to 50 m^{-1}.

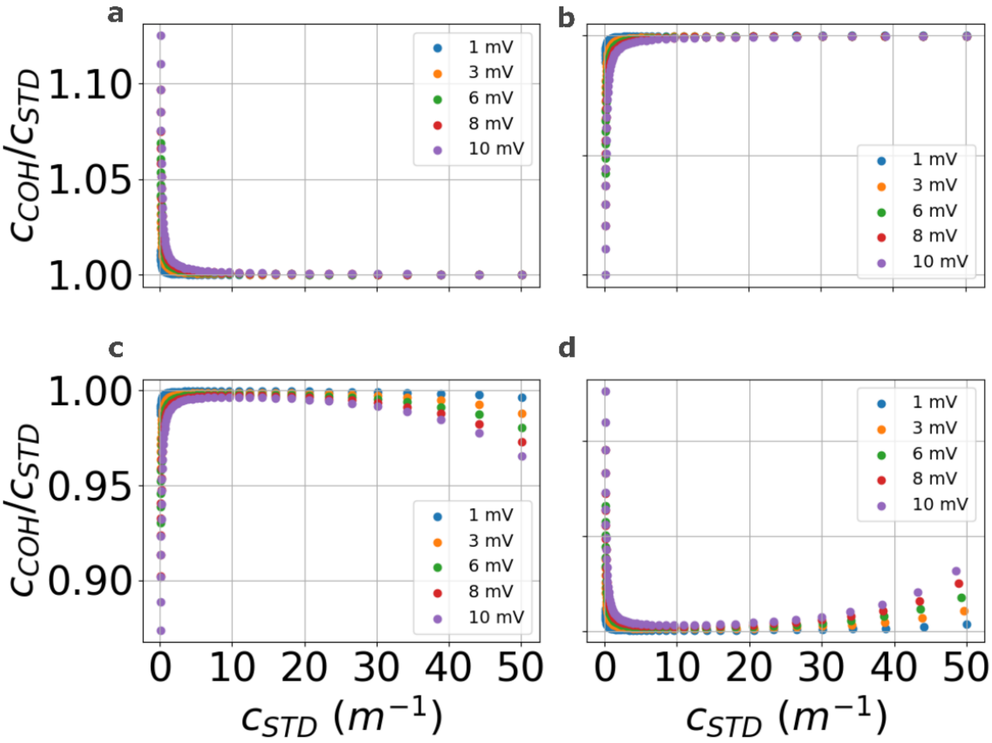

Figure 25: Simulation of how introducing an offset to the sample and reference terms in Eq.(22) and Eq. (23) would affect the behaviour of c_{COH}/c_{STD} as a function of c_{STD}. Simulations performed for values of V_{COH} = 8V and V_{STD} = 9V at Milli-Q. a. Effect of adding an increasing offset to the Milli-Q reference for the coherence transmissometer. b. Effect of adding an increasing offset to the Milli-Q reference for the standard transmissometer. c. Effect of adding an increasing offset to all sample terms for the coherence transmissometer. d. Effect of adding an increasing offset to all sample terms for the standard transmissometer.

The effects of increasing the values of these offsets from 0 to 10 mV can be seen in Figure 25. In all cases, as the offset value is increased from 0 mV, an increasingly steep nonlinear slope appears at the low end of the attenuation regime. For an added offset of 10 mV, the c_{COH}/c_{STD} diverges from 0 by an amount on the order of 10% in each of the above cases at the lowest attenuation value simulated of 0.1 m^{-1}. This simulated effect at low attenuations is similar to the measured experimental behaviour observed in Figure 20 for the diatom species. In Figure 20, the onset of nonlinear behaviour begins as the attenuation values measured decrease below approximately 12 m^{-1} and the c_{COH}/c_{STD} deviation measured at the lowest value in the regime is on the order of 20 %. This represents a larger deviation than that shown in Figure 25; however, the trend appears to be similar. It is easy to see how the introduction of a systematic bias equivalent in nature to one of the offsets simulated above could affect one or the other of the transmissometers and lead to the behaviour seen in Figure 20.

This type of nonlinear deviation between the performance of two optical devices at low values can also be seen in the literature for different IOPs. For example, the comparison between AC-s and AC-9 absorption measurements for the same sampling locations increasingly deviates from linear agreement at values lower than approximately 0.01 m^{-1}, considered to be the limit of the device sensitivity to temperature fluctuations and pure water calibration quality (Lefering et al., 2018).

However, a key point that can be observed in Figure 25 is that the areas most affected by the addition of offsets to each term in Eqs. (22) and (23) are at the low and high ends of the attenuation regime in all cases. In each scenario, there is a mid-range attenuation regime where the $c_{\mathrm{COH}}/c_{\mathrm{STD}}$ measurements are less sensitive to bias in the form of unequal offsets added to the voltage measurements. For example, in Figures Figure *25*a and b, a comparatively stable region of the $c_{\mathrm{COH}}/c_{\mathrm{STD}}$ measurement, where the device performances with respect to each other are relatively invariant on the addition of bias, appears above approximately 5 m^{-1}. In these scenarios, representing biases added to the pure water measurements, artefacts do not appear at the high end of the attenuation regime. In Figures Figure *25*c and d, representing biases added to the sample measurements, the comparatively stable region similarly appears above approximately 5 m^{-1}; however, in these cases, the coherence and standard transmissometer measurements begin to deviate due to the presence of bias again above approximately 20 m^{-1}. Both of these trends of deviating transmissometer performance at low and high attenuations are similar to the trends observed experimentally across multiple datasets. For example, Figure 22 displays both low and high attenuation deviations away from linear $c_{\mathrm{COH}}/c_{\mathrm{STD}}$ measurements.

The results of these simulations provide us with two main takeaways. First, it is possible for the presence of a systematic bias on either transmissometer as described by Eqs. (22) and (23) to produce similar nonlinear behaviour at low attenuations to that observed in Figure 20. Given that in the experimental data, this nonlinear behaviour persists well into the multiple scattering regime, it is more likely that this behaviour is consistent with the presence of bias in the measurements as described above than being correlated to changes in the shape of the volume scattering function with degree of scattering. Secondly, despite the ability of small systematic biases to substantially affect the $c_{\mathrm{COH}}/c_{\mathrm{STD}}$ measurements at low attenuations, in all cases there remains a mid-range attenuation regime where comparatively stable $c_{\mathrm{COH}}/c_{\mathrm{STD}}$ measurements can be made.

Going forward, this relatively flat regime will be used to evaluate the performance of the coherence transmissometer with respect to the standard lens and pinhole method. In the following sections, efforts to reduce the effect of environmental bias on both transmissometers are described, in order to extend this comparatively stable attenuation regime to as low attenuations as possible in the current set-up.

4.2. Sensitivity to alignment

The initial transmissometry set-up as described in Chapter 3: Initial transmissometer performance using a diffraction grating utilized a 10-cm cuvette that was mounted in a V-mount and held in place using a magnetic lock system to prevent changes in the cuvette position at axes both parallel and perpendicular to the direction of beam propagation. The magnetic lock was designed to return the cuvette to the exact same position each time the cuvette was removed and reinserted, minimizing changes in cuvette angle with respect to the beam propagation direction. Under the assumptions of cuvette position and angle stability using this set-up, the cuvette was removed from the system for sample transfer and cleaning between each measurement (for both Milli-Q and the attenuating samples).

However, although this set-up appeared to be sufficient for constraining the cuvette position, an increasing angular deviation of the cuvette was observed with each removal and reinsertion of the cuvette into the set-up. This could be visualised by placing a camera at the 0th diffraction order from the diffraction grating and monitoring the movement of the beam centre over the course of multiple measurements (Figure 26: Absolute displacement of pixel position of the 0th order beam, as measured on CMOS camera, as a function of sample number across 3 attenuation datasets for approximately 1–3 micron polystyrene beads. The centre of the 0th order was chosen by eye after averaging the beam intensity over 20 frames.).

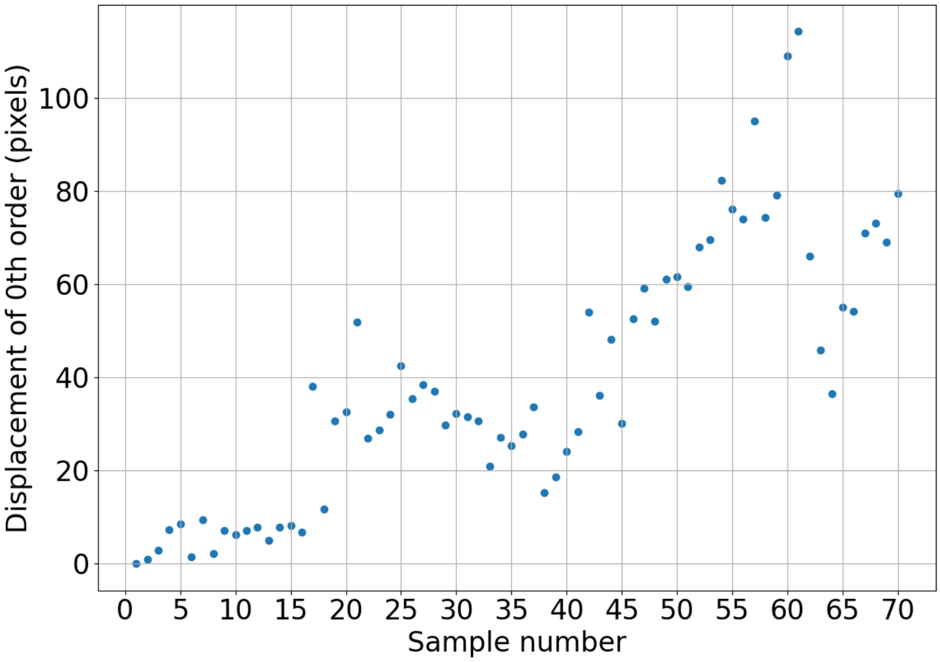

Figure 26: Absolute displacement of pixel position of the 0th order beam, as measured on CMOS camera, as a function of sample number across 3 attenuation datasets for approximately 1–3 micron polystyrene beads. The centre of the 0th order was chosen by eye after averaging the beam intensity over 20 frames.

Over the course of three sets of polystyrene bead measurements, 70 sample measurements were taken with corresponding images of the light beam at the 0th diffracted order recorded for each sample. Across all of the measurements, the beam was deviated at the 0th order from the original position by a maximum of approximately 110 pixels. For the CMOS camera in use (ThorLabs DCC1545M), each square pixel has a dimension of 5.20 by 5.20 µm. For a beam displacement of 110 camera pixels, this corresponds to a real displacement of 0.57 mm.

Although this does not seem like a large deviation of the beam position compared to the approximate width of the beam (5 mm, corresponding to an angular displacement of 0.64° measured from the cuvette to the camera), the change that this displacement may cause to the measured voltage signals could potentially be large enough to induce large changes in the $c_{\mathrm{COH}}/c_{\mathrm{STD}}$ measurements. A real displacement of 0.57 mm of the centre of a 5 mm-wide beam corresponds to a displacement of 11.4% relative to the total beam size. In the case of the coherence transmissometer, which does not utilize a focusing lens to focus the beam onto the active area of the photodetector (3.6 by 3.6 mm), the beam approximately fills the active area. Therefore, a movement of the beam of 11.4% could correspond to up to an 11.4% loss of voltage signal. As illustrated in the previous section, deviations on this order are capable of producing a large change in the $c_{\mathrm{COH}}/c_{\mathrm{STD}}$ measurements, particularly at low and high attenuations. Therefore, this persistent change in cuvette alignment had to be addressed. The actions taken will be discussed in combination with those described in the next section.

4.3. Sensitivity to attenuation reference

The values of attenuation measured at both transmissometers were seen to be sensitive to the Milli-Q measurement used as a reference. The influence of the Milli-Q measurement was observed to be strongest at the lowest attenuation values measured for the polystyrene bead samples. An example of this sensitivity is shown in Figure 27, where samples of 0.994 µm polystyrene beads with average attenuations ranging from 0.46 ± 0.08 to 42.9 ± 1.38 m^{-1} were measured by both transmissometers. For this data set, ten sets of fresh Milli-Q were measured in the cuvette independently, prior to making the attenuating sample measurements. The attenuations of each polystyrene bead sample were then calculated ten times using each of these Milli-Q measurements. While at higher attenuations (> 10 m^{-1}) there is not a substantial difference between the $c_{\mathrm{COH}}/c_{\mathrm{STD}}$ measurements made with each of the ten Milli-Q references, the $c_{\mathrm{COH}}/c_{\mathrm{STD}}$ measurements show large deviations at low attenuations for different Milli-Q references.

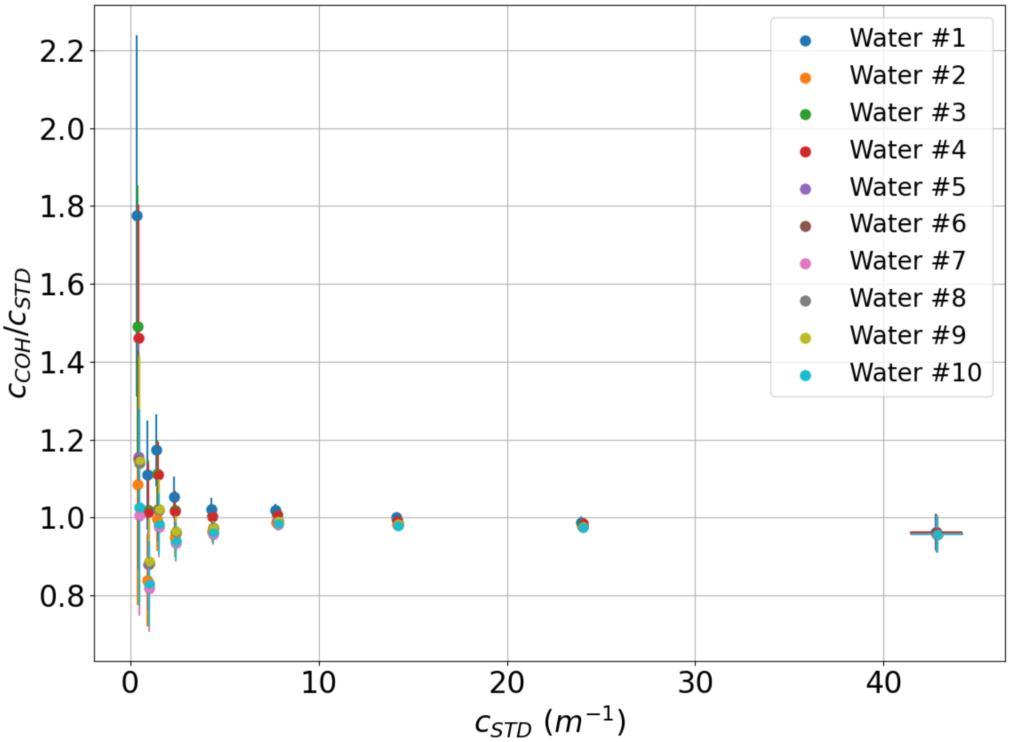

Figure 27: Variation in attenuations (c_{COH} and c_{STD}) measured for a set of 1μm polystyrene bead samples for a range of pure water (Milli-Q) measurements made prior to the attenuating sample measurements and used as a reference. The error bars are determined primarily as a result of the noise in each Picoscope voltage measurement propagated through the attenuation calculations, via the procedure laid out in Chapter 3.

At the lowest attenuation value in the range for each Milli-Q measurement, the attenuation measured at the standard transmissometer (c_{STD}) ranges from 0.36 ± 0.08 m^{-1} to 0.47 ± 0.08 m^{-1} and the ratio between the attenuations measured at each transmissometer (c_{COH}/c_{STD}) ranges from 1.77 ± 0.46 to 1.00 ± 0.26.

In the above case, the attenuation values measured for both transmissometers increased in line with the order of water sample used. One potential explanation for this is that the first water sample measurement contained contaminants picked up from the cuvette from the previous data run. After measurement, the first water sample was removed from the cuvette and disposed of. The next water sample was obtained from fresh purified water and placed into the cuvette before being measured. In theory, this repeated step when measuring new water samples is equivalent to repeated flushing out of the cuvette to dilute the presence of contaminants. This would result in the first water sample containing the highest presence of contaminants, resulting in the least difference between the water sample and polystyrene bead samples and a lower attenuation measurement for a given polystyrene bead sample. Whereas, the final water sample contains the lowest degree of contamination relative to the other water samples and so creates the highest attenuation measurements for the polystyrene beads when used as a reference. One thing that this particular data set indicates is that a high presence of contamination remains within the cuvette after previous data sets, which can be reduced by further flushing out of the cuvette with ultrapure water. However, reasonable variation in the $c_{\mathrm{COH}}/c_{\mathrm{STD}}$ measurements at low attenuations can also be seen across all data sets, even in cases where there is a less clear change in contamination level with sequential water samples.

Notably, not only do the range of $c_{\mathrm{COH}}/c_{\mathrm{STD}}$ measurements for different Milli-Q references increase at low attenuations, the error bars associated with each $c_{\mathrm{COH}}/c_{\mathrm{STD}}$ value for each Milli-Q become increasingly large at lower attenuations. This suggests that the resolution of the set-up for measuring and comparing two simultaneous attenuations becomes increasingly sensitive to noise at low attenuations and that the measurements are less reliable and reproducible – something that is corroborated by the substantial change in measured $c_{\mathrm{COH}}/c_{\mathrm{STD}}$ value with small changes to the reference Milli-Q.

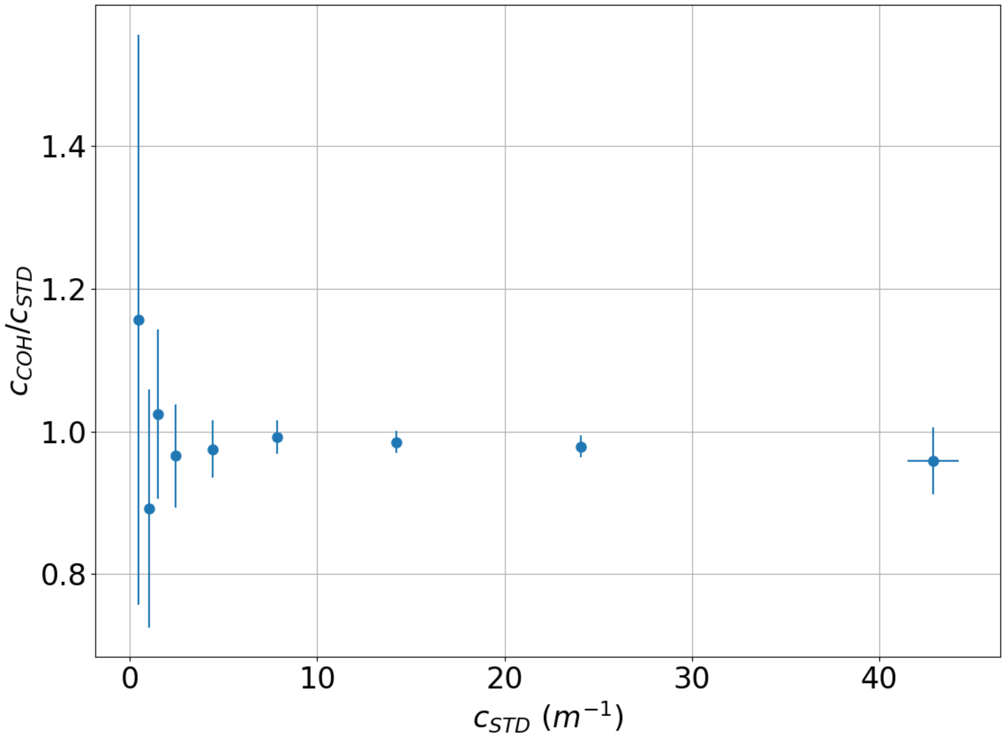

Figure 28: Attenuations measured for the set of 0.994 µm polystyrene bead samples shown in Figure 27, when the median of all of the Milli-Q measurements is used as a reference for calculating the sample attenuations.

When the attenuation values at each transmissometer and the ratio between the transmissometer performances ($c_{\mathrm{COH}}/c_{\mathrm{STD}}$) varies so much with the water reference used, it is impossible to know which set of calculations results in the "true" attenuation values. Although it may seem reasonable to conclude that the last in a sequence of water measurements is the least contaminated measurement and should result in the most “correct” attenuation measurements, this cannot be effectively concluded in the absence of a true attenuation measurement made independent of the experimental system in question. It is not trivial to obtain a true attenuation estimate: this requires a measurement technique that is completely free from error and systematic bias, in addition to being able to precisely maintain the composition of the sample between independent measurement techniques without dilution or the introduction of further contaminants. In the absence of a true attenuation measurement, leading to the inability to choose a single “correct” water reference, the method for determining the attenuations that are best representative of the system is to take the average or the median of range of water measurements. This average or median should then be used to calculate the attenuations of the attenuating samples. Going forward, the median is used rather than the average to exclude the influence of large outliers in the water measurements on the final attenuation measurements of the samples. The error associated with the median water measurement is taken as the standard error of the set of water measurements. For the multiple attenuation measurements made for multiple water measurements shown in Figure 27, the attenuations calculated for the same samples using the median of the water measurements are shown in Figure 28.

The level of variation seen in Figure 28 can be seen as a rough indicator of the level of noise in the experimental system and suggests that we cannot reliably measure reproducible attenuations below approximately 3 m^{-1}.

An important consideration is exactly why the use of different pure water references has the power to change the c_{COH}/c_{STD} results so substantially at low attenuations and if this effect can be minimized. One likely factor, as discussed in previous paragraphs, is a variable level of contamination of the fresh water samples with residual polystyrene bead solutions from previous experiments. It is also likely that contamination from other particles introduced by the environment (e.g., dust, fibres, etc.) are introduced to the water samples in the process of taking the ultrapure water from the machine and transferring them to the cuvette. However, the concentration of these types of contaminants is unlikely to be sufficiently high to cause a large change in the c_{COH}/c_{STD} readings. Placing new water samples into the cuvette should produce some amount of turbulence due to the force at which the water is placed in the cuvette. The amount of turbulence induced may be inconsistent across the range of water samples. Any turbulence present in the samples should be solely associated with the movement of the water sample as it is introduced into the cuvette: salinity and temperature differentials should not be present in the set-up when set up for measuring polystyrene bead samples (Bogucki et al., 2004). When taking ultrapure water from the machine and when transferring it to the cuvette, bubbles can be introduced to the samples which cause scattering – primarily forward scattering since the VSF is strongest at small angles for bubbles (X. Zhang et al., 1998; X. Zhang et al., 2002). Lastly, when the water samples were being transferred in and out of the cuvette, the cuvette was removed from the magnetic mounting set-up and then placed back into position.

To remove the sensitivity to the quality of the water samples discussed in this chapter, as many factors as possible should be minimized. The level of contamination from previous data runs with the polystyrene bead solutions can be minimized by increasing the amount of flushing out of the cuvette with ultrapure water between separate experiments. Increased efforts to minimize bubble production when taking and transferring water samples between different locations were made, primarily involving a slower rate of transfer and the rejection of any samples with visible bubbles. Finally, as also discussed in the previous section on alignment, despite attempts to produce a secure and reproducible cuvette mounting set-up, the potential remained for cuvette rotation whenever the cuvette was removed for cleaning and sample transfer. Going forward, the cuvette remained in a fixed position throughout all experimental runs, without removing the cuvette for cleaning or sample transfer. Instead, the samples were removed and placed into the cuvette via pipette while the cuvette remained in place in the experimental set-up. While this may have made it more difficult to remove contaminants at the edges of the cuvette, this was considered to be a less important factor than the potential of cuvette rotation and corresponding transmission changes during a data set.

4.4. Assessing sensitivity to polarization

There is an associated effect of polarization change with the scattering of light that has been utilized in marine optics to identify the presence of difference particle types, such as minerals and phytoplankton, in natural water samples (Bickel & Bailey, 1985). This change of polarization with scattering is better described by the Mueller matrix, which describes both the intensity and polarization of the light (Voss & Fry, 1984), than by the VSF. Since the device presented within this thesis is heavily reliant on the use of a diffraction grating, which has a polarization dependent efficiency, it is important to understand if the level of polarization change from scattering at forward angles (< 1°) from spherical, polystyrene beads is large enough to influence the nature of the results.

Due to the polarization control stage prior to the cuvette consisting of a HWP and PBS (95:5 T:R), the light incident on the cuvette is linearly polarized. The HWP is fixed in position to transmit light with a linear polarization angle corresponding to the maximum grating efficiency into the –1st diffractive order. As such, any change to this polarization state would result in a reduction of diffraction efficiency at the grating. A loss of efficiency at the diffraction grating could be caused by any of the following: a depolarization of the incident light as a result of scattering; a change in the angle of linear polarization due to scattering; or an introduction of circular polarization.

The degree of linear polarization ($DoLP_p$) of a particle describes the ability of the particle distribution to induce a linear polarization on an initially unpolarized beam (note that the subscript *p* indicates that this property relates to the particle). A $DoLP_p$ equal to 1 indicates completely perpendicular polarization, a $DoLP_p$ equal to –1 indicates completely parallel polarization, and a $DoLP_p = 0$ indicates no change. Koestner et al., (2018) demonstrated that the maximum $DoLP_p$, describing maximum change in polarization due to scattering, found for natural particle samples taken from clear, coastal, and turbid waters peaks at a scattering angle of approximately 90° for all water types considered, as measured by a LISST-VSF device. The magnitude of the maximum $DoLP_p$ in each case was seen to decrease in samples with higher proportions of larger particles. In another study, $DoLP_p$ and the P_{22} element of the Mueller matrix, which is associated with particle scattering, tended to 0 and 1, respectively, as the scattering angle approached 0° for polystyrene beads measured using a LISST-VSF device (Koestner et al., 2020). These values refer to scenarios of no polarization change. However, the actual values of these variables are not measured below 15° by a LISST-VSF, as a consequence of a general understanding in the field that the strongest changes to polarization due to scattering happen at larger angles in the backscattering regime rather than in the forward-scattering region. The manufacturer’s website notes that the P_{22} parameter describing polarization changes due to particle scattering is 1 at all angles for spherical particles (Sequoia Scientific, 2017).

On the other hand, Y. Zhang et al. (2019) describe a decrease in the DoP of linearly polarized light when it interacts with underwater particles (such as algae or sand) with increasing particle size. The magnitude of polarization loss is on the order of 5% at 50 µm over 5 m and is acknowledged to be a function of the path length. Although this indicates that polarization loss from marine particle scattering is possible, it is likely to be more of a problem for underwater communications applications that use long distances but unlikely to be substantial at 10 cm. Furthermore, Cochenour et al. (2010) measured the DoP loss from scattering from Maalox particles and indicated that large DoP loss did not initiate until around $cz > 10$ for all scattering albedos which is a much higher attenuation threshold than used in this study.

Due to the generally accepted low amounts of polarization change from scattering in the forward direction from homogenous, spherically symmetric particles in the Mie regime, it is considered unlikely that a large enough depolarizing effect (or a change in the linear polarization angle) could occur on scattering to produce a large difference in performance between the standard and coherence transmissometers at the angles of light collected by each device (< 1°) and so no steps were taken to account for polarization changes due to scattering in this study.

However, the expected polarization behaviour has not been modelled or measured in this study, which is a limiting factor. Future studies of the behaviour of the coherence transmissometer could involve modelling the expected loss in measured light due to changes in polarization. The Stoke’s parameters of the light through ultrapure water could also be experimentally measured and compared to measurements of the Stoke’s parameters of light after propagation through polystyrene bead samples at sizes and attenuations used within this study.

4.5. Optimized attenuation measurements after sensitivity improvements

As discussed in the previous subsections, progressive changes to the alignment of the cuvette in the transmissometry set-up were theorised to be introducing a measurable amount of bias in the $c_{\mathrm{COH}}/c_{\mathrm{STD}}$ measurements, particularly at low attenuations. This potential effect was indicated by the progressive change in beam position measured by a camera placed at the 0th diffracted order (Figure 26) and by the variation in $c_{\mathrm{COH}}/c_{\mathrm{STD}}$ measurements made when a range of different ultrapure water references were used, which coincided with the cuvette being moved in and out of the system. Although the main approach to fix this alignment sensitivity was to transition to a procedure where the cuvette remained fixed in place throughout an entire experimental data run and the ultrapure water and attenuating samples were transferred on the optical table, an additional attempt was made to reduce alignment sensitivity at the coherence transmissometer by placing a lens between the diffraction grating and the photodetector (Figure 29).

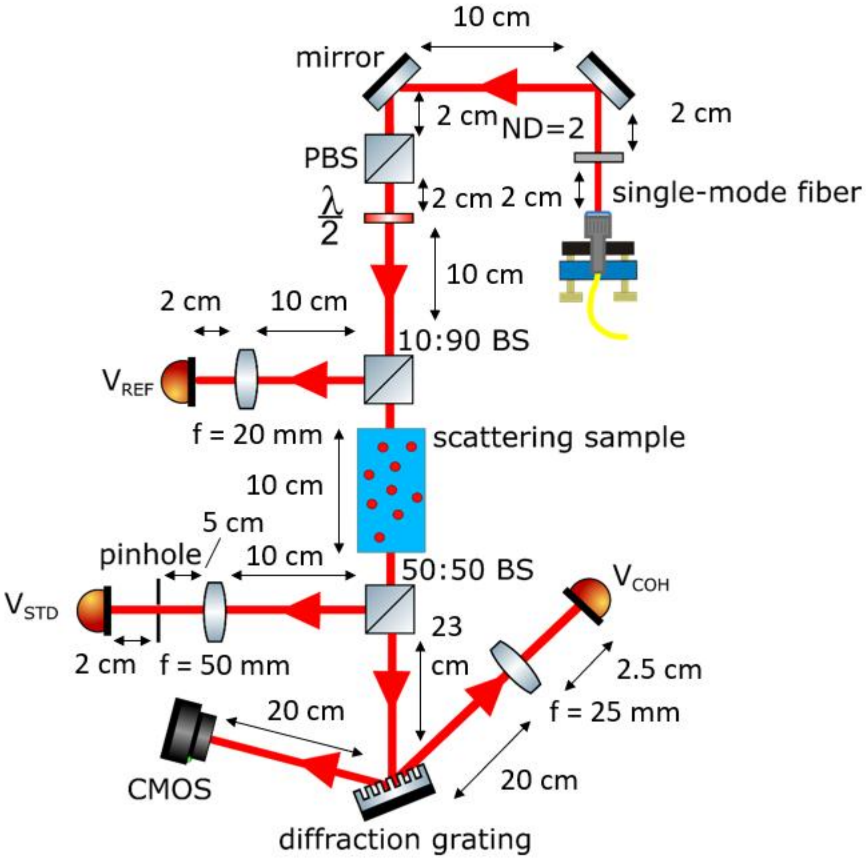

Figure 29: Depiction of the physical changes made to the experimental set-up after optimization, including the addition of a focusing lens between the diffraction grating and photodetector of the coherence transmissometer, a camera for monitoring beam alignment at the 0th diffraction order, and two mirrors after the output of the laser to allow fine control of alignment. Drawing dimensions are not to scale.

The addition of the lens was to focus the diffracted light onto a smaller area of the photodetector, minimizing the effect of any change in direction of beam travel on the voltage signal measured at the photodetector. Since the initial theory was that the coherence transmissometer only measured spatially coherent, transmitted light, the addition of the lens was not expected to change the amount of scattered light collected.

To summarize the main advancements of this chapter, the transmissometry set-up was optimized to improve sensitivity at low attenuations and accuracy of $c_{\mathrm{COH}}/c_{\mathrm{STD}}$ results by taking the following steps. Multiple ultrapure water measurements were made prior to all attenuating sample measurements and the most accurate $c_{\mathrm{COH}}/c_{\mathrm{STD}}$ measurement was considered to be that which was calculated using the median ultrapure water measurement. Sensitivity of the measurements to changes in the alignment of the cuvette was minimized by transitioning to an experimental procedure involving a fixed cuvette, rather than a cuvette that was moved in and out of the system for sample transfer and cleaning between measurements. Larger amounts of data were saved for each measurement, to improve the precision of each voltage measurement. Background light levels were measured and subtracted after every sample measurement, rather than using a universal background light measurement for all samples in a data run, to improve measurement accuracy. The light levels reaching each photodetector were maximized, improving the transmissometer sensitivities. Finally, the focusing lens was added to the coherence transmissometer to reduce sensitivity to cuvette alignment, as indicated in Figure 29.

Table 3: Parameters associated with polystyrene microspheres used to characterise transmissometer performance.

Diameter (µm)	Standard deviation of particle size distribution (µm)	Refractive index	Microsphere composition	ThermoFisher Catalogue Number
0.994 ± 0.01	0.01	1.59 @ 589 nm	Polystyrene	4009A
5.0 ± 0.3	0.6	1.59 @ 589 nm	Polystyrene Divinylbenzene	2005A
10.07 ± 0.06	0.09	1.59 @ 589 nm	Polystyrene	4210A
20.01 ± 0.33	0.26	1.59 @ 589 nm	Polystyrene	4220A

With the newly optimized transmissometry set-up, measurements of the attenuation of a standardized set of polystyrene beads were made by both transmissometers, from 0.994 to 20.01 µm (Table 3). This data is also displayed graphically in the next chapter, in *Figure 30*.

When making attenuation measurements to compare the two transmissometers, several behaviours must be analysed. For example, the average absolute value of c_{COH}/c_{STD} gives an indication of the difference in attenuation measured by the transmissometers. However, for analysing the measurement capabilities of the transmissometer set-up, the following two parameters provide the most information. First, the c_{STD} range over which there is a linear relationship between c_{COH} and c_{STD} indicates the reproducible, operable range of the transmissometer set-up. An increase in this operable range towards lower values of c_{STD} indicates a reduction in sensitivity to systematic bias, as discussed throughout this chapter. Second, the error bars associated with the c_{COH}/c_{STD} measurements indicate the precision with which the experimental set-up can measure the difference between the two attenuation measurements, which is important for making accurate predictions of the coherence transmissometer's performance.

The linearity and precision of the c_{COH}/c_{STD} measurements will be discussed first, as understanding and optimizing the sensitivity of this transmissometry set-up to bias has been the key focus of this chapter. The absolute values of the coherence transmissometer measurements for the range of polystyrene microspheres will be discussed further in the next chapter.

For all polystyrene microsphere sizes, the linearity of the c_{COH}/c_{STD} measurements remain fairly stable with decreasing attenuation until at least approximately 2 m^{-1} (Table 4). Below this attenuation, the c_{COH}/c_{STD} relationship becomes increasingly nonlinear with decreasing c_{STD} for the 0.994 ± 0.01 µm microspheres, considered to be a sign of at least one of the transmissometers performing outside its operable range. For the other microsphere sizes, large deviations from a linear c_{COH}/c_{STD} relationship do not begin until the attenuation decreases below approximately 1 m^{-1}. This is a strong improvement in the measurement resolution and sensitivity of this transmissometry set-up, compared to the case shown in Figure 22 for the same set of 0.994 ± 0.01 µm microspheres. In the case shown in Figure 22, the divergence of the c_{COH}/c_{STD} relationship from linearity occurs at values lower than approximately 5 m^{-1}.

Table 4: Description of the linearity and precision of polystyrene microsphere measurements made using the coherence and standard transmissometers.

Diameter (µm)	Operable c_{STD} range where c_{COH}/c_{STD} is linear (m^{-1})	Precision in c_{COH}/c_{STD} at lowest c_{STD} in operable range (%)
0.994 ± 0.01	1.96 – 14.31	0.50
5.0 ± 0.3	1.1 – 9.6	0.3
10.07 ± 0.06	1.20 – 8.19	0.13
20.01 ± 0.33	0.87 – 9.17	2.82

The data shown in Table 4 across a range of polystyrene microspheres sizes represents up to a factor of five improvement in device sensitivity to bias at low attenuations compared to measurements of the same microspheres prior to transmissometer optimization. The precision of these measurements has also been substantially increased, with the lowest c_{COH}/c_{STD} value in the operable range for the 0.994 ± 0.01 µm microspheres demonstrating an error of ± 0.50% at 1.96 m^{-1} in the optimized case as opposed to demonstrating an error of ± 5.92% at 2.08 m^{-1} in the unoptimized case as shown in Figure 22. This represents an approximately order of magnitude improvement in measurement precision at similar attenuations regimes from the unoptimized to optimized case.

This improvement in the operable measurement regime, represented by the sensitivity of the c_{COH}/c_{STD} measurements to systematic bias, and the precision, represented by the error associated with the c_{COH}/c_{STD} measurements, of the transmissometry set-up indicates that the steps taken and described in this chapter have been worthwhile towards making a more robust-to-noise transmissometer. The optimized transmissometer with an improved signal-to-noise ratio and increased operable range will be used going forward to produce more precise and reliable measurements of the coherence transmissometer performance with respect to the standard lens-and-pinhole method.

Chapter 5: Observation of coherent scattering

The original principle used in the design of the coherence transmissometer was that the scattering from particles typically found in marine environments was expected to induce close-to-complete spatial incoherence (Alley et al., 2018) on an initially spatially coherent beam, with negligible amounts of spatial coherence remaining. Under this assumption, a coherence-dependent optic such as a diffraction grating could be used to isolate a portion of the spatially coherent light associated with transmission from the scattered light, allowing an attenuation measurement. The ability for this system to remove the detection of scattered light and effectively have a collection angle of 0° is dependent on the scattered light retaining only a negligible amount of spatial coherence.

Although values representing the precision and stability of the c_{COH}/c_{STD} measurements for a range of polystyrene microspheres with sizes from 0.994 ± 0.01 µm to 20.01 ± 0.33 µm microspheres were discussed at the end of the previous chapter, the behaviour of these particles as a function of c_{STD} was not represented graphically. Herein, they are shown in Figure 30.

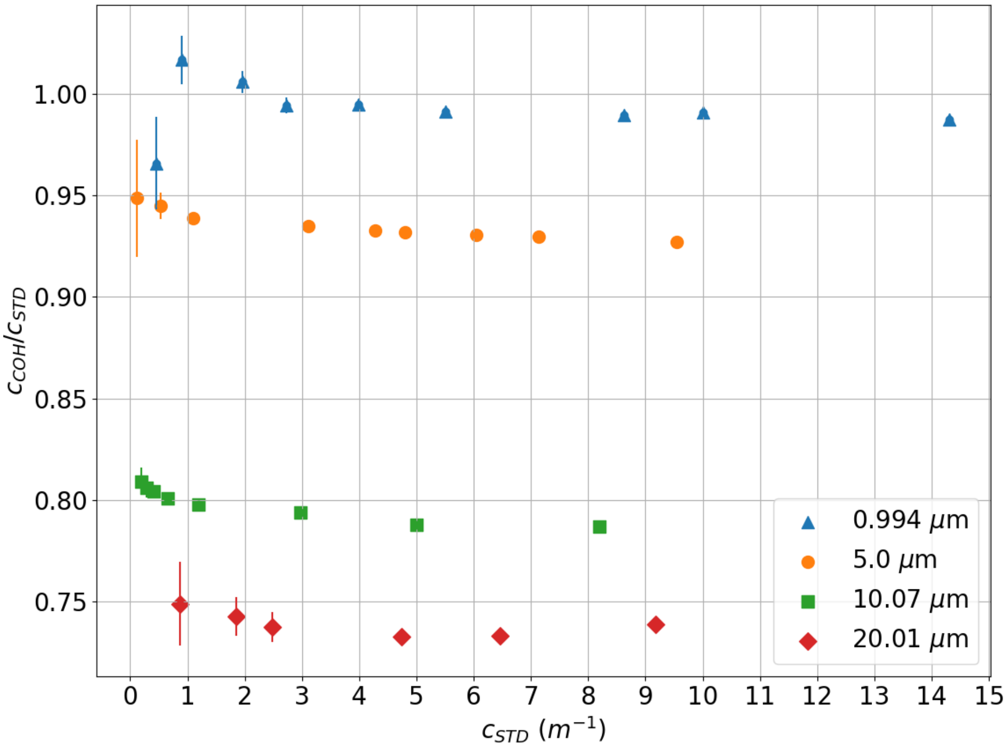

Figure 30: Attenuation measurements made simultaneously by the coherence and standard transmissometers for polystyrene beads of sizes 0.994 µm, 5.0 µm, 10.07 µm, and 20.01 µm.

There are two primary factors to consider in this figure: the linearity of the c_{COH}/c_{STD} measurements at low attenuations, which is understood to be correlated with device sensitivity; and the absolute value of the c_{COH}/c_{STD} measurements, which is a marker of the extent to which the coherence transmissometer better excludes forward scattered light. As discussed in the previous chapter, as a result of improvements in design and experimental protocols, the linearity of the c_{COH}/c_{STD} measurements for all particle sizes has extended to smaller c_{STD} values, with a stable linear relationship between c_{COH} and c_{STD} for $c_{STD} > 2m^{-1}$ for all microsphere sizes.

However, the second key takeaway from Figure 30 can be found by considering the absolute values of the c_{COH}/c_{STD} measurements for each microsphere size. In the following discussion, the averages of the c_{COH}/c_{STD} measurements for each particle size have been taken for $c_{STD} > 2\ m^{-1}$, where the relationship between both transmissometers is linear.

In the optimized transmissometer measurements, despite a large improvement in the measurement sensitivity and precision as discussed in the previous chapter, the coherence transmissometer consistently measures attenuation values lower than that of the standard transmissometer. For the 0.994 ± 0.01 µm, 5.0 ± 0.3 µm, 10.07 ± 0.06 µm, and 20.01 ± 0.33 µm microspheres, the average c_{COH}/c_{STD} measurements are $0.99 \pm 4.2E^{-4}$, $0.93 \pm 4.2E^{-4}$, $0.79 \pm 1.1E^{-3}$, and $0.74 \pm 6.5E^{-4}$, respectively. This is the opposite behaviour to what was hypothesized to occur for the coherence transmissometer, which was designed on the principle that only transmitted light would remain spatially coherent and only spatially coherent light would diffract to orders > 0 and reach the detection area. These optimized results also show the opposite behaviour to that shown in Chapter 3: Initial transmissometer performance using a diffraction grating for the liquid antacid and Thalassiosira sp. Measurements. It is surprising that the optimized transmissometry behaviour appears to be fundamentally different from both prediction and previously observed results for samples of a similar size scale.

The increasingly low values of c_{COH}/c_{STD} measured as a function of particle size suggest the presence of a variable effect with particle size rather than the introduction of a new fixed systematic bias or noise term to the set-up. There have been no fundamental changes to the design of the standard transmissometer throughout this optimization process, suggesting that the coherence transmissometer is recording relatively lower attenuation values than was previously the case.

Going back over the optimization process described in this chapter, most changes have focused on locking down the position of optical components, changing the experimental procedure, or changing the data analysis procedure. There have not been many physical changes to the experimental set-up. In fact, the only extra component that has been introduced is the focusing lens between the diffraction grating and the photodetector for the coherence transmissometer. This suggests that the lens has an important role in the change in the nature of the c_{COH}/c_{STD} measurements.

However, if it is possible to create a change in the system that decreases the attenuation recorded by the coherence transmissometer, without changing the nature of the attenuating samples, this sheds some doubt on the original hypothesis that only transmitted light passes the diffraction grating since the proportion of transmitted light to the total initial signal should only be controlled by the nature of the samples. This highlights a pressing need to re-examine the original hypothesis regarding spatial coherence and transmitted and scattered light in the Mie scattering regime.

A potential interpretation of these results is that some amount of light remains spatially coherent after scattering from the sample and is able to be collected by the coherence transmissometer. If all scattered light is incoherent, then there would be no possibility of it contributing to the non-zero diffraction orders, and placing a lens between the diffraction grating and detector would simply improve the collection of the diffracted order. On the other hand, if some amount of spatially coherent light were to be retained on scattering, this could contribute to the non-zero order diffraction signals, providing an angularly dependent signal, and the focusing lens would then be focusing scattered light onto the detector, resulting in lower attenuation values, effectively reintroducing a non-zero collection angle. At this point, the addition of a focusing lens would alter the amount of scattered light collected. As discussed by Boss et al. (2009), transmissometers with different collection angles can measure very different attenuations for similar particle types, sizes, and concentrations.

To determine the likelihood of the above scenario and assess the success of the coherence transmissometer in excluding scattered light, the possibility of spatial coherence being retained on scattering must be investigated further. This will involve both a review of any existing literature on spatial coherence retention after scattering and an experimental test of this concept.

5.1. Coherent scattering in marine and atmospheric environments

The most common approach to describing the behaviour of light in marine environments corresponds to a ballistic photon approach, wherein a light particle is considered to collide with a marine particle, after which a new direction for the light particle to travel in is randomly chosen, as described in Figure 31 from Mishchenko (2009). This ballistic approach is the underlying principle from which radiative transfer theory has been derived (Bohren & Clothiaux, 2006). This approach does not account for the possibility of light interference resulting in coherence-based effects.

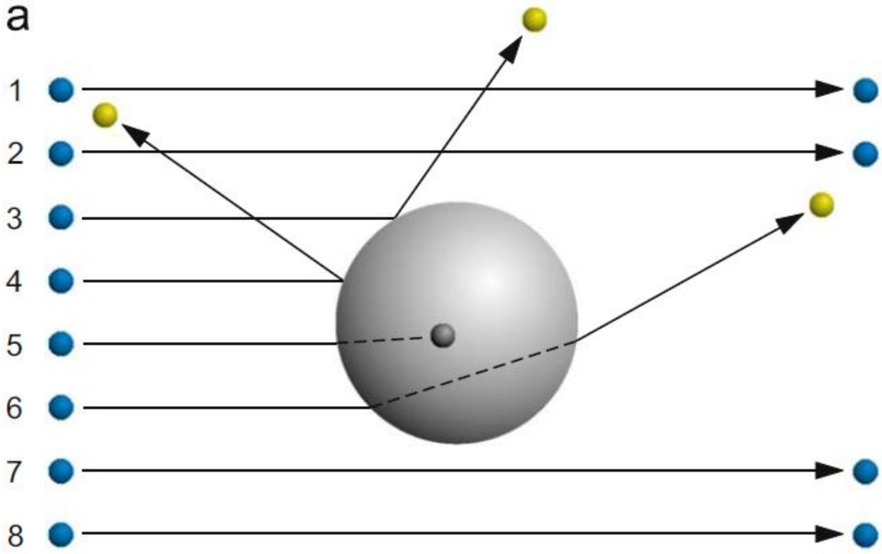

Figure 31: Depiction of a ballistic photon view of light scattering, where light particles interact with scattering particles resulting in a change in their initial direction. Figure taken from Figure 1a of Mishchenko, 2009 (Mishchenko, 2009).

However, studies from the field of atmospheric sciences contradict this view. Mishchenko refutes this approach and instead describes an electromagnetic field approach for an infinite plane wave wherein the total field at all locations is modified by the presence of a particle at all times, and is not only changed “after collision with a particle” (Mishchenko, 2009). Rather than describing a causal relationship between a particle and some scattered field, he instead describes a probabilistic relationship where the total field is at all times modified by the existence of the particle and its potential to cause scattering.

For the most part, the above-described approach merely alters the frame-of-thinking associated with scattering, since the full radiative transfer equations and the Mie scattering approach can be derived from this electromagnetic field description (Mishchenko, 2002;

Mishchenko, 2008). However, this view results in the prediction of coherent scattering effects where the intensity of the field increases at certain locations due to constructive interference. For example, coherent backscattering results in the creation of an intensity peak at exactly 180° for an ensemble of particles when the field is statistically averaged over all possible particle positions. This behaviour can be seen in both experimental data and numerical simulations of Maxwell’s equations. The act of averaging over all possible particle configurations for a set of fixed particles is considered to be analogous to time-averaging a light signal that has passed through an ensemble of particles in constant movement, as is the case for taking time-averaged transmissometry data from marine samples held in a cuvette. Therefore, coherent effects seem likely to also appear in marine optics applications.

Via numerical studies, Mishchenko predicts that there should also be a strong forward-scattering enhancement at 0° due to coherent effects, alongside the coherence backscattering enhancement at 180°, for randomly-distributed particles with sizes on the order of the light wavelength at concentrations from 0.1% to 24% (Mishchenko et al., 2007). For two different refractive indices, a strong forward-scattering signal was seen at the exact angle of forward scattering (0°) that increased with the concentration of particles and was attributed to constructive interference. The authors note that this is because the phase of the scattered wavelet from each particle is exactly the same regardless of particle position for this specific direction. If multiple scattering was not present, the forward-scattered phase function would continue to increase as a function of the number of scatterers indefinitely. However, multiple scattering causes this phenomenon to plateau. This effect was also noted in a previous study (Mishchenko, 2008), which described that certain scattering wavelets in certain directions will always have the same phase difference and always interfere constructively regardless of the particle positions.

Although Mishchenko has theoretically and numerically described both coherent backscattering and forward-scattering effects, when it comes to experimental observations the backscattering effect has been more extensively studied. For example, Van Der Mark et al. (1988) studied the scattering behaviour of polystyrene beads in water with sizes from 0.215 microns to 2.02 microns. An enhancement of the scattering behaviour in the backscattering direction was observed that was concluded to come from constructive interference. The forward-scattering enhancement was not reported on, despite the presence of a detector at this position. Similarly, Wolf & Maret (1985) demonstrated a coherent backscattering enhancement in samples of polystyrene spheres in water with submicron diameters from 0.109 to 0.8 μm at samples concentrations as high as 10% with a collection angle of 0.17°. They report an increase in the intensity and angular width of this effect increased with the density of scatterers, alongside some polarization dependence of the effect.

It should also be noted that the majority of studies have been performed on submicron-sized particles; the presence of coherent scattering interference at the particle sizes used in this thesis (approximately 1 – 50 µm) has not been widely explored, to our knowledge.

However, within the marine optics field, Fry et al. (1992) measured coherent scattering effects in the near-forward direction by designing a set-up that allowed separation of the transmitted beam from the scattered beam at 0°. The set-up utilized a photorefractive crystal in which beam fanning (otherwise known as asymmetric self-defocusing) occurred which allowed undeviated transmission of a beam that exhibits spatial phase perturbations associated with scattering.

They found that spherical particles do not need to be identical to create identical phase shifts on scattering which will lead to constructive interference in the forward direction. At 0°, although the amplitude of scattering strongly depends on the sphere radius, the phase shift associated with scattering does not. When variations in the scattered phase are small with changes in sphere radius, even an arbitrary particle size distribution can result in coherent scattering effects at 0°. Fry et al. (1992) showed that scattered phase variations are small and coherent scattering is possible at sphere radii greater than a few micrometers (Figure 2). However, the extent to which any resulting constructive interference would enhance the forward signal for a given particle size and type was not specified in this study. Furthermore, coherent effects at non-zero angles were not described. In the coherence transmissometer design described in this thesis, coherent scattering effects would need to be occurring at non-zero angles for a change in the collection angle to affect the measured attenuation.

In conclusion, multiple studies, covering theoretical, numerical, and experimental techniques, have acknowledged the presence of enhanced signals at certain scattering angles due to the effects of constructive interference of the scattered wave with itself. This is an effect that only shows up as a result of scattering from multiple particles. Although constructive interference effects have been more extensively studied in the backscattering direction for sub-micron sized particles, there has been some indication that a forward-scattering enhancement at the particle sizes used in this thesis could be expected (Fry et al., 1992).

Therefore, it is possible that some amount of forward-scattered light in the coherence transmissometry system is spatially coherent with itself and is able to diffract into diffraction modes greater than 0, making it inseparable from the transmitted light. While the phase of the light may have been shifted from that of the initial beam, spatial coherence can still be created due to the same shift occurring for multiple particles. This could be a viable explanation for the results in Figure 30, where $c_{\mathrm{COH}} < c_{\mathrm{STD}}$ after changes to the set-up that would have altered the collection angle of the coherence transmissometer. Considering these results in the context of the possibility of coherent forward scattering, it is necessary to investigate the likelihood of this effect further before making more attenuation measurements for a wider range of polystyrene microspheres.

5.2. Coherent scattering observations in coherence transmissometer

5.2.1. Collection of scattered light at the coherence transmissometer

The hypothesized improvement provided by the coherence transmissometer to standard scattering errors was due to the proposed removal of incoherently scattered light from the measurement area. This concept is reliant on two assumptions: that the diffraction grating acts as a filter for spatial coherence; and that all scattered light becomes 100% spatially incoherent.

The first assumption holds based on the understanding that diffraction gratings act as the Young's double slit experiment for many slits, as discussed in section 2.2.2.1. Interference and Young's Double Slit experiment.

The second assumption requires further investigation based on the results seen in *Figure 30*, where the addition of a focusing lens (f = 25 mm) in front of the coherence transmissometer detector appeared to decrease the attenuation measured at the coherence transmissometer relative to the standard transmissometer. Assuming that all light diffracted onto the lens from the grating must be spatially coherent, this observation suggests that either some amount of spatial coherence may be preserved on scattering, or a substantial proportion of stray light from an alternate source is being focused by the lens onto the detector.

Initial attempts were made to reduce the likelihood of stray light entering the lens from other sources on the optical table by adding additional beam blocks around light sources such as the optical fibre. Measurements of $c_{\mathrm{COH}}/c_{\mathrm{STD}}$ were made for 10.07 ± 0.06 μm polystyrene beads prior to and after adding the additional beam blocking. However, no substantial difference in $c_{\mathrm{COH}}/c_{\mathrm{STD}}$ measurements were observed, with the behaviour still following the trend seen in *Figure 30*. Stray light could be scattered in all directions from the diffraction grating; however, the focusing lens was placed at a distance > 2*f* away from the grating, indicating that diffusely scattered light should not be captured and focused down onto the detector at *f* distance away from the lens.

A potential interpretation is that the increased light signal at the coherence transmissometer detector (compared to the case without a lens prior to the detector) is due to the capture of coherent light that has been diffracted from the grating, captured by the lens, and focused onto the detector. Although these results could also be potentially be explained by large beam divergence from the diffraction grating, the use of a collimated laser source with an experimentally measured divergence of $\Theta = 7.69E^{-4}$ mrad ($4.41E^{-5\circ}$) makes this explanation unlikely. The increase in signal from the case with no lens to the case with the lens in place suggests instead that a non-negligible proportion of this light has been scattered at angles > 0°. However, as discussed previously, non-zero angle coherent scattering has not been discussed within marine optics and should be discussed here with caution.

To test the new hypothesis that coherently scattered light was being captured by the lens, an adjustable aperture was added just prior to the lens (Figure 32:). If all of the incident light on this lens was coherently transmitted, only light overlapping with the Gaussian beam should be focused down via the lens onto the photodetector. In this case, there should be no change in the voltage measured by the coherence photodetector with changing aperture size, as long as the aperture size remains greater than the transmitted beam width. This scenario aligns with the original hypothesis of approximately 100% spatial incoherence of all scattered light. However, if some amount of coherently scattered light passes the diffraction grating at angles collected by the lens, the signal measured at the detector should change with changing aperture size. Here, the lens has a maximum numerical aperture of 0.29 when the aperture is fully open, which decreases to 0.10 as the aperture in front of the lens is closed. This scenario aligns with the alternate hypothesis of some non-zero percentage of coherent scattering occurring.

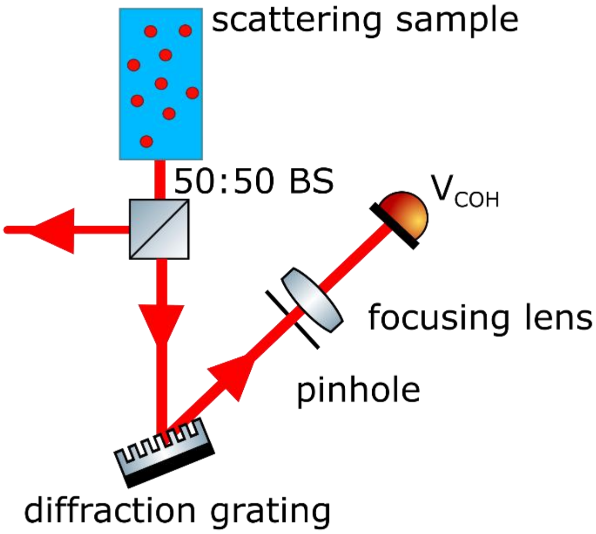

Figure 32: Zoomed-in view of the coherence transmissometer arm of the experiment. An adjustable pinhole has been placed directly in front of the f = 25 mm lens. The pinhole size started fully open (15 mm diameter) and was closed towards the size of the beam (approximately 5 mm diameter) The rest of the experiment (not pictured) remains the same as in Figure 29.

With the adjustable aperture in front of the lens in the coherence transmissometer fully open (Ø ≈ 15 mm), the system was set to start acquiring voltage data as normal as a function of time, with a sample of 10.07 ± 0.06 μm polystyrene beads with $c_{\mathrm{STD}} \approx 4.23 \pm 0.10\ \mathrm{m}^{-1}$ held in the cuvette. As the data acquisition progressed, the aperture was slowly, manually closed, approaching a previously marked point that was slightly larger than the beam width of the transmitted beam (Ø ≈ 5 mm). Once this point was reached, the aperture was not closed further and the data acquisition period progressed at this aperture size until finished. Data was taken for 50 s with a sampling period of 0.05 ms. Prior to the sample acquisition, voltage signals were acquired for the same time period and sampling period for five individual sets of Milli-Q reference samples. Each Milli-Q reference sample corresponds to a fresh introduction of new Milli-Q into the cuvette. The average of these five Milli-Q references was then used to calculate the attenuations at both transmissometers for the 10.07 ± 0.06 μm polystyrene bead sample.

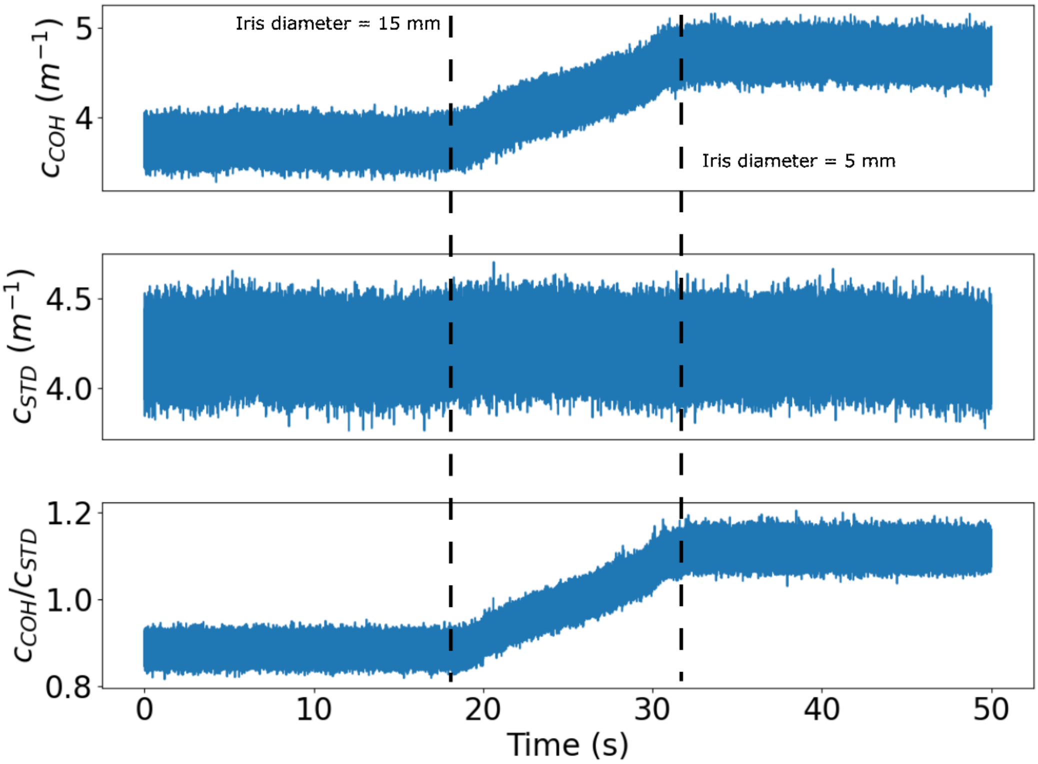

Figure 33:Attenuations measured at the coherence and standard transmissometers as a function of time, when an adjustable iris in front of the coherence transmissometer lens is closed from a 15 mm diameter to a 5 mm diameter (just larger than the beam size). a. Attenuation measured at the coherence transmissometer (c_{COH}). b. Attenuation measured at the standard transmissometer (c_{STD}). c. Ratio between the attenuations measured at the coherence and standard transmissometers (c_{COH}/c_{STD}).

As can be seen in Figure 33, when the iris is fully open such that the coherence transmissometer is capturing the maximum amount of light, c_{COH} measures approximately 0.88 c_{STD} (± 0.02) at $c_{COH} = 3.72 \pm 0.10$ m^{-1}. During the course of the experiment, the adjustable pinhole was manually closed towards the beam size of the transmitted beam. The change in all transmissometers during this closure is indicated by the area enclosed by the dashed lines in the above figure. With the iris fully closed to just wider than the transmitted beam width, c_{COH} measures approximately 1.11 c_{STD} (± 0.02) at $c_{COH} = 4.69 \pm 0.10$ m^{-1}. The value for c_{STD} remains comparatively stable throughout the measurement with an average value of 4.23 ± 0.10 m^{-1}. The standard deviation of both signals may be slightly higher than during a typical data acquisition procedure because some of the background light shielding was reduced to allow the user access to the adjustable aperture during the course of the measurement. However, the clear takeaway is that, while c_{STD} remains fairly stable through the measurement, c_{COH} is substantially affected by the change in aperture size, indicating that an amount of scattered light large enough to substantially change the transmissometer performance is passing through the coherence filter provided by the diffraction grating. This potentially suggests that, rather than scattered light from the polystyrene beads being 100% spatially incoherent, some non-negligible amount of spatial coherence is retained on scattering.

The presence of some non-negligible but unknown proportion of coherently forward-scattered light in the coherence transmissometer would explain the difference between the results seen in Chapter 3: Initial transmissometer performance using a diffraction grating and those seen in *Figure 30*. Adding the lens to focus light onto the detector changes the collection angle of the coherence transmissometer, allowing it to capture more scattered light and measure a higher transmitted signal than in the case without a lens. The severity of this effect scales with increasing particle size, as the VSF for increasing sizes of polystyrene microspheres becomes stronger at small angles, as discussed previously. This is seen in Figure 30 where, after the addition of a focusing lens, $c_{\mathrm{COH}}/c_{\mathrm{STD}}$ becomes increasingly lower than one with increasing particle size. This scaling of the effect severity with particle size suggests that we can exclude potential interpretations that do not scale with particle size, such as fixed optical noise in the optical set-up or effects of beam divergence from the grating.

5.3. Collection angle of the coherence transmissometer

Previously, when the coherence transmissometer was hypothesized to reject all scattered light, the coherence transmissometer was effectively assumed to have a collection angle of zero for scattered light, measuring only transmitted light.

However, in the presence of coherently forward-scattered light, the coherence transmissometer must have some non-zero collection angle for scattered light. Whereas in previous iterations of the transmissometry set-up, only the collection angle of the standard lens-and-pinhole transmissometer had to be calculated, now the collection angle of both transmissometers must be evaluated. More so, to exactly compare the effect of the coherence filter on the attenuation measurements, the collection angles of both transmissometers must be matched.

Several factors go into determining the collection angle of the coherence transmissometer:

1. The total path length between the exit face of the cuvette and the photodetector. Due to design constraints in the system when making simultaneous attenuation measurements, this distance has previously been longer for the coherence transmissometer than for the standard transmissometer;

2. The presence (or absence) of a lens and pinhole arrangement and its properties (i.e., focal length of lens, size of pinhole, and distance between optics);
3. The wavelength-dependent angular spread of the diffracted light from the grating;
4. The spread of the angular scattering distribution of the light when diffracted to the –1st diffractive order;
5. The increased spread of any initial beam divergence of the incident beam after diffraction from the grating;
6. Compression of the angular distribution of the diffracted light due to the compressed effective grating area experienced when the light hits the grating at an angle other than normal.

All of the above-listed phenomena have the potential to change the signal recorded by the coherence transmissometer in the presence of coherent scattered light, resulting in a different measured attenuation value. The key factor that we are interested in measuring in isolation is the effect of the diffraction grating as a coherence filter on the attenuation measurements. However, when simply measuring the level of light that reaches the photodetector of the coherence transmissometer, all of the factors affecting the collection angle couple together with the effect of the coherence filter and their separate effects cannot be distinguished.

In order to truly distinguish the absolute performance of the coherence transmissometer with respect to the standard lens-and-pinhole transmissometer in the presence of coherence scattering, all of the above-listed effects on the collection angle must be quantified. In practice, it is not trivial to calculate the results of all of these effects on a light field of arbitrary angular scattering distribution. In particular, the angular spread of light on diffraction from the grating occurs primarily on one axis (x-axis), with no spread occurring on the other (y-axis). Additionally, the diffraction grating is angled along the y–z plane but remains normal to the beam along all others, resulting in a compression of the beam after diffraction only along the x-axis due to the compressed area of the grating experienced by the incoming light. Both of these two effects specifically result in an elliptical collection angle for the coherence transmissometer, i.e., the collection angles in the x-axis and y-axis are not necessarily equal. This makes the exact calculation of the collection angle and subsequent comparison to that of the standard transmissometer, which is radially symmetric, extremely difficult.

As discussed in Chapter 4, the beam divergence over the approximate path length of the full experimental set-up was calculated to be $\Theta = 7.69E^{-4}$ mrad ($4.41E^{-5\circ}$), with a beam waist of 2.5 mm and a Rayleigh range of 100 m for a wavelength of 521.2 nm and $M^2 = 1.5$, which is a relatively low beam divergence due to the use of a collimated laser beam. This indicates that it is unlikely that the inherent spread of the incident beam will contribute to a higher attenuation measurement at the coherence transmissometer.

The exact quantitative calculation and comparison of both collection angles may need a complex ray tracing model that is not the focus of this experimental work. Instead, the focus was to minimize the effect of as many parameters affecting the collection angle as possible. For example, the distances involved in the standard transmissometer could be made longer to ensure that the path length and distance between optics in each transmissometer were the same. A lens-and-pinhole arrangement with the exact same focal length and aperture size as that in the standard transmissometer could be added to the coherence transmissometer to provide additional directional filtering and account for this effect on the collection angle. The wavelength dependent spread of the light from the grating was assumed to be negligible relative to other factors due to the use of a monochromatic laser source ($\lambda = 662.5 \pm 1.0$ nm).

This leaves only the non-radially symmetric effects that the diffraction grating may have on the angular scattering distribution. The inability of the study to account for these is an acknowledged limitation. However, going forward, the collection angles of both transmissometers were considered to be broadly similar due to the equivalence of the path lengths and lens-and-pinhole parameters.

5.3.1. Experimental design changes

The simultaneous transmissometer set-up was updated to remove as many factors as possible that could change the collection angle of the coherence transmissometer with respect to that of the standard transmissometer. A key change that was made was the addition of the same lens-and-pinhole arrangement to each transmissometer. In the updated set-up, both transmissometers now contain a plano-convex lens with a focal length of 50 mm that focuses the incident light down through a 2 mm pinhole that is placed at the focal plane. This means that the coherence transmissometer has been adjusted to now include both a directional filter (the lens and pinhole combination) and a coherence filter (the diffraction grating). On the other hand, the standard transmissometer contains only the directional filter and no coherence filter. Although the idealized final version of the coherence filter would not require this directional filter, adding it in this experiment provides us with a way to directly compare the effect of coherence filtering on the attenuation measurements in two cases of similar collection angle.

Alongside this update, the previously fixed apertures used as pinholes were replaced with adjustable translation stages with apertures mounted inside. This allowed the position of the pinholes to be fully adjustable in the x–y plane, where z is the beam propagation direction. Alignment of the beam through the exact centre of each pinhole using the adjustable screws to move the centre exactly 1 mm from the position at which the beam hit the edge of the aperture was performed with Milli-Q in the cuvette. This alignment procedure was added to the protocol before taking each new dataset for each sample, to ensure that beam wander had not affected the alignment through the pinhole. The signal may not change noticeably for slight movements of the beam with respect to the pinhole centre after passing through a cuvette filled with Milli-Q, due to the relatively flat VSF of Milli-Q in the forward direction. However, for beams scattered from large scatterers, the VSF becomes forward-peaked with a slope wider than the pinhole aperture. Movement of the pinhole centre with respect to the beam then results in a change in the proportion of the scattered signal captured by the photodetector, affecting the final light level and the attenuation measurement. The above-described procedure aimed to eliminate this potential problem.

To remove the potential effect of different path lengths in air through each transmissometer, the experimental set-up was adjusted so that each transmissometer was composed of the same distance from the exit of the cuvette to the lens-and-pinhole arrangement (Figure 34).

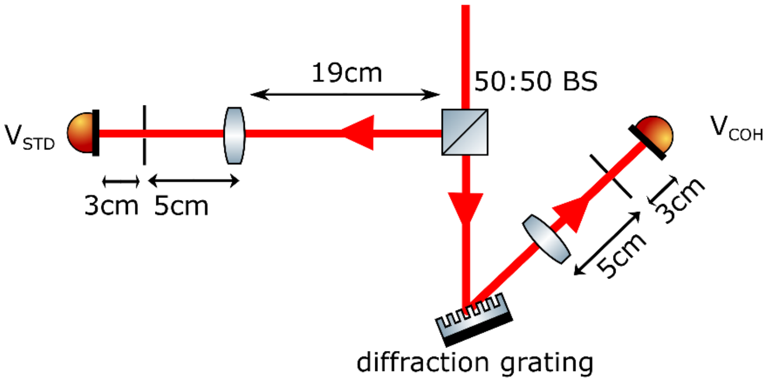

Figure 34: Close-up of final alterations to the standard and coherence transmissometers. Both transmissometers use the same f = 50 mm lens, a 2 mm pinhole, and the same distances between all optics (including from beamsplitter to focusing lens) in order to achieve broadly similar angular collection angles.

This decision was taken to show that different path lengths between the two transmissometers should not contribute to the coherence transmissometer measuring a different attenuation than the standard method. With this approach, coupled with the choice of the same lens-and-pinhole arrangement, the two transmissometers were considered to have broadly similar collection angles — as much as was considered possible without calculating the effect of the diffraction grating on the light field via a ray transfer model.

5.4. Performance of coherence transmissometer: polystyrene beads

With the experimental set-up updated as described in the previous section to obtain a coherence transmissometer with a broadly similar collection angle to that of the standard transmissometer, $c_{\mathrm{COH}}/c_{\mathrm{STD}}$ values were measured for polystyrene microspheres from 0.994 µm to 49.9 µm (Figure 35).

Table 5: Polystyrene microsphere properties

Diameter (µm)	Standard deviation of particle size distribution (µm)	Refractive index	Microsphere composition	ThermoFisher Catalogue Number
0.994 ± 0.01	0.01	1.59 @ 589 nm	Polystyrene	4009A
2.020 ± 0.015	0.021	1.59 @ 589 nm	Polystyrene	4202A
5.0 ± 0.3	0.6	1.59 @ 589 nm	Polystyrene Divinylbenzene	2005A
10.07 ± 0.06	0.09	1.59 @ 589 nm	Polystyrene	4210A
20.01 ± 0.33	0.26	1.59 @ 589 nm	Polystyrene	4220A
49.9 ± 0.6	0.6	1.59 @ 589 nm	Polystyrene	4250A

For each bead size from 0.994 µm to 49.9 µm (Table 5), the following experimental procedure was followed.

The cuvette was flushed out three times with fresh Milli-Q to reduce contamination from previous sample measurements. The outside windows of the cuvette were cleaned with methanol prior to the initiation of each polystyrene microsphere sample run. The polarization incident on the diffraction grating was adjusted to the point of optimal diffraction efficiency towards the coherence transmissometer by rotating the HWP. Each Picoscope channel used to measure voltage was zeroed under darkened experimental conditions. The cuvette was filled with the first fresh Milli-Q sample and the alignment of the laser was confirmed to hit each measurement point while passing through the centre of all optics. The adjustable pinholes at each transmissometer were checked and adjusted such that the visible laser beam passed through the centre of each pinhole. Light signals were measured for five fresh Milli-Q samples. Background light measurements were made after each Milli-Q and polystyrene bead attenuation measurement after closing the shutter at the laser output to remove light in the system. For each polystyrene microsphere size, a high concentration sample was made by diluting polystyrene microsphere suspensions with fresh Milli-Q. Samples of decreasing concentration were made from the original sample by further dilution with fresh Milli-Q.

For each polystyrene bead measurement for microsphere sizes from 0.994 ± 0.01 μm to 20.01 ± 0.33 μm, five waveforms of voltage signals corresponding to N datapoints were saved and then averaged to get a single voltage corresponding to light attenuation through each sample. For the 49.9 ± 0.6 μm, the microspheres rapidly fell out of suspension such that averaging a large number of datapoints was not appropriate. Instead, a large number of waveforms were saved covering a range from c_{STD} = 12.96 ± 0.01 m^{-1} to 0.30 ± 0.01 m^{-1}. Rather than averaging, the attenuation of each datapoint was calculated relative to the median Milli-Q measurement for both transmissometers. The resulting signals were then downsampled to compare on the same plot as the $c_{\mathrm{COH}}/c_{\mathrm{STD}}$ measurements for the other microsphere sizes (Figure 35).

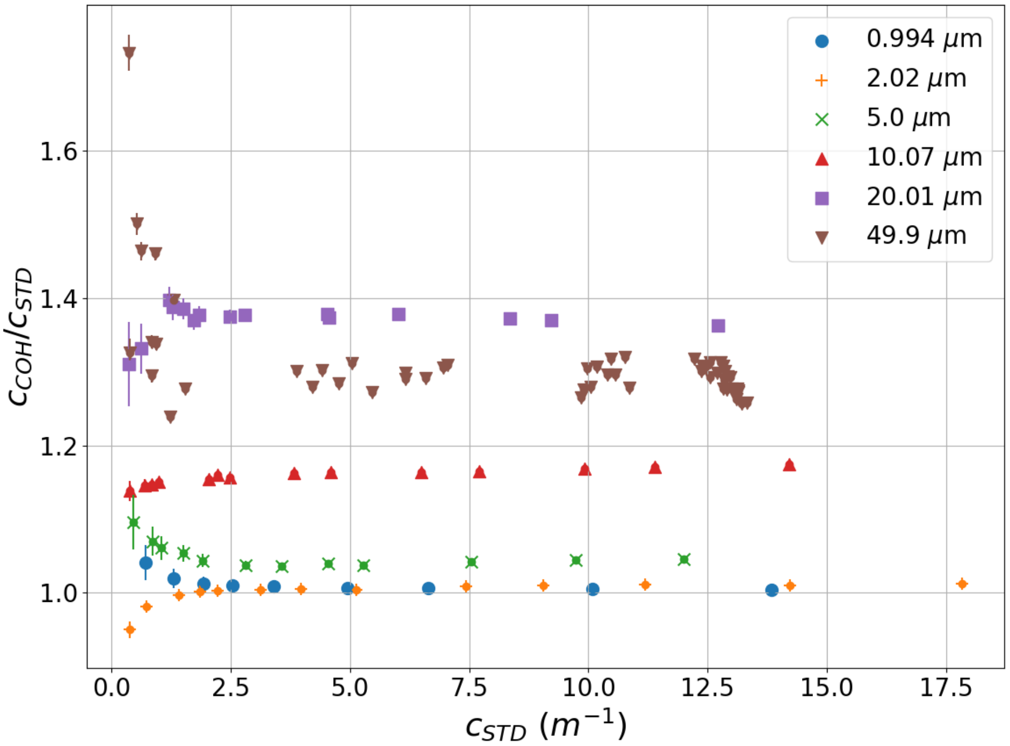

Figure 35: Performance of the coherence transmissometer compared to the standard transmissometer (as shown via $c_{\mathrm{COH}}/c_{\mathrm{STD}}$) when both transmissometers have a broadly similar collection angle for a range of polystyrene microsphere samples with diameters from 0.994 ± 0.01 – 49.9 ± 0.6 μm.

From 0.994 ± 0.01 μm to 20.01 ± 0.33 μm, there is a clear increase in values of $c_{\mathrm{COH}}/c_{\mathrm{STD}}$ with increasing particle size in regimes where a stable, linear relationship between the transmissometers is achieved. There is a reduction in the difference between c_{COH} and c_{STD} for the 49.9 ± 0.6 µm microspheres compared to the 20.01 ± 0.33 µm microspheres; however, the attenuation measured by the coherence transmissometer is still larger than that measured by the standard transmissometer. The $c_{\mathrm{COH}}/c_{\mathrm{STD}}$ measurements were considered to remain stable and linear with decreasing attenuation until values of approximately $c_{\mathrm{STD}} = 2$ m^{-1} for all microsphere sizes. The best linear fit value of $c_{\mathrm{COH}}/c_{\mathrm{STD}}$ was therefore determined for all values corresponding to $c_{\mathrm{STD}} > 2\mathrm{m}^{-1}$ for all microsphere sizes (Figure 36)

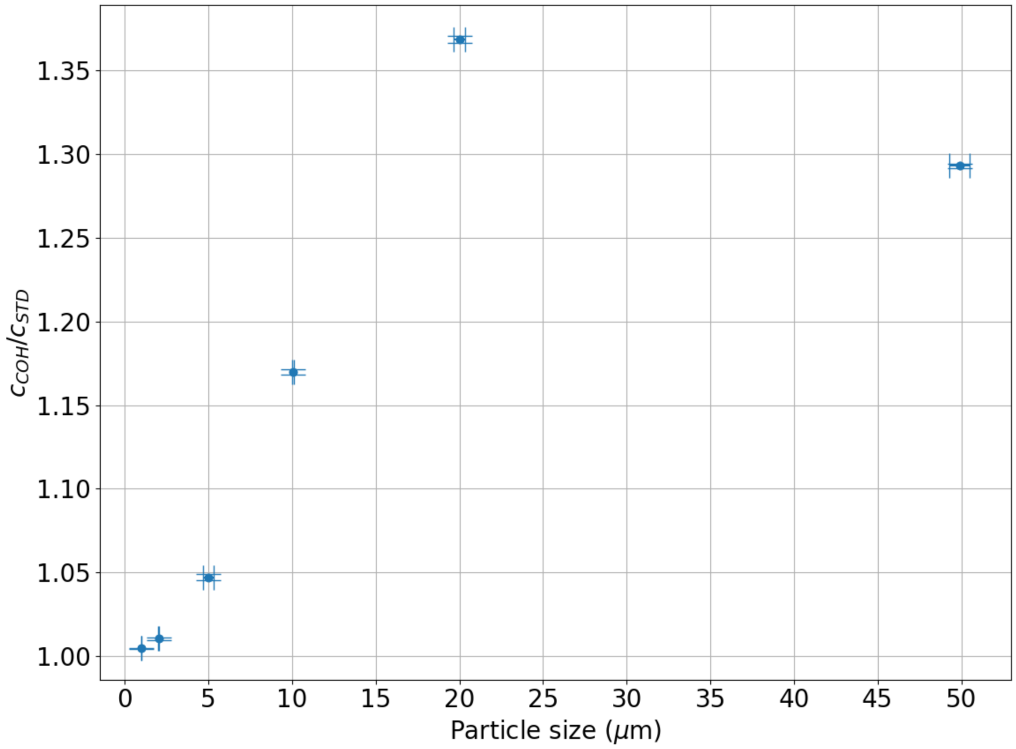

Figure 36:Best linear fit of $c_{\mathrm{COH}}/c_{\mathrm{STD}}$ values measured in the linear regime for all polystyrene microspheres as a function of particle size.

For values of $c_{\mathrm{STD}} > 2$ m^{-1}, the best fit values of $c_{\mathrm{COH}}/c_{\mathrm{STD}}$ were 1.00 ± 3.72E^{-4} for 0.994 ± 0.01 µm, 1.01 ± 7.16E^{-4} for 2.020 ± 0.015 µm, 1.05 ± 1.73E^{-3} for 5.0 ± 0.3 µm, 1.17 ± 1.51E^{-3} for 10.07 ± 0.06 µm, 1.37 ± 2.20E^{-3} for 20.01 ± 0.33 µm, and 1.29 ± 1.21E^{-3} for 49.9 ± 0.6 µm.

At the two lowest values shown in Figure 36, corresponding to the lowest microsphere sizes of 0.994 ± 0.01 µm and 2.020 ± 0.015 µm, there is not a distinct statistical increase in $c_{\mathrm{COH}}/c_{\mathrm{STD}}$. However, when increasing to larger microsphere diameters, an obvious increase in $c_{\mathrm{COH}}/c_{\mathrm{STD}}$ can be seen with increasing size. The $c_{\mathrm{COH}}/c_{\mathrm{STD}}$ value for 49.9 ± 0.6 µm does not follow this increasing trend, but still shows a substantial deviation of $c_{\mathrm{COH}}/c_{\mathrm{STD}}$ from unity (representing equivalent attenuation measurements).

5.4.1. Comparisons to simulated true attenuation

A theoretical estimate of the level of scattering bias recorded by the standard transmissometer implemented in this experimental set-up was required to evaluate the recorded coherence transmissometer performance ($c_{\mathrm{COH}}/c_{\mathrm{STD}}$) against. This estimate for each dataset was used to give a broad indication of if the increased attenuation measured by the coherence transmissometer was on a reasonable level compared to the expected scattering bias (i.e., if $c_{\mathrm{COH}}/c_{\mathrm{STD}}$ was substantially greater than the expected scattering bias, this would suggest that the difference between the transmissometer measurements was dominated by a systematic offset) and if so, to what degree the coherence transmissometer approach was able to account for the scattering bias.

To produce these expected scattering bias estimations, hereafter expressed as $c_{\mathrm{TRUE}}/c_{\mathrm{STD}}$, a Mie scattering approach following the method of Bohren and Huffman (Bohren & Huffman, 1983) using the publicly available implementation by Slade (W. Slade, 2005) was adapted to our experimental parameters. The following subsection will describe the underlying physics of this approach.

5.4.1.1. Mie scattering implementation

A basic overview of the approach of Mie theory for approximating scattering functions was given in Section 2.1.2.2., where it was discussed that Mie theory simulations must take in the incident wavelength, the particle size parameter, the relative refractive index of the particle, and the angular range of interest to output the elements of the amplitude scattering matrix $S_i(\vec{\theta})$, efficiencies Q_i describing the rate of extinction, total scattering, and backscattering, for example, and the average cosine of the scattering angle, g. The exact details of these calculations for the implementation used in this thesis will be described in more detail here. The theory in this section partially follows that described by MacCallum (2000).

To calculate the angular scattering distribution from each particle, knowledge of certain particle and light characteristics is necessary. For example, the wavelength of the light, the refractive index of the medium, the refractive index of the particle, and the diameter of the particle must be known. The relative refractive index of the particle is taken as an input to the Mie scattering calculations and is calculated as:

$$m = \frac{n_{particle} + in_{particle}'}{n_{medium} + in_{medium}'}, \tag{24}$$

where $n = c/v_s$, c is the speed of light in a vacuum, v_s is the speed of light in a given medium, $n' = a_s\lambda/4\pi$, and a_s is the absorption coefficient. In a theoretical case of zero absorption, as described here, the above equation simplifies to $m = n_{\text{particle}}/n_{\text{medium}}$. Another key input parameter to the Mie scattering calculations is the size parameter of the particle, describing the size of the particle relative to the wavelength of the light, which is given by:

$$x = \frac{2\pi r_{\text{sphere}}}{\lambda}, \tag{25}$$

where r_{sphere} is the sphere radius and λ is the wavelength of the light in the medium.

The samples used in this experimental work were simulated by using a log-normal particle size distribution, as follows:

$$PSD(\xi) = \frac{A}{\sqrt{2\pi}\xi\ln(\sigma)}\exp\left(-\frac{\left(\ln(\xi) - \ln(\xi_{peak})\right)^2}{2\ln(\sigma)^2}\right), \tag{26}$$

where ξ is the range of particle sizes, ξ_{peak} is the central particle size, σ is the standard deviation of the particle size distribution, and A is a scaling factor that determines the height of the particle size distribution.

For the different samples, the particle size distribution was altered by choosing ξ_{peak} and σ such that the PSD was centred at the manufacturer's specification and covered the range given by the manufacturer's tolerance for both the polystyrene microspheres and the phytoplankton species.

The relative refractive index, the size parameter, and the angle range of interest $\vec{\theta}$ (taken as between 0° and 180°) are taken as the inputs to the Mie scattering implementation, which then outputs the scattering wave amplitude functions $S_1(\vec{\theta})$ and $S_2(\vec{\theta})$, the extinction efficiency Q_c, the total scattering efficiency Q_b, and the backscattering efficiency Q_{bb}.

The total scattered intensity of the ensemble of scatterers could then be calculated from the scattering wave amplitude functions, as follows:

$$I_{TOT}(\theta) = \left|S_1(\vec{\theta})\right|^2 + \left|S_2(\vec{\theta})\right|^2 . \tag{27}$$

The total scattered intensity, I_{TOT}, was then summed in combination with the previously defined log-normal particle size distribution over the range of particle sizes defined by ξ_{peak} and σ to obtain the volume scattering function of the entire ensemble of scatterers at a given angle, as follows:

$$\beta(\theta) = \sum_{\xi}\frac{\pi I_{TOT}(\theta)}{\lambda}PSD(\xi)\Delta\xi. \tag{28}$$

This VSF describes the angular distribution of the scattering function due to scattering from all sizes of polystyrene microspheres described within the manufacturer's tolerance (or the analogous case for the phytoplankton species in the given size range). To determine the magnitude of scattering due to this VSF over all angles (0°–180°), the scattering coefficient was calculated as:

$$b = 2\pi \sum_{\theta} \beta(\theta) \sin\theta \, \Delta\theta \, . \tag{29}$$

To calculate the bias in the attenuation measurement at the standard transmissometer due to the finite, non-zero collection angle (taken as 0.9°), the scattering coefficient and VSF are summed from 0° to the collection angle:

$$attenuation\ error = 2\pi \sum_{\theta=0^\circ}^{0.9^\circ} \beta(\theta) \sin\theta \, \Delta\theta. \tag{30}$$

From this, the expected ratio between the "true", unbiased attenuation and that measured by the standard transmissometer is calculated as:

$$\frac{c_{TRUE}}{c_{STD}} = \frac{b}{b - attenuation\ error}, \tag{31}$$

in the absence of absorption in the system such that $c = b$.

Following this method, predicted values of $c_{\mathrm{TRUE}}/c_{\mathrm{STD}}$ were obtained for each sample for both the polystyrene microspheres and the phytoplankton species. To provide error bars for these estimates and evaluate the sensitivity of this model, the peak and width of the particle size distribution were varied (ξ_{peak} and σ, respectively), alongside the relative refractive index, m. The peak size and widths of the particle size distributions for the polystyrene microspheres were determined from the manufacturer specifications (Thermo Scientific Duke Standards 4000 Series Microsphere Size Standards and Thermo Scientific Duke Standards 2000 Series Uniform Polymer Microspheres). The range for modelling was determined by the tolerances given for the peak size and widths of the particle size distributions. The refractive indices of the polystyrene microspheres were given by the manufacturer without tolerances. The range used for modelling was then chosen to be comparable to the percentage range of the particle size distributions.

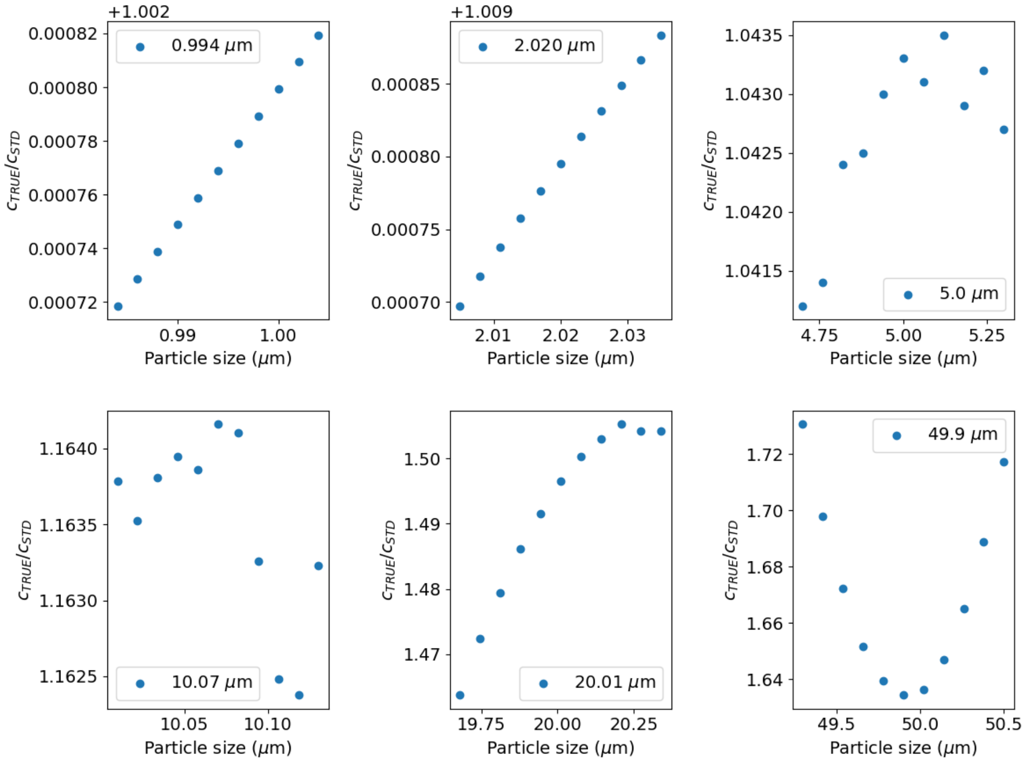

Figure 37: Sensitivity of Mie scattering simulations of $c_{\text{TRUE}}/c_{\text{STD}}$ to changes in particle size for all six polystyrene microsphere sizes.

For all six polystyrene microsphere sizes measured experimentally, the particle size used in the Mie scattering simulations were varied over 11 values and the effect on $c_{\text{TRUE}}/c_{\text{STD}}$ was recorded (Figure 37). The range of particle sizes used were chosen as the uncertainty given in each particle size by the manufacturer, as shown in the first column of Table 5. While results for the 0.994 and 2.020 μm microspheres showed extremely low sensitivity to changes in particle sizes, changes to $c_{\text{TRUE}}/c_{\text{STD}}$ predictions for the 20.01 and 49.9 μm microspheres were more substantial at approximately 1.3% and 2.4%, respectively, over each particle size range. Overall, the $c_{\text{TRUE}}/c_{\text{STD}}$ predictions were increasingly sensitive to changes in particle size as the polystyrene microsphere size increased.

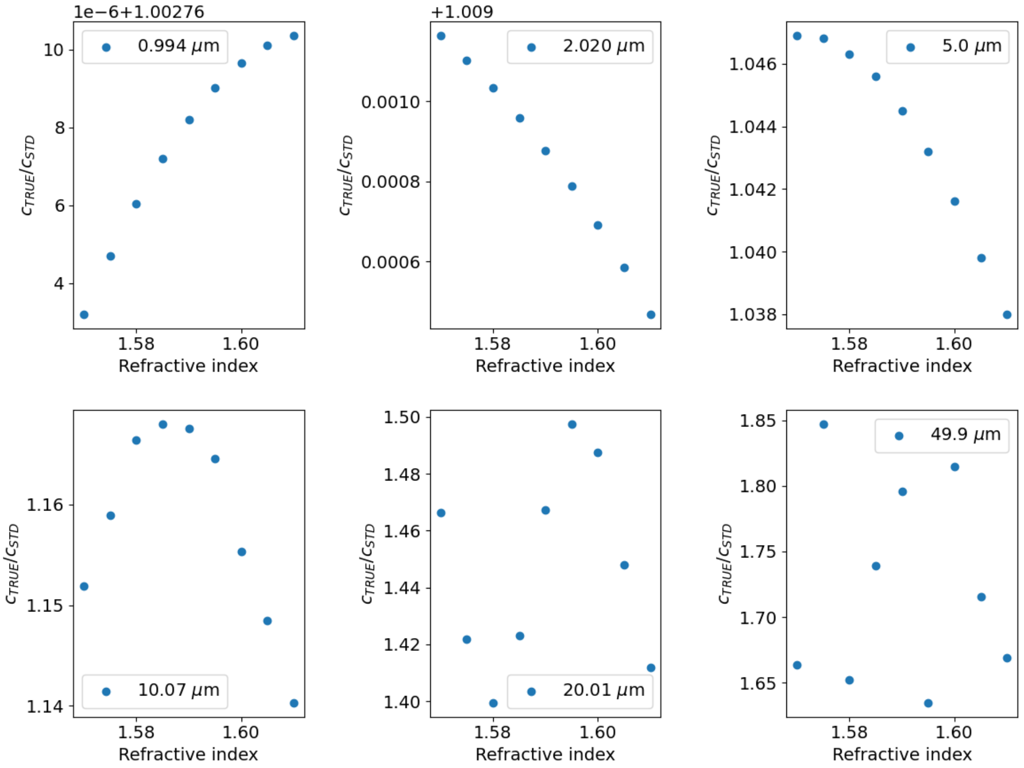

Figure 38: Sensitivity of Mie scattering simulations of $c_{\mathrm{TRUE}}/c_{\mathrm{STD}}$ *to changes in the refractive index of the polystyrene microspheres for all six sizes.*

For all six polystyrene microsphere sizes, the sensitivity of the $c_{\mathrm{TRUE}}/c_{\mathrm{STD}}$ predictions were also determined for changes in the refractive index of the microspheres (Figure 38). The microsphere refractive index was varied across nine values from 1.57 – 1.61. Similar to the previous sensitivity results for changing particle size, the $c_{\mathrm{TRUE}}/c_{\mathrm{STD}}$ predictions were most sensitive to changes in refractive index for the largest particle sizes. For example, for the 49.9 µm microspheres, changes in the refractive index led to 11.4% variation in the $c_{\mathrm{TRUE}}/c_{\mathrm{STD}}$ results. This indicates that the Mie scattering simulations are more sensitive to changes in the refractive index of the scatterers than to changes in the particle size.

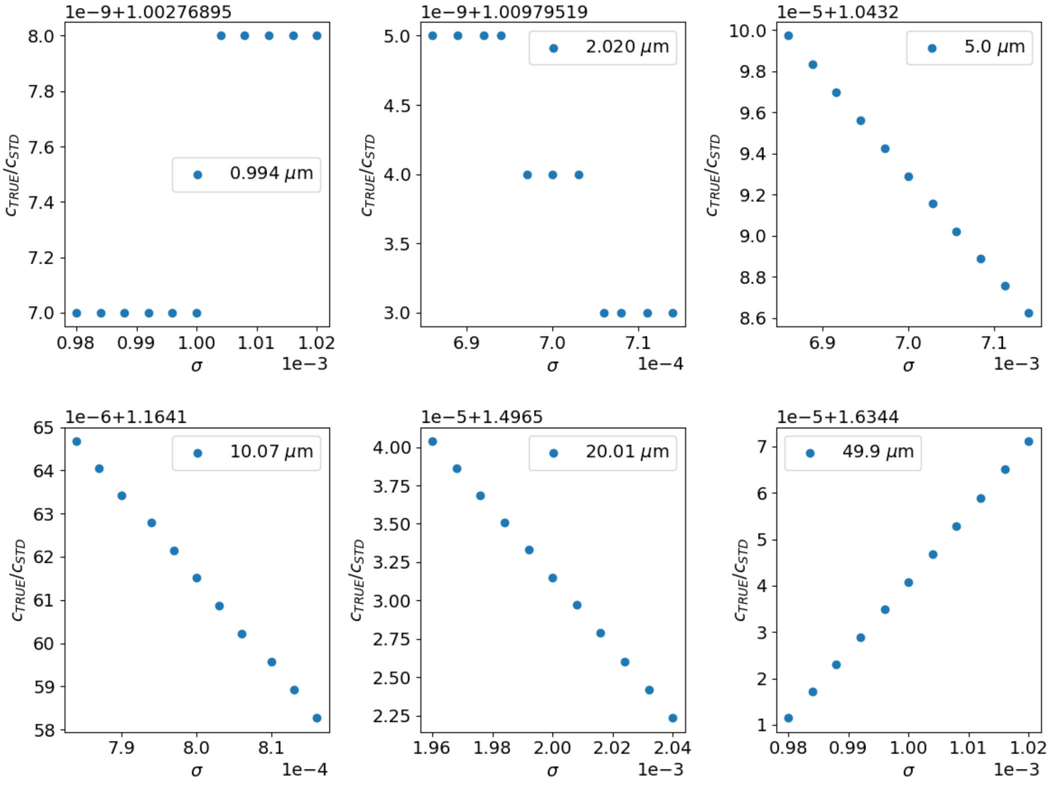

Figure 39: Sensitivity of Mie scattering simulations of $c_{\mathrm{TRUE}}/c_{\mathrm{STD}}$ to changes in the width of the particle size distribution (via the sigma parameter) for all six polystyrene microsphere sizes.

Finally, the sensitivity of the $c_{\mathrm{TRUE}}/c_{\mathrm{STD}}$ predictions to changes in the width of the particle size distribution was evaluated by changing the sigma parameter (as a proxy for particle size distribution width). The sigma values were chosen for each particle size such that the width of the particle size distribution was similar to the standard deviation quoted by the manufacturer. For these sigma ranges, there is not a large change in the $c_{\mathrm{TRUE}}/c_{\mathrm{STD}}$ estimates for all particle sizes (Figure 39).

The above simulations of $c_{\mathrm{TRUE}}/c_{\mathrm{STD}}$ for a range of particle sizes, refractive indices, and particle size distribution widths can be used to provide a confidence range for simulated values of $c_{\mathrm{TRUE}}/c_{\mathrm{STD}}$. As seen above, the simulations are most sensitive to changes in the refractive index of the microspheres and least sensitive to changes in the width of the particle size distribution. This is likely because the widths of the particle size distributions are initially so narrow that changes on the order of a few percent make little difference to the results of the simulation. For changes to the particle size and refractive index, simulations of $c_{\mathrm{TRUE}}/c_{\mathrm{STD}}$ are more sensitive for larger particle sizes.

The standard deviations of the range of $c_{\mathrm{TRUE}}/c_{\mathrm{STD}}$ predictions for changing particle size, refractive index, and sigma were combined in quadrature to give an estimate of the error in the $c_{\mathrm{TRUE}}/c_{\mathrm{STD}}$ simulations. The values of these simulations were then compared against the experimentally measured $c_{\mathrm{COH}}/c_{\mathrm{STD}}$ values for each polystyrene microsphere size (Figure 40).

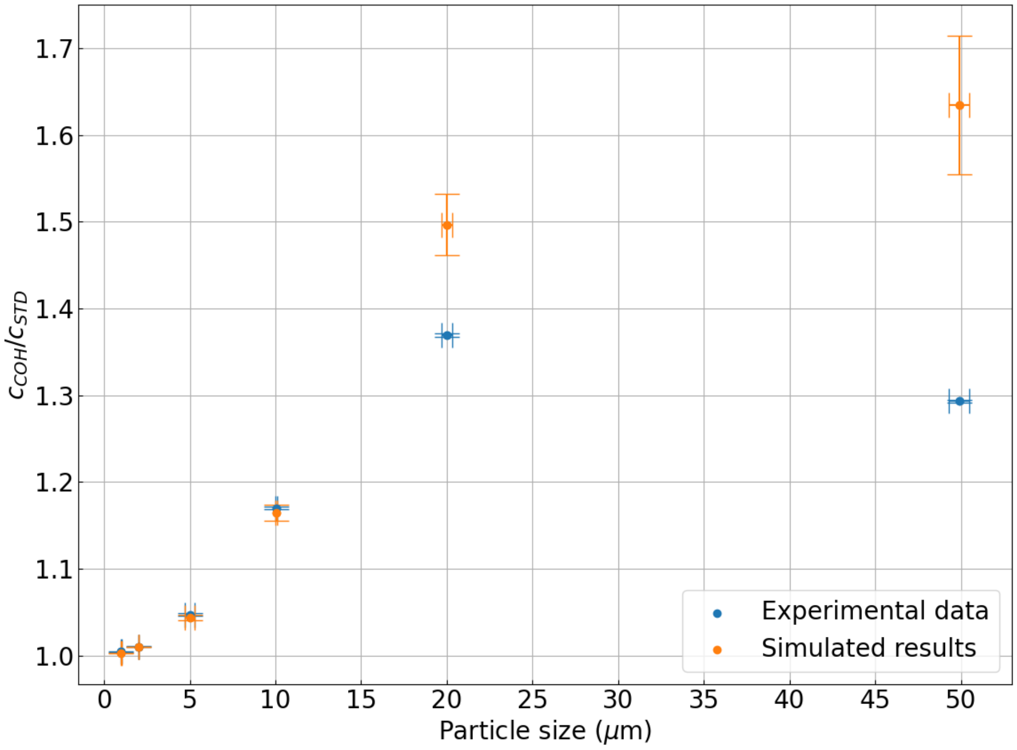

Figure 40: Comparison of measured $c_{\mathrm{COH}}/c_{\mathrm{STD}}$ values and predicted $c_{\mathrm{TRUE}}/c_{\mathrm{STD}}$ values from Mie scattering simulations for polystyrene microspheres.

For polystyrene microsphere sizes from 0.994 ± 0.01 µm to 10.07 ± 0.06 µm, the results of the Mie scattering simulations and of the experimental $c_{\mathrm{COH}}/c_{\mathrm{STD}}$ measurements are in good agreement (Table 6). The difference in c_{COH} and c_{STD} is on the order of the expected scattering bias that would affect the standard transmissometer, as predicted by the Mie scattering simulations. Although unmeasured systematic biases additional to the known scattering bias could still be present in the experimental set-up, these are not expected to have a substantial effect on the $c_{\mathrm{COH}}/c_{\mathrm{STD}}$ measurements at attenuation values in the stable, linear regime, as discussed previously. Therefore, the initial interpretation of the above results is that the coherence transmissometer is capable of completely accounting for the forward scattering bias for polystyrene microspheres with sizes from 0.994 ± 0.01 µm to 10.07 ± 0.06 µm.

For the 20.01 ± 0.33 µm and 49.9 ± 0.6 µm microspheres, the values of $c_{\mathrm{COH}}/c_{\mathrm{STD}}$ increasingly drop below the expected forward scattering bias indicated by $c_{\mathrm{TRUE}}/c_{\mathrm{STD}}$, suggesting that the coherence transmissometer is less effective at accounting for the full scattering bias for larger particle sizes. As discussed in Figures Figure 37 to Figure 39, the Mie scattering simulations become increasingly sensitive to small deviations in scatterer parameters for larger particle sizes. Therefore, it is possible that this increased deviation of $c_{\mathrm{COH}}/c_{\mathrm{STD}}$ from $c_{\mathrm{TRUE}}/c_{\mathrm{STD}}$ with increasing particle size could reflect increased difficulty in simulating the expected forward scattering bias for large particles. This increasing deviation requires further investigation and more in-depth modelling of the expected forward scattering bias.

The potential effect of settling of particles at larger particle sizes on the $c_{\mathrm{COH}}/c_{\mathrm{STD}}$ measurements should also be further investigated. The relationship between coherent scattering and different particle sizes and geometries must be better understood to fully understand the effect of settling on the measurements. If the degree of coherent scattering varies with particle size and geometry, it is possible that as larger particle sizes and certain geometries settle faster than other particles in the sample, the attenuation measured by the coherence transmissometer could begin to differ from that measured by the standard transmissometer.

For polystyrene microsphere sizes from 0.994 ± 0.01 μm to 20.01 ± 0.33 μm, the value of $c_{\mathrm{COH}}/c_{\mathrm{STD}}$ increases, as does that of $c_{\mathrm{TRUE}}/c_{\mathrm{STD}}$. This indicates that the expected forward scattering bias affecting the standard transmissometer increases with particle size and that the coherence transmissometer is generally capable of substantially counteracting this bias. However, for the 49.9 ± 0.6 μm microspheres, although the predicted scattering bias via $c_{\mathrm{TRUE}}/c_{\mathrm{STD}}$ continues to increase, the measured $c_{\mathrm{COH}}/c_{\mathrm{STD}}$ decreases compared to that for the 20.01 ± 0.33 μm microspheres. The predicted forward scattering bias continues to increase with size and there were no changes to the experimental configuration of the standard transmissometer for this data point. This suggests that the coherence transmissometer is less effective at counteracting the scattering bias for the 49.9 ± 0.6 μm polystyrene microspheres. The reasons for this are unclear; however, as was previously noted, the experimental procedure also had to be adapted for these particles due to their inability to stay in suspension long enough to obtain an appropriate time-averaged signal. The behaviour of this sample is unusual and could also benefit from further investigation in future studies.

Table 6: Comparison of $c_{\mathrm{COH}}/c_{\mathrm{STD}}$ experimental measurements and $c_{\mathrm{TRUE}}/c_{\mathrm{STD}}$ predictions from Mie scattering simulations for polystyrene microspheres.

Polystyrene microsphere size (μm)	$c_{\mathrm{COH}}/c_{\mathrm{STD}}$ measurement	$c_{\mathrm{TRUE}}/c_{\mathrm{STD}}$ prediction
0.994 ± 0.01	1.00 ± 3.72E^{-4}	1.00 ± 3.20E^{-5}

2.020 ± 0.015	1.01 ± 7.16E^{-4}	1.01 ± 2.32E^{-4}
5.0 ± 0.3	1.05 ± 1.73E^{-3}	1.04 ± 3.12E^{-3}
10.07 ± 0.06	1.17 ± 1.51E^{-3}	1.16 ± 9.18E^{-3}
20.01 ± 0.33	1.37 ± 2.20E^{-3}	1.50 ± 0.04
49.9 ± 0.6	1.29 ± 1.21E^{-3}	1.63 ± 0.08

5.5. Performance of coherence transmissometer: diatoms

To further document the performance of the coherence transmissometer compared to the standard transmissometer, attenuation measurements were made for a range of spherical phytoplankton samples of different particle sizes: *Nannochloropsis oculata*; *Chlorella vulgaris*; *Chlorocystis dangeardii*; and *Haematoccocus lacustris* (Table 7). The particle sizes of the samples ranged from 3 ± 1 µm to 37.5 ± 7.5 µm. Two samples were of freshwater phytoplankton and two were of marine phytoplankton. All samples were ordered from the Culture Collection of Algae and Protozoa (CCAP) at the Scottish Association for Marine Sciences (SAMS). Species with near-spherical geometries were chosen to remove any potential effect of particle shape on the performance of the coherence transmissometer.

Table 7: Phytoplankton sample information.

Species name	Particle size range (µm)	Medium
Nannochloropsis oculata	2 – 4	Marine
Chlorella vulgaris	4 – 6	Freshwater
Chlorocystis dangeardii	10 – 25	Marine
Haematoccocus lacustris	30 – 45	Freshwater

The experimental procedure for measuring the attenuation of the phytoplankton samples followed the general procedure described for the polystyrene microspheres. For the freshwater species, Milli-Q was used as a base for diluting the phytoplankton samples, as with the polystyrene microspheres. For the marine species, artificial seawater was produced as a base for dilution at 35 g of salt (NaCl, Source Chemicals) per 1 L of Milli-Q. For these species, the cuvette was also flushed out multiple times with artificial seawater rather than with Milli-Q in the experimental procedure, to minimize turbulence due to changes in salinity within the cuvette. The attenuations of the marine samples were calculated relative to beam attenuation through artificial seawater rather than Milli-Q.

For the *Chlorocystis dangeardii* species, the particles rapidly dropped out of suspension, similar to the behaviour of the 49.9 ± 0.6 µm polystyrene microspheres. The experimental procedure and analysis of these samples therefore followed that laid out for the 49.9 ± 0.6 µm polystyrene microspheres. This behaviour is interesting, as the initial hypothesis for the inability of the microspheres to stay in suspension was attributed to them being the largest in the measured size range. However, the size of the *Chlorocystis dangeardii* is quoted to be from 10 – 25 µm, a size range which did not exhibit this problem for the polystyrene microsphere samples. Additionally, the largest size of the phytoplankton species does not exhibit this same behaviour. It is unclear if this is due to any different behaviours between salt and freshwater samples. It was expected that the primary factor contributing to the scattering behaviour would be the particle size and geometry.

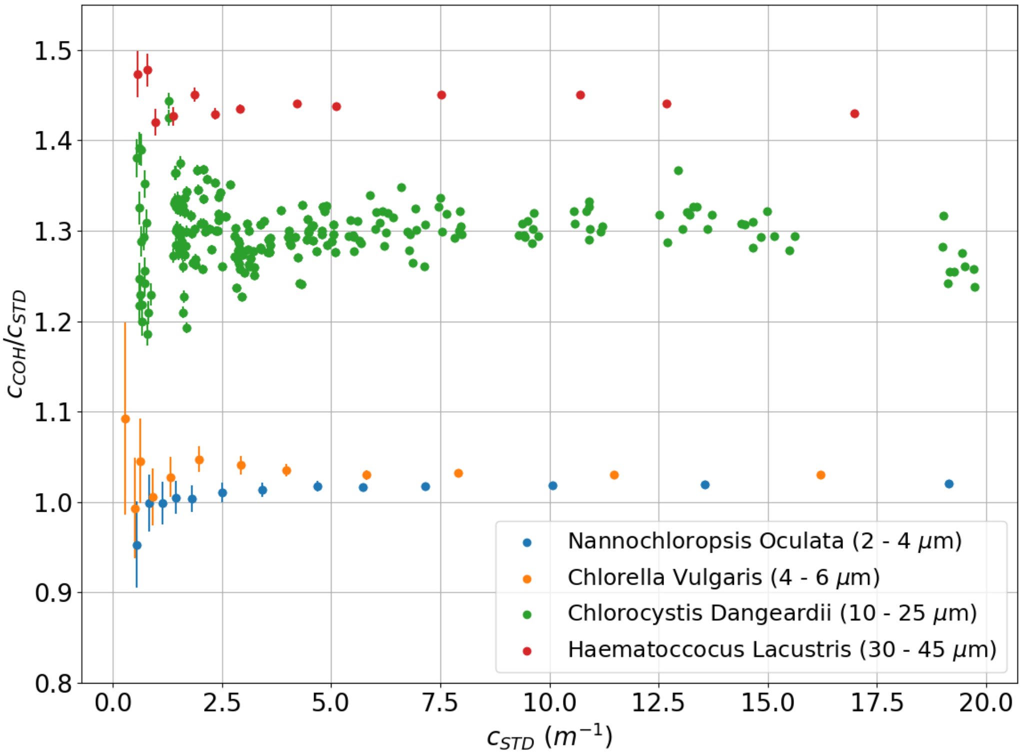

Figure 41: Attenuations measured by the coherence transmissometer with respect to that of the standard transmissometer (c_{COH}/c_{STD}) for a range of spherical phytoplankton species, with error bars calculated as described in Section 3.2.3.

Similar to the results for the polystyrene microspheres, the coherence transmissometer measured a higher attenuation than the standard transmissometer for all phytoplankton samples, showing an increasing divergence of c_{COH} from c_{STD} with increasing particle size (Figure 41). The nature of the c_{COH}/c_{STD} results as a function of c_{STD} is similar to that for the polystyrene microspheres, with a linear relationship between the transmissometers for attenuations above some threshold. Below this threshold, nonlinearities appear in the $c_{\mathrm{COH}}/c_{\mathrm{STD}}$ measurements that are attributed to the increasing influence of noise sources on the transmissometers, as previously discussed. The regime where a stable, linear relationship between the transmissometers could be obtained for the phytoplankton species was chosen to be above c_{STD} = 2 m^{-1}, the same as that for the polystyrene microspheres. For c_{STD} > 2 m^{-1}, the best fit values of $c_{\mathrm{COH}}/c_{\mathrm{STD}}$ were found to be: 1.02 ± 6.35E^{-4} for *Nannochloropsis oculata* (2 – 4 µm); 1.03 ± 9.07E^{-4} for *Chlorella vulgaris* (4 – 6 µm); 1.30 ± 1.51E^{-3} for *Chlorocystis dangeardii* (10 – 25 µm); and 1.44 ± 3.07E^{-3} for *Haematoccocus lacustris* (30 – 45 µm). This increasing trend in $c_{\mathrm{COH}}/c_{\mathrm{STD}}$ is shown in Figure 42.

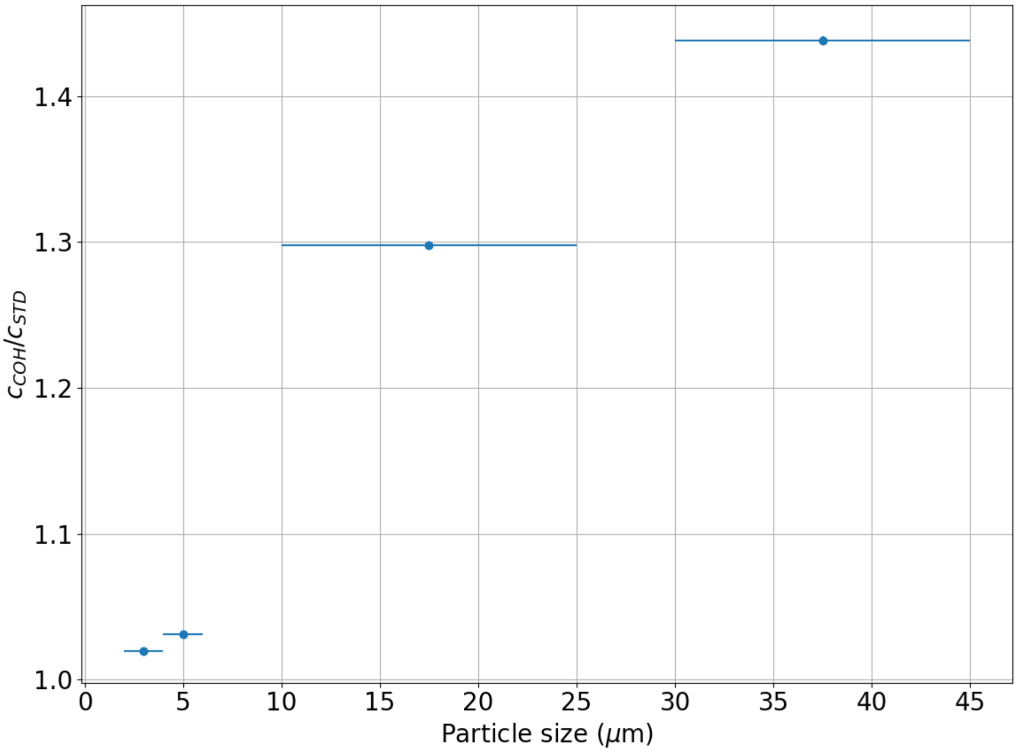

Figure 42: Best linear fit of $c_{\mathrm{COH}}/c_{\mathrm{STD}}$ for c_{STD} > 2 m^{-1} for all phytoplankton species samples as a function of particle size.

As with the polystyrene microspheres, Mie scattering simulations were carried out for the phytoplankton species to provide a reference for the expected degree of forward-scattering bias for each sample. The sensitivity of the Mie scattering simulations for each phytoplankton species to changes in the refractive index of the phytoplankton particles was also assessed through a refractive index range of approximately 1.39 – 1.43. This range was taken by using a relative refractive index of phytoplankton of 1.05 and a refractive index of seawater of 1.34, giving a real refractive index of phytoplankton of 1.41 and then allowing a variation of ± 2% to give a refractive index variation similar to that of the polystyrene microspheres (Aas, 1996). This range of refractive index values is within those considered typical for healthy phytoplankton (Ackleson et al., 1988). The same approach to calculating $c_{\mathrm{TRUE}}/c_{\mathrm{STD}}$ was used as detailed for the polystyrene microspheres, with an altered refractive index appropriate for that of phytoplankton and particle sizes and distribution widths matching the quoted size range for each species.

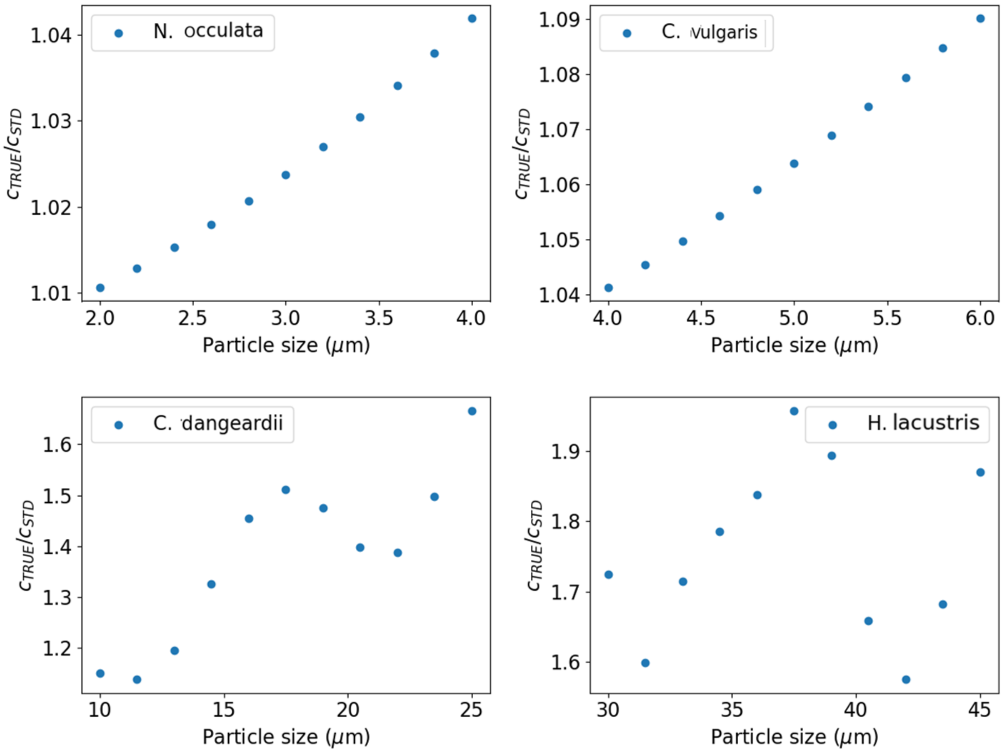

Figure 43: Sensitivity of $c_{\mathrm{TRUE}}/c_{\mathrm{STD}}$ simulations as a function of particle size for all algae species.

For all four algae species, a substantial sensitivity of the simulations to changes in the particle size was observed. For the 2 – 4 µm *Nannochloropsis occulata*, the $c_{\mathrm{TRUE}}/c_{\mathrm{STD}}$ estimates varied by approximately 3% over the particle size range. For the 4 – 6 µm *Chlorella vulgaris*, the $c_{\mathrm{TRUE}}/c_{\mathrm{STD}}$ estimates varied by approximately 5% over the particle size range. For the 10 – 25 µm *Chlorocystis dangeardii*, the $c_{\mathrm{TRUE}}/c_{\mathrm{STD}}$ estimates varied by approximately 50% over the particle size range. Finally, for the 30 – 45 µm *Haematoccocus lacustris*, the $c_{\mathrm{TRUE}}/c_{\mathrm{STD}}$ estimates varied by approximately 35% over the particle size range. The phytoplankton species with larger initial particle sizes were an order of magnitude more sensitive to changes in particle size than the samples with smaller initial particle sizes.

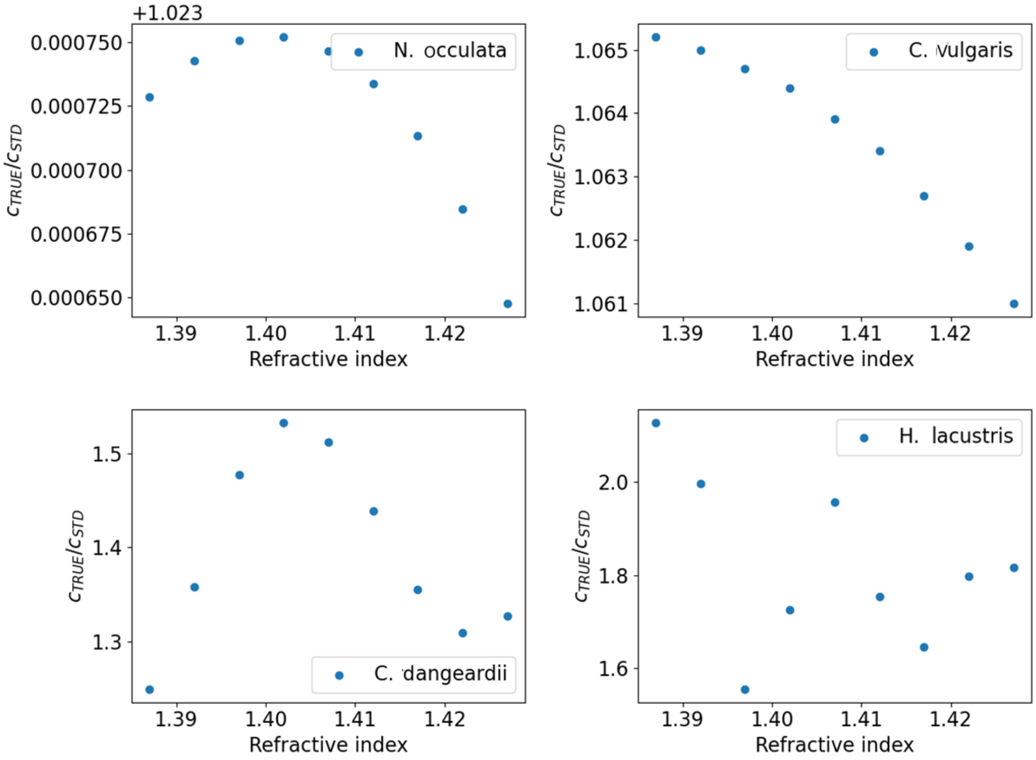

Figure 44: Sensitivity of $c_{\mathrm{TRUE}}/c_{\mathrm{STD}}$ *simulations as a function of refractive index for all algae species.*

For the *Nannochloropsis occulata*, the $c_{\mathrm{TRUE}}/c_{\mathrm{STD}}$ estimates did not vary substantially over the refractive index range. For the *Chlorella vulgaris*, the $c_{\mathrm{TRUE}}/c_{\mathrm{STD}}$ estimates varied on the order of 0.4% over the refractive index range. For the *Chlorocystis dangeardii*, the $c_{\mathrm{TRUE}}/c_{\mathrm{STD}}$ estimates varied by approximately 30% over the refractive index range. Finally, for the *Haematoccocus lacustris*, the $c_{\mathrm{TRUE}}/c_{\mathrm{STD}}$ estimates varied by approximately 50% over the refractive index range. The general result is that the species with larger particle sizes (and following from that, wider size ranges) are more sensitive to changes in the refractive index of the particles.

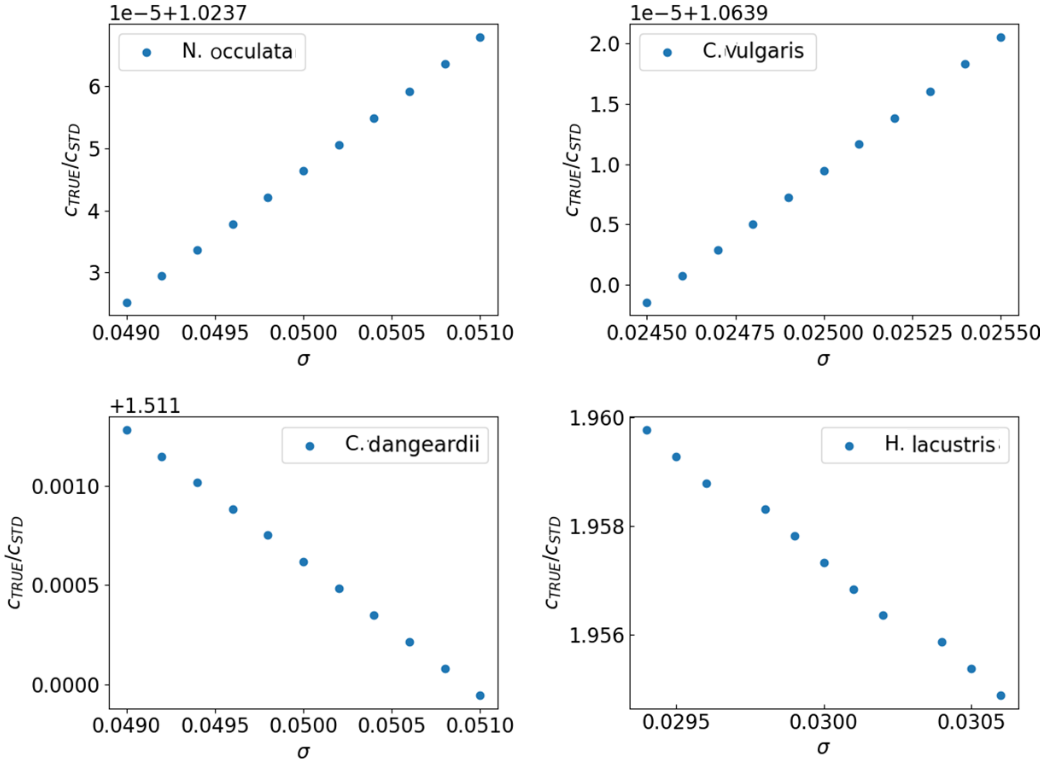

Figure 45: Sensitivity of $c_{\mathrm{TRUE}}/c_{\mathrm{STD}}$ simulations to changes in sigma, related to particle size distribution width, for all algae species.

Finally, the sensitivity of the $c_{\mathrm{TRUE}}/c_{\mathrm{STD}}$ predictions to changes in the particle size distribution width were assessed. Although there is an increase in sensitivity towards the larger particles, for all species there is not a large change in $c_{\mathrm{TRUE}}/c_{\mathrm{STD}}$ with particle size distribution width.

Overall, the $c_{\mathrm{TRUE}}/c_{\mathrm{STD}}$ predictions calculated via Mie scattering simulations were most sensitive to changes in the particle size and the refractive index of the phytoplankton particles. This sensitivity was strongest for the two larger phytoplankton species: *Chlorocystis dangeardii* and *Haematoccocus lacustris*. This indicates that it becomes more difficult to simulate the scattering behaviour of particles of larger sizes, suggesting that these values of $c_{\mathrm{TRUE}}/c_{\mathrm{STD}}$ may be less reliable than those calculated for small particles. Further modelling could be used to investigate the expected scattering behaviour of each particle type more carefully; however, these estimates coupled with the above-described sensitivity analysis are considered sufficient for making a broad comparison between the experimental transmissometry data and the expected degree of scattering bias for each particle type and size.

As with the polystyrene microspheres, the errors associated with the $c_{\mathrm{TRUE}}/c_{\mathrm{STD}}$ sensitivity to particle size, refractive index, and particle size distribution width were combined in quadrature to produce error bars in the $c_{\mathrm{TRUE}}/c_{\mathrm{STD}}$ estimates. The $c_{\mathrm{TRUE}}/c_{\mathrm{STD}}$ estimates were then plotted on the same graph as the $c_{\mathrm{COH}}/c_{\mathrm{STD}}$ measurements for comparison (Figure 46).

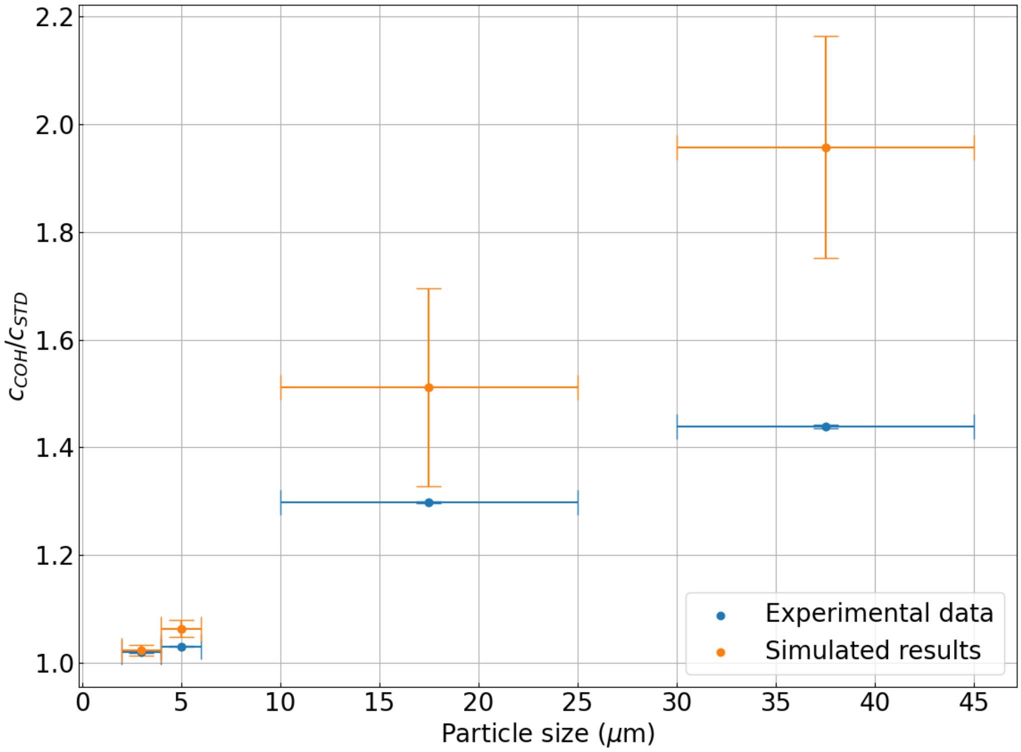

Figure 46: Comparison of $c_{\mathrm{COH}}/c_{\mathrm{STD}}$ (experimental data) and $c_{\mathrm{TRUE}}/c_{\mathrm{STD}}$ (simulated scattering bias) for all phytoplankton species measured as a function of particle size.

Table 8: Values of $c_{\mathrm{COH}}/c_{\mathrm{STD}}$ and $c_{\mathrm{TRUE}}/c_{\mathrm{STD}}$ for all phytoplankton species used in this study.

Species name	Particle size range (μm)	$c_{\mathrm{COH}}/c_{\mathrm{STD}}$ measurement	$c_{\mathrm{TRUE}}/c_{\mathrm{STD}}$ prediction
Nannochloropsis oculata	2 – 4	$1.02 \pm 6.35\mathrm{E}^{-4}$	$1.02 \pm 9.95\mathrm{E}^{-3}$
Chlorella vulgaris	4 – 6	$1.03 \pm 9.07\mathrm{E}^{-4}$	$1.06 \pm 1.56\mathrm{E}^{-2}$
Chlorocystis dangeardii	10 – 25	$1.30 \pm 1.51\mathrm{E}^{-3}$	1.51 ± 0.18
Haematoccocus lacustris	30 – 45	$1.44 \pm 3.07\mathrm{E}^{-3}$	1.96 ± 0.21

For all particle sizes, simulations predict values of $c_{\mathrm{TRUE}}/c_{\mathrm{STD}}$ that are greater than unity and increase with increasing particle size (Table 8). For all sizes of phytoplankton species, the simulated $c_{\mathrm{TRUE}}/c_{\mathrm{STD}}$ values are greater than or equal to the measured $c_{\mathrm{COH}}/c_{\mathrm{STD}}$ values. The difference between $c_{\mathrm{TRUE}}/c_{\mathrm{STD}}$ and $c_{\mathrm{COH}}/c_{\mathrm{STD}}$ increases with increasing particle size and expected scattering bias, indicating that the coherence transmissometer accounts less effectively for the overall expected scattering bias with increasing phytoplankton particle size. This differs slightly from the comparison between $c_{\mathrm{TRUE}}/c_{\mathrm{STD}}$ and $c_{\mathrm{COH}}/c_{\mathrm{STD}}$ for the polystyrene microspheres, where the measurements and simulations were in relatively good agreement up to sizes of approximately 10 µm and an increasing difference between values occurred from approximately 20 µm to 50 µm. A comparison between the simulated and measured values for both particle types can be seen in Figure 47. This may seem to initially suggest that the coherence transmissometer more fully accounts for the expected scattering bias for polystyrene microspheres of sizes up to 10 µm than for larger microsphere sizes or for phytoplankton; however, it should be observed that the error bars associated with the phytoplankton simulations of $c_{\mathrm{TRUE}}/c_{\mathrm{STD}}$ are larger than those for the polystyrene microspheres.

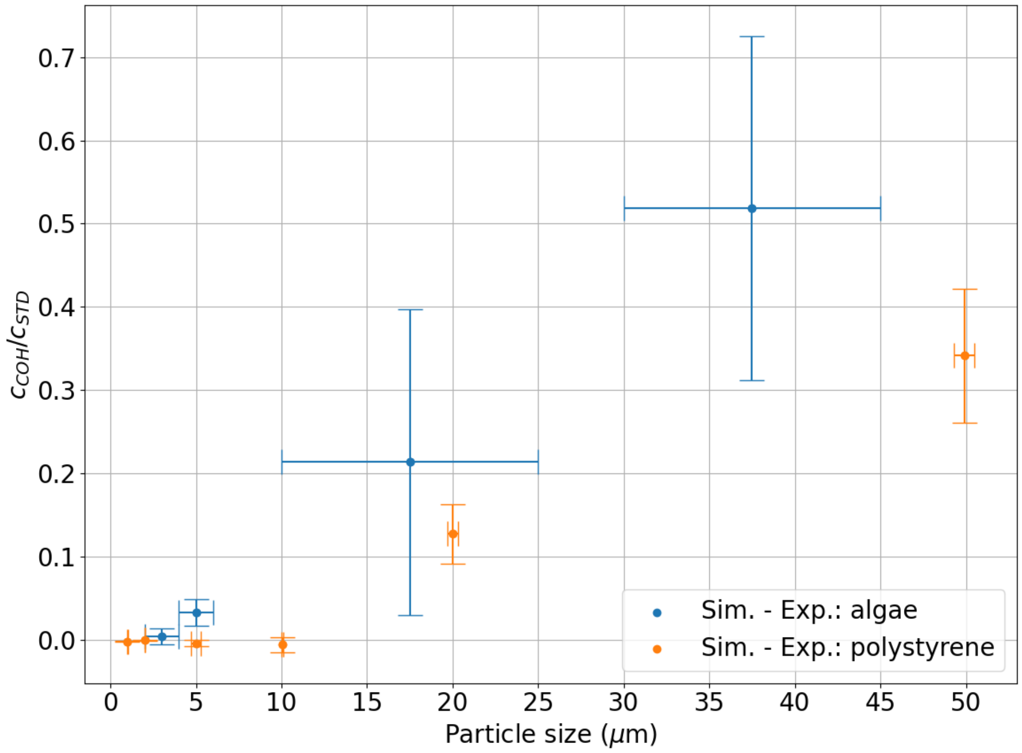

Figure 47: Difference between simulated scattering bias ($c_{\mathrm{TRUE}}/c_{\mathrm{STD}}$) and measured coherence transmissometer performance ($c_{\mathrm{COH}}/c_{\mathrm{STD}}$) for phytoplankton species (in blue) and polystyrene microspheres (in orange) as a function of particle size.

This reflects the large sensitivity of the $c_{\mathrm{TRUE}}/c_{\mathrm{STD}}$ simulations to the information provided by the supplier regarding the size range and refractive index of the phytoplankton species. Furthermore, the simulations become increasingly sensitive at larger particle sizes, potentially casting doubt on the accuracy of these predicted values relative to the experimental measurements. A potential interpretation of the change in the Mie scattering predictions at large particle sizes could be due to the increasing effect of particle flocculation. Flocs of particles that have aggregated together from smaller particles can no longer be represented as a single independent scatterer with only one refractive index and consistent IOPs (Mobley, 2020). It is known that the scattering behaviour from different positions on the same floc can differ, leading to different scattering coefficients across the “particle” and the potential for complex coherence effects as the scattering functions from nearby positions on the floc interact with each other. Mie theory can also not account effectively for complexity in the structure and distribution of mass of aggregations of particles, since Mie theory assumes homogenous, spherical particles. The accuracy of this modelling approach, particularly exploring the effect of flocculation, should be explored further in future work.

Broadly, it can be seen that, for both particle types, there is an expected scattering bias that increases with increasing particle size, and the measurements made by the coherence transmissometer relative to those made by the standard transmissometer make positive progress towards accounting for this scattering bias in attenuation measurements (Figure 48).

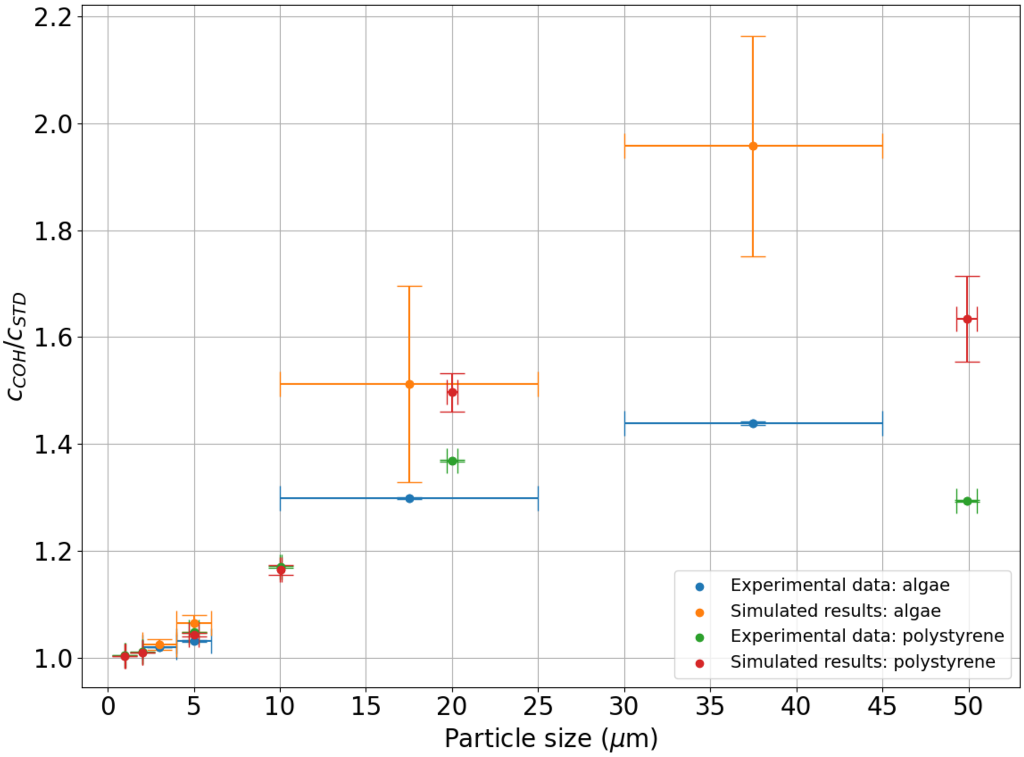

Figure 48: Comparison of simulated and experimentally measured values of c_{TRUE}/c_{STD} *and* c_{COH}/c_{STD} *for both particle types.*

In all cases, the coherence transmissometer measures a higher attenuation than the standard transmissometer when making simultaneous measurements through the same sample, suggesting the capture of less forward-scattered light by the coherence transmissometer. There is broadly good agreement between the coherence transmissometer correction and the predicted scattering bias for both particle types up to 10 μm, suggesting that the coherence transmissometer is able to substantially account for the expected scattering bias in this size range. Although the agreement between predicted and measured values becomes less strong at larger particle sizes, the coherence transmissometer still measures a higher attenuation than the standard transmissometer in each case and provides an attenuation measurement that is consistently closer to the true, “gold-standard” attenuation free from scattering bias than the current standard measurement. While the performance of the coherence transmissometer and accuracy of scattering simulations at higher particle sizes (> 20 μm) should be investigated in further study, the results of this work suggest that the coherence transmissometer is overall successful at reducing the measured scattering bias in attenuation across all particle sizes investigated.

5.7. Outlook and next steps

The results shown in this chapter show promising progress towards the development of a transmissometer free from scattering bias, with the coherence transmissometer measuring between 2–44% and 1–37% higher attenuation than the standard lens-and-pinhole method for phytoplankton species and polystyrene microspheres of increasing size, respectively. To put these results into context, the following limitations of the study and suggested next steps should be considered.

It is difficult to make an exact comparison between the coherence transmissometer and the standard transmissometer without quantitatively knowing the collection angle of both arrangements. Efforts have been made to make these as similar as possible based on the set-up geometry in the absence of a quantitative measurement; however, the exact effect of the diffraction grating on the collection angle of the coherence transmissometer has not been quantified. It is believed that the spreading due to diffraction from the grating occurs only along one axis (with the other axis simply reflecting the light), resulting in an elliptical collection angle which is not trivial to calculate but could potentially be calculated using a Fourier optics approach in future studies. If the collection angle of the coherence transmissometer was comparatively smaller, a positive offset in $c_{\mathrm{COH}}/c_{\mathrm{STD}}$ may be introduced. The level of this offset relative to magnitude of change in collection angle has not been studied; however, previous investigations have highlighted the sensitivity of the system to offsets, particularly at low and high attenuations (Figure 25).

It is presumed that the accuracy of the $c_{\mathrm{TRUE}}/c_{\mathrm{STD}}$ simulations becomes less reliable with increasing particle size, as indicated by the increase in sensitivity to changes in all parameters. This could be due to larger phytoplankton exhibiting more complex internal structure, although this would not account for the behaviour of large polystyrene microspheres which are extremely uniform. An alternate explanation could be that the Bessel functions involved in the modelling approach become less well approximated at larger particle sizes. This makes an accurate evaluation of the performance of the coherence transmissometer relative to expected scattering bias more difficult at large particle sizes. Future studies of this system could assess the performance of different modelling techniques, in comparison to the Mie theory approximation implemented herein, in predicting the behaviour of the coherence transmissometer including the effect of coherent scattering. For example, Muinonen et al. (2012) evaluated the appearance of coherent effects in backscattering scenarios using both the superposition T-matrix method for solving the

Maxwell’s equations and also using a Monte Carlo based approach that account specifically for coherence.

The behaviour of the coherence transmissometer when assessing the attenuation of samples composed of non-spherical particles has not been evaluated. Non-spherical particles make up a substantial proportion of natural water samples and it would be interesting to examine any shape/internal structure dependent effects. Changes in polarization associated with scattering from long-chain particles are expected to have some effect on the measurements made by the coherence transmissometer, which uses a polarization-sensitive diffraction grating. The degree of this effect should be evaluated to determine the expected level of error introduced; this error can potentially be minimized by choice of a diffraction grating with low polarization sensitivity.

Although the presence of coherent scattering has been suggested to exist at the coherence transmissometer via the results shown in Figure 33 and the review of the literature, the exact proportion of light that was coherently scattered in each of the above experimental cases is unknown. It is also unknown if this proportion of coherent forward scattered light remains as a constant percentage of the total amount of forward scattered light with changing particle size and type. To make correct attenuations measurements, it is necessary to determine the coherent scattering amount and remove its effects from the attenuation calculations.

To summarize, the key sources of uncertainty remaining in the device performance relate to the effect of the elliptical and unquantified collection angle, the potential discrepancy between Mie modelling predictions and the experimental results, and the effect of coherent scattering on the attenuation measurements. Although it has been noted that the behaviour of the transmissometer may be sensitive to alignment changes or perform differently for non-spherical particles with internal structure, these sensitivities are not expected to affect the key results shown in this chapter. Regarding the effect of the elliptical collection angle, it is clear from the results in Figure 33 that changing the collection angle has the potential to substantially change the ratio between transmissometer measurements (on the order of 20% in this case). It is expected that the efforts made to match the path lengths and optics used in both transmissometers will have reduced this error far below the 20% value; however, this should be quantified. Regarding the divergence of the Mie scattering predictions from observations, it is expected that the unreliability of the Mie scattering modelling at large particle sizes (> 10 µm) is the most substantial source of error since this effect is well-known in the field. However, this effect is not well-quantified in the literature and so it is difficult to determine how substantial this effect may be compared to the contribution of coherent scattering. This comparison should be the key focus of future study.*Figure 30*

The recommended next steps following on from this research are as follows. Determining the effect of the diffraction grating on the collection angle of the coherence transmissometer will allow an exact, quantitative comparison between it and the standard transmissometer, removing any potential offsets due to this issue. Additionally, the accuracy of the modelling approach used herein, especially at larger particle sizes, should be examined.

An extreme sensitivity of both transmissometers to slight changes in the position and angles of optics and photodetectors in the beam path was observed. For example, tilting a photodetector on the order of 1° was capable of changing $c_{\mathrm{COH}}/c_{\mathrm{STD}}$ by up to 5% in some cases. In practice when taking the data presented in this chapter, the positions of optics, acquisition devices, and the cuvette were not manually changed throughout the course of all polystyrene microsphere and phytoplankton species measurements, to minimize change in signal due to alignment changes. However, for future study, a more rigid set-up is recommended, both for future laboratory work and any in-situ applications. For example, a cage-mounted optical set-up would be less prone to changes in the angles and positions of optics.

Once the coherence transmissometer has been updated to account for the previously described sensitivity, it would be interesting to measure a hyperspectral dataset for known particle types (such as the polystyrene microspheres or phytoplankton) compared to the standard transmissometer. This will indicate if there is any wavelength dependence of the correction applied by the coherence transmissometer to the standard method.

Ideally, in the further future, this device could be adapted for use as an in-situ optical sensor. If this implementation were to succeed, it would be necessary to make changes to the geometry and set-up to ensure robustness of alignment to noise, a set-up geometry that can be encased to withstand high pressures, and real-time calculations of attenuation based on a known reference value.

Conclusions

Since their inception, standard transmissometers used in the field of marine optics that utilize a combined lens-and-pinhole approach to reject scattered light have been plagued by accuracy issues related to the collection of forward-scattered light. This limitation in the accuracy of standard transmissometers is due to the ability of forward-scattered light to pass through the pinhole when scattered at angles less than the collection angle of the device. This can be a large problem, since marine particles of increasing sizes scatter light increasingly preferentially at small forward angles. For example, Boss et al. (2009) and McKee et al. (2013) both measure and predict errors between 50–80% in ac-9 beam attenuation measurements as a result of scattering bias.

Scattering correction algorithms have been developed to account for this limitation in ac-9/s transmissometers; however, these require the accurate measurement of backscattering coefficients and require further uptake and validation to determine their reliability across multiple water types (McKee et al., 2013). As it stands, there is no “gold standard” approach to making accurate measurements of beam attenuation independent of the device geometry and with full rejection of scattered light from the measurement. The current most-common and recommended approach for dealing with scattering errors in the measurement of beam attenuation coefficients is to make no attempt to correct for these errors but instead to report the uncorrected results alongside the parameters of the transmissometer (i.e., path length, collection angle, etc.). The IOCCG protocol regarding beam transmission and attenuation measurements highlights the need for new approaches that can provide unambiguous measurements of the beam attenuation coefficient that are free from scattering errors (Boss et al. 2019).

The motivation of this thesis has been to develop and test an alternate transmissometer design that aims to fully reject scattered light from the attenuation measurements, creating a transmissometer that measures “true attenuation” regardless of the device parameters. A novel device of this type is necessary for the field of marine optics in order to make consistent and accurate measurements of attenuation possible. This in turn would allow more accurate determination of radiative transfer, particle size distributions, and plankton biomass, among other factors related to the beam attenuation.

Summary of research

To address the problem of the collection of forward-scattered light through the pinhole with a finite collection angle, a novel transmissometer design that accounts for the degradation of spatial coherence of light with scattering was proposed. This novel transmissometer utilizes a diffraction grating to diffract only light that is spatially coherent into the –1st order diffraction mode; it was initially theorized that only transmitted light would maintain its spatial coherence, resulting in a transmissometer with an effective collection angle of 0°.

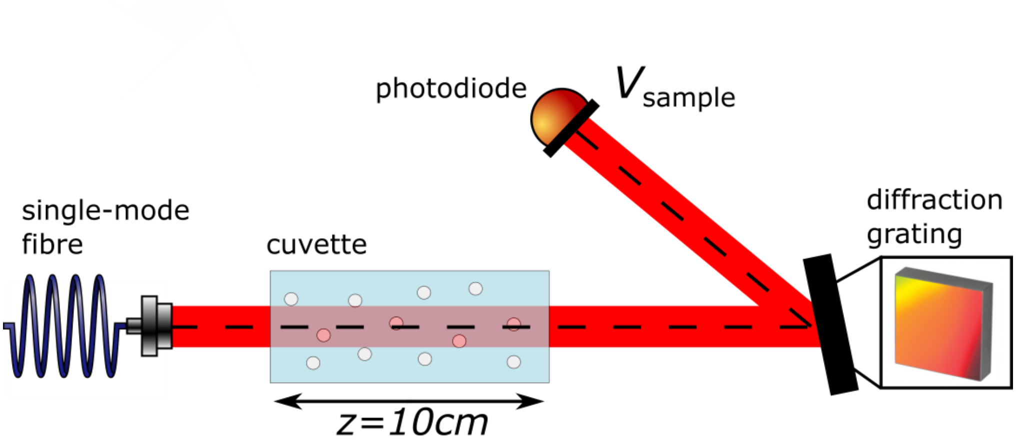

Figure 49: Zoomed-in schematic of the key parts of the coherence transmissometer. All that is required is a spatially coherent light source, a cuvette, a diffraction grating, and a photodetector. The cuvette is 10cm long, there are elements for polarization control and power calibration prior to the cuvette, and a beamsplitter after the cuvette to direct some light to the standard transmissometer.

To compare the performance of this novel transmissometer design against that of a standard design, an experimental set-up was produced to simultaneously measure the attenuation through a 10-cm cuvette with the novel coherence-based transmissometer and with a lens-and-pinhole transmissometer based on the WETLABS ac-9 series of devices with a collection angle of 0.9°. This simultaneous measurement was facilitated via a beamsplitter after the cuvette and a simultaneous voltage measurement using a multi-channel Picoscope.

An initial prototype of the coherence-based transmissometer was produced and found to consistently measure higher attenuations (c_{COH}) than that measured by a standard-design transmissometer (c_{STD}) for both liquid antacid and diatom samples at attenuations larger than some threshold. For both types of sample, two regimes were observed. First, a regime above some attenuation threshold where the relationship between c_{COH} and c_{STD} was stable and linear and generally $c_{\mathrm{COH}} > c_{\mathrm{STD}}$. Second, a regime below that attenuation threshold where the relationship between c_{COH} and c_{STD} was nonlinear and c_{COH} did not have a fixed sign relative to c_{STD} across the datasets. The nonlinear regime at low thresholds was theorized to be most likely due to the presence of noise terms in the experimental set-up, such as sensitivities to beam alignment changes across multiple measurements and the resolution of the voltage measurements. As such, a newer prototype of the transmissometer was developed that accounted for multiple potential sources of noise and systematic bias, as discussed in Chapter 5.

The nonlinearity between c_{COH} and c_{STD} at low attenuations was identified to be likely due to the presence of noise terms in the experimental set-up; simulations of the effect of adding small error terms to the $c_{\mathrm{COH}}/c_{\mathrm{STD}}$ calculations highlighted the extreme sensitivity of the system to noise terms in the order of 1–10%.

To reduce the sensitivity of the final attenuation measurements to noise terms in the system and to improve their overall accuracy, the following steps were taken. A new procedure was introduced for making reference attenuation measurements whereby multiple ultrapure water measurements were made prior to all attenuating sample measurements and the median of these was taken as the most accurate reference. Further, the experimental procedure was updated to keep the cuvette fixed in place throughout the entire data run; potentially introducing an increased risk of contamination to the cuvette due to reduced cleaning, but reducing the risk of alignment changes which were considered to have a large effect on the attenuation measurements. An increased amount of data was taken for each attenuation measurement to improve the measurement precision. Background light measurements were taken after every sample measurement rather than a global measurement to improve accuracy. The light levels reaching each photodetector were maximized, improving the transmissometer sensitivities. Finally, a focusing lens was added to the coherence transmissometer to reduce sensitivity to cuvette alignment.

After implementing all of the above changes to the initial transmissometer prototype, up to a factor of five improvement in device sensitivity was observed when measuring the attenuation of 0.994 ± 0.01 µm polystyrene microspheres. The precision also increased by approximately an order of magnitude, with the lowest $c_{\mathrm{COH}}/c_{\mathrm{STD}}$ value in the regime for the 0.994 ± 0.01 µm microspheres equalling 0.96 ± 0.02 at 0.45 m^{-1} in the optimized case as opposed to equalling 1.04 ± 0.33 at 0.35 m^{-1} in the unoptimized case. However, these improvements coincided with a switch to $c_{\mathrm{COH}} < c_{\mathrm{STD}}$ across all measurements, indicating a potential change in collection angle of the coherence transmissometer. This result threw the initial hypothesis that only negligible amounts of forward-scattered light would retain any spatial coherence into question and required further investigation.

Conclusions

On further investigation, it was discovered that an amount of spatial coherence was retained with forward-scattered light in the system, large enough to alter the $c_{\mathrm{COH}}/c_{\mathrm{STD}}$ behaviour on the order of 20%. This finding indicated that a negligible amount of spatially coherent scattered light could not be assumed in measurements of micrometer-sized particles and that the key design of the coherence transmissometer must be altered to account for this.

A new iteration of the coherence transmissometer was developed that combined the directional filter provided by a lens and pinhole with the coherence filter provided by the diffraction grating. The collection angle of the coherence transmissometer was made broadly similar to that of the standard transmissometer, within the limited ability of this study to exactly quantify the elliptical collection angle, to compare the attenuations measured with and without a coherence filter for the same collection angle and path length.

When the geometry of the coherence transmissometer was matched to that of the standard transmissometer, the coherence transmissometer consistently measured a higher attenuation than the standard transmissometer in a stable regime defined as greater than $c_{\mathrm{STD}} = 2\ \mathrm{m}^{-1}$ for all particle types and sizes for both polystyrene microspheres from 0.994 ± 0.01 µm to 49.9 ± 0.6 µm and various spherical diatom species with sizes from 3 ± 1 µm to 37.5 ± 7.5 µm.

The difference in the attenuations measured by the coherence and standard transmissometers generally increased with particle size for both the polystyrene microspheres and the spherical diatom species. This was hypothesized to be due to the standard transmissometer increasingly capturing more forward-scattered light for larger particle sizes as the VSF became more strongly forward peaked; the coherence transmissometer was expected to be largely immune to this problem, excluding the potential effect of coherently scattered light.

The experimental results of increasing $c_{\mathrm{COH}}/c_{\mathrm{STD}}$ with particle size for both sample types were broadly similar to predictions of the attenuation error made via Mie scattering simulations. The agreement between these predictions and the experimental results was better for lower particle sizes, potentially indicating that the Mie scattering results become less reliable at larger particle sizes which is a well-known problem with numerical implementations of Mie theory as the convergence of the expansion terms is more difficult to achieve as the size parameter becomes larger. The divergence between experimental measurements and simulations should be investigated further in the future.

On the whole, these results show that the coherence transmissometer that utilizes both a spatial coherence filter via the diffraction grating and a directional filter via the lens and pinhole is consistently capable of measuring higher attenuations than the standard transmissometer that uses only a directional filter for both marine and plastic spherical particles with sizes on the order of 1 to 50 micrometers. Particularly at the lower particle sizes in the range, the increase in the attenuation provided by the coherence transmissometer is on the order of the necessary scattering bias correction, suggesting that a large reduction in scattering bias plays a key role in this effect.

In general, the addition of a filter which accounts for the degradation in spatial coherence of light when it is scattered to a standard transmissometer design allows for a substantial increase in the measured attenuation for both plastic and algae spherical sample types at sizes in the micrometer to tens of micrometers regime. The degree of change in the attenuation measurements for particle sizes from 1–10 µm is on the order of the expected attenuation error due to scattering, indicating that a transmissometer that incorporates both directional and coherence filtering can almost entirely reduce the scattering error and push progress towards a true attenuation measurement.

Outlook and future work

The introduction in this thesis of a transmissometer that acknowledges the change in spatial coherence of a coherent light source due to scattering and uses a diffraction grating, in addition to the standard lens-and-pinhole design, to filter for this scattered light provides another tool for researchers in marine optics to reduce the effect of scattering errors on beam attenuation measurements. This approach provides a method that is theoretically easier to implement than, for example, scattering correction methods, such as the iterative correction method proposed by McKee et al. (2013), which present an extra difficulty in taking additional backscattering measurements alongside beam attenuation coefficients in order to make the corrections. Compared to methods using OAM transmissometers to filter for coherence, this thesis presents a design that is less complex and more economical to implement, since it does not rely on expensive, specialised optics to encode and decode OAM information. Furthermore, in comparison to both of these methods, it is expected that the diffraction grating-based design presented in this thesis does not require extensive data processing or corrections to obtain a beam attenuation measurement, aside from typical corrections for parameters such as temperature stability, for example. Depending on how significant the effect of coherent forward-scattering is, it is possible that this coherence transmissometer could be utilised with a relatively large collection angle compared to the LISST-200X (0.018°) or LISST-Tau (1°), making it less sensitive to alignment sensitivities or changes in turbulence. In comparison to other commercial instruments for measuring the beam attenuation coefficient, such as the LISST-200X or the LISST-Tau, the relative performance of this transmissometer should be further evaluated in later studies. Nonetheless, the coherence transmissometer provides at minimum an additional tool for determining the beam attenuation coefficient which can be compared with other methods under different measurement conditions to further understand and reduce scattering errors. For example, the iterative scattering method of McKee et al. (2013) has been evaluated alongside and shown good agreement with data from a LISST instrument with a collection angle of 0.027°. Future studies of the beam attenuation coefficient could involve comparing scattering correction methods to coherence filtering methods (i.e., the work of this thesis or OAM transmissometers) to commercial instruments such as the LISST devices.

Although the behaviour of the coherence transmissometer must be explored further as a function of particle geometry and light wavelength, and the exact effect of coherent forward scattering should be quantified for each scenario, it is recommended that future transmissometer designs should consider how they can account for the change in spatial coherence that commonly occurs on scattering in order to make more accurate attenuation measurements. Any system that combines both directional and coherence filtering, whether in the form described above or another, shows promise for cutting down the substantial forward-scattering bias that has plagued attenuation measurements in the marine optics field.

However, to more accurately determine the improvements made by the addition of a coherence filter and how these compare to the expected attenuation error from scattered light collection, the following future steps should be made. The exact effect of the diffraction grating on the collection angle of the coherence transmissometer must be determined to directly compare transmissometer performance with and without a coherence filter. Similarly, a quantitative study of the amount of coherently scattered light in this system for particle sizes in the micrometer to tens of micrometer regime should be performed to determine how significantly coherently scattered light changes the attenuation measurements, if this effect is constant or variable with particle size, and if it changes with other particle parameters such as shape and refractive index. More extensive modelling of the expected attenuation error in this system should also be performed to better understand the divergence between predictions and observations at large particle sizes.

Furthermore, future implementations of this transmissometer would benefit from reducing the alignment sensitivity of the device. For future study, a more rigid set-up is recommended, both for future laboratory work and any in-situ applications. For example, a cage-mounted optical set-up would be less prone to changes in the angles and positions of optics. If this device were to succeed as an in-situ sensor, it would be necessary to make changes to the geometry and set-up to ensure robustness of alignment to noise, a set-up geometry that can be encased to withstand high pressures, and real-time calculations of attenuation based on a known reference value. Along these lines, any next-generation laboratory designs should also think about reducing the spatial area covered by the sensor optics, as reducing the overall surface area of the device is important for reducing the force on in-situ sensors at high pressures. One way to reduce this area would be to consider the use of a transmissive rather than reflective diffraction grating, although there would still need to be sufficient separation between the diffraction orders to make accurate attenuation measurements. The components of the sensor can also be affected by strong temperature differentials via changes to detector responsivity, changes to optical alignment, changes to the performance of electronics, and laser power changes with fluctuating temperatures. This is a known problem in beam attenuation sensors and companies like Sea Tech and Sea-Bird Scientific have implemented correction techniques in their own devices such as implementing temperature corrections or compensating for the change in electronics (Boss et al., 2019). In future versions of this work, the sensitivity of all components of the sensor to temperature changes should first be evaluated alongside any changes in attenuation measurements as a function of temperature. Following this, similar considerations to that of Sea Tech or Sea-Bird Scientific should be implemented in any in-situ iteration of this device.

Finally, the work of this thesis has highlighted the significance of spatial coherence degradation in measurements of IOPs in marine settings. Not only can degradation in spatial coherence be measured to provide more information regarding processes such as scattering and attenuation, as performed in this thesis, but constructive interference phenomena can also arise and result in enhancements in the scattering signal at certain directions. In general, it is important for researchers to understand the coherent behaviour of scattering of electromagnetic fields, rather than simply relying on the ballistic photon approach, and to consider if coherent effects are applicable in their scenario, to allow for the most accurate light signal measurements.

Bibliography

Aas, E. (1996). Refractive index of phytoplankton derived from its metabolite composition. *Journal of Plankton Research*, *18*(12), 2223–2249. https://doi.org/10.1093/plankt/18.12.2223

Ackleson, S. G., Robins, D. B., & Stephens, J. A. (1988). *Distributions In Phytoplankton Refractive Index And Size Within The North Sea* (M. A. Blizard, Ed.; p. 317). https://doi.org/10.1117/12.945739

Adams, C. S., & Hughes, I. G. (2018). Two waves: Interference. In C. S. Adams & I. G. Hughes, *Optics f2f* (1st ed., pp. 33–50). Oxford University PressOxford. https://doi.org/10.1093/oso/9780198786788.003.0003

Agrawal, Y. C., & Mikkelsen, O. A. (2009). Empirical forward scattering phase functions from 008 to 16 deg for randomly shaped terrigenous 1-21 μm sediment grains. *Optics Express*, *17*(11), 8805. https://doi.org/10.1364/OE.17.008805

Allen, L., Beijersbergen, M. W., Spreeuw, R. J. C., & Woerdman, J. P. (1992). Orbital angular momentum of light and the transformation of Laguerre-Gaussian laser modes. *Physical Review A*, *45*(11), 8185–8189. https://doi.org/10.1103/PhysRevA.45.8185

Alley, A., Laux, A., & Mullen, L. (2018). An optical vortex transmissometer. In W. “Will” Hou, R. A. Arnone, & B. Cochenour (Eds.), *Ocean Sensing and Monitoring X* (p. 29). SPIE. https://doi.org/10.1117/12.2305500

Anagnostou, C. L., Kostianoy, A. G., Mariolakos, I. D., Panayotidis, P., Soilemezidou, M., & Tsaltas, G. (Eds.). (2024). *The Aegean Sea Environment: The Geodiversity of the Natural System* (Vol. 127). Springer International Publishing. https://doi.org/10.1007/978-3-031-53797-4

Astoreca, R., Doxaran, D., Ruddick, K., Rousseau, V., & Lancelot, C. (2012). Influence of suspended particle concentration, composition and size on the variability of inherent optical properties of the Southern North Sea. *Continental Shelf Research*, *35*, 117–128. https://doi.org/10.1016/j.csr.2012.01.007

Babin, M., Morel, A., Fournier-Sicre, V., Fell, F., & Stramski, D. (2003). Light scattering properties of marine particles in coastal and open ocean waters asrelated to the particle mass concentration. *Limnology and Oceanography*, *48*(2), 843–859. https://doi.org/10.4319/lo.2003.48.2.0843

Baker, E. T., & Lavelle, J. W. (1984). The effect of particle size on the light attenuation coefficient of natural suspensions. *Journal of Geophysical Research: Oceans*, *89*(C5), 8197–8203. https://doi.org/10.1029/JC089iC05p08197

Barth, H., Grisard, K., Holtsch, K., Reuter, R., & Stute, U. (1997). Polychromatic transmissometer for in situ measurements of suspended particles and gelbstoff in water. *Applied Optics*, *36*(30), 7919. https://doi.org/10.1364/AO.36.007919

Bateman, J. B., Weneck, E. J., & Eshler, D. C. (1959). Determination of particle size and concentration from spectrophotometric transmission. *Journal of Colloid Science*, *14*(3), 308–329. https://doi.org/10.1016/0095-8522(59)90055-8

Bazhenov, V. Yu., Soskin, M. S., & Vasnetsov, M. V. (1992). Screw Dislocations in Light Wavefronts. *Journal of Modern Optics*, *39*(5), 985–990. https://doi.org/10.1080/09500349214551011

Behrenfeld, M. J., & Boss, E. (2006). Beam attenuation and chlorophyll concentration as alternative optical indices of phytoplankton biomass. *Journal of Marine Research*, *64*(3), 431–451. https://doi.org/10.1357/002224006778189563

Bhandari, P. (2023, December 17). *Correlation Coefficient | Types, Formulas & Examples*. Scribbr. https://www.scribbr.co.uk/stats/correlation-coefficient-meaning/

Bickel, W. S., & Bailey, W. M. (1985). Stokes vectors, Mueller matrices, and polarized scattered light. *American Journal of Physics*, *53*(5), 468–478. https://doi.org/10.1119/1.14202

Bogucki, D. J., Domaradzki, J. A., Ecke, R. E., & Truman, C. R. (2004). Light scattering on oceanic turbulence. *Applied Optics*, *43*(30), 5662. https://doi.org/10.1364/AO.43.005662

Bohren, C., & Clothiaux, E. (2006). *Fundamentals of atmospheric radiation*. Wiley-VCH.

Bohren, C., & Huffman, D. (1983). *Absorption and scattering of light by small particles.* John Wiley & Sons.

Boss, E., Slade, W. H., Behrenfeld, M., & Dall'Olmo, G. (2009). Acceptance angle effects on the beam attenuation in the ocean. *Optics Express*, *17*(3), 1535. https://doi.org/10.1364/OE.17.001535

Boss, E., Twardowski, M., McKee, D., Cetinic, I., & Slade, W. (2019). Beam Transmission and Attenuation Coefficients: Instruments, Characterization, Field Measurements and Data Analysis Protocols. [17pp.]. *IOCCG Protocol Series, IOCCG Ocean Optics and Biogeochemistry Protocols for Satellite Ocean Colour Sensor Validation, Volume 2.0*. https://doi.org/10.25607/OBP-458

Boss, E., Twardowski, M. S., & Herring, S. (2001). Shape of the particulate beam attenuation spectrum and its inversion to obtain the shape of the particulate size distribution. *Applied Optics*, *40*(27), 4885. https://doi.org/10.1364/AO.40.004885

Brooker, G. (2003). *Modern Classical Optics*. Oxford University Press.

Chen, R., Zhou, H., Moretti, M., Wang, X., & Li, J. (2020). Orbital Angular Momentum Waves: Generation, Detection, and Emerging Applications. *IEEE Communications Surveys & Tutorials*, *22*(2), 840–868. https://doi.org/10.1109/COMST.2019.2952453

Coble, P. G., Green, S. A., Blough, N. V., & Gagosian, R. B. (1990). Characterization of dissolved organic-matter in the black-sea by fluorescence spectroscopy. *Nature*, (348), 432–435.

Bibliography

Cochenour, B., Morgan, K., Miller, K., Johnson, E., Dunn, K., & Mullen, L. (2016). Propagation of modulated optical beams carrying orbital angular momentum in turbid water. *Applied Optics*, *55*(31), C34. https://doi.org/10.1364/AO.55.000C34

Cochenour, B., Mullen, L., & Muth, J. (2010). Effect of scattering albedo on attenuation and polarization of light underwater. *Optics Letters*, *35*(12), 2088. https://doi.org/10.1364/OL.35.002088

Cochenour, B., Rodgers, L., Laux, A., Mullen, L., Morgan, K., Miller, J. K., & Johnson, E. G. (2017). *The detection of objects in a turbid underwater medium using orbital angular momentum (OAM)* (W. (Will) Hou & R. A. Arnone, Eds.; p. 1018603). https://doi.org/10.1117/12.2264626

Curtis, D. B., Meland, B., Aycibin, M., Arnold, N. P., Grassian, V. H., Yound, M. A., & Kleiber, P. B. (2008). A laboratory investigation of light scattering from representative components of mineral dust aerosol at a wavelength of 550 nm. *J. Geophys. Res.*, *113*(D08210). https://doi.org/10.1029/2007JD009387

Finkel, Z. V., & Irwin, A. J. (2001). Light absorption by phytoplankton and the filter amplification correction: Cell size and species effects. *Journal of Experimental Marine Biology and Ecology*, *259*(1), 51–61. https://doi.org/10.1016/S0022-0981(01)00225-8

Fry, E. S., Padmabandu, G. G., & Choonghoon, O. (1992). Coherent effects in forward scattering. *SPIE Ocean Optics XI*, *1750*, 170–177.

Häfker, N. S., Connan-McGinty, S., Hobbs, L., McKee, D., Cohen, J. H., & Last, K. S. (2022). Animal behavior is central in shaping the realized diel light niche. *Communications Biology*, *5*(1), 562. https://doi.org/10.1038/s42003-022-03472-z

Hughes, I. G., & Hase, T. (2010). *Measurements and their uncertainties: A practical guide to modern error analysis*. Oxford University Press.

Jerlov, N. G. (1957). A Transparency-Meter for Ocean Water. *Tellus 9.2.*, 229–233.

Kidder, S. Q., & Vonder Haar, T. H. (1995). Radiative Transfer. In *Satellite meteorology: An introduction*. Gulf Professional Publishing.

Koestner, D., Stramski, D., & Reynolds, R. (2018). Measurements of the Volume Scattering Function and the Degree of Linear Polarization of Light Scattered by Contrasting Natural Assemblages of Marine Particles. *Applied Sciences*, *8*(12), 2690. https://doi.org/10.3390/app8122690

Koestner, D., Stramski, D., & Reynolds, R. A. (2020). Polarized light scattering measurements as a means to characterize particle size and composition of natural assemblages of marine particles. *Applied Optics*, *59*(27), 8314. https://doi.org/10.1364/AO.396709

Koestner, D., Stramski, D., & Reynolds, R. A. (2022). A Multivariable Empirical Algorithm for Estimating Particulate Organic Carbon Concentration in Marine Environments From Optical Backscattering and Chlorophyll-a Measurements. *Frontiers in Marine Science*, *9*, 941950. https://doi.org/10.3389/fmars.2022.941950

Lefering, I., Röttgers, R., Utschig, C., Twardowski, M. S., & McKee, D. (2018). Measurement uncertainties in PSICAM and reflective tube absorption meters. *Optics Express*, *26*(19), 24384. https://doi.org/10.1364/OE.26.024384

Lefering, I., Röttgers, R., Weeks, R., Connor, D., Utschig, C., Heymann, K., & McKee, D. (2016). Improved determination of particulate absorption from combined filter pad and PSICAM measurements. *Optics Express*, *24*(22), 24805. https://doi.org/10.1364/OE.24.024805

Li, X., Wang, X., Yi, Y., Zhou, Y., Chen, Q., Wang, A., Mao, S., & Yan, Y. (2023). Separation of coherent and incoherent light by using optical vortex via spatial mode projection. *Optics Communications*, *527*, 128986. https://doi.org/10.1016/j.optcom.2022.128986

MacCallum, I. (2000). *Measurement and modelling of phytoplankton light scattering* [PhD Thesis]. University of Strathclyde.

Maurer, C., Jesacher, A., Fürhapter, S., Bernet, S., & Ritsch-Marte, M. (2007). Tailoring of arbitrary optical vector beams. *New Journal of Physics*, *9*(3), 78–78. https://doi.org/10.1088/1367-2630/9/3/078

McKee, D., Piskozub, J., Röttgers, R., & Reynolds, R. A. (2013). Evaluation and Improvement of an Iterative Scattering Correction Scheme for in situ Absorption and Attenuation Measurements. *Journal of Atmospheric and Oceanic Technology*, *30*(7), 1527–1541. https://doi.org/10.1175/JTECH-D-12-00150.1

Mishchenko, M. I. (2002). Vector radiative transfer equation for arbitrarily shaped and arbitrarily oriented particles: A microphysical derivation from statistical electromagnetics. *Applied Optics*, *41*(33), 7114. https://doi.org/10.1364/AO.41.007114

Mishchenko, M. I. (2008). Multiple scattering, radiative transfer, and weak localization in discrete random media: Unified microphysical approach. *Reviews of Geophysics*, *46*(2), 2007RG000230. https://doi.org/10.1029/2007RG000230

Mishchenko, M. I. (2009). Gustav Mie and the fundamental concept of electromagnetic scattering by particles: A perspective. *Journal of Quantitative Spectroscopy and Radiative Transfer*, *110*(14–16), 1210–1222. https://doi.org/10.1016/j.jqsrt.2009.02.002

Mishchenko, M. I., Liu, L., Mackowski, D. W., Cairns, B., & Videen, G. (2007). Multiple scattering by random particulate media: Exact 3D results. *Optics Express*, *15*(6), 2822. https://doi.org/10.1364/OE.15.002822

Mobley, C. D. (1994). *Light and Water: Radiative Transfer in Natural Waters*. Academic Press.

Bibliography

Mobley, C. D. (2020, October 19). *Ocean Optics Web Book*. https://www.oceanopticsbook.info/view/introduction/overview

Mobley, C. D. (2021). The Quasi-Single-Scattering Approximation. In *Ocean Optics Web Book*. https://www.oceanopticsbook.info/view/radiative-transfer-theory/level-2/the-quasi-single-scattering-approximation#x1-62

Muinonen, K., Mishchenko, M. I., Dlugach, J. M., Zubko, E., Penttilä, A., & Videen, G. (2012). COHERENT BACKSCATTERING VERIFIED NUMERICALLY FOR A FINITE VOLUME OF SPHERICAL PARTICLES. *The Astrophysical Journal*, *760*(2), 118. https://doi.org/10.1088/0004-637X/760/2/118

Organelli, E., Dall'Olmo, G., Brewin, R. J. W., Tarran, G. A., Boss, E., & Bricaud, A. (2018). The open-ocean missing backscattering is in the structural complexity of particles. *Nature Communications*, *9*(1), 5439. https://doi.org/10.1038/s41467-018-07814-6

Parker, M. (2017). *Digital Signal Processing 101: Everything you need to know to get started*. Newnes.

Petzold, T. J. (1972). *Volume scattering functions for selected ocean waters* (Final Technical Rept. AD0753474; p. 77). SCRIPPS INSTITUTION OF OCEANOGRAPHY LA JOLLA CA VISIBILITY LAB.

Piskozub, J., & McKee, D. (2011). Effective scattering phase functions for the multiple scattering regime. *Optics Express*, *19*(5), 4786. https://doi.org/10.1364/OE.19.004786

Ren, Y., Huang, H., Xie, G., Ahmed, N., Yan, Y., Erkmen, B. I., Chandrasekaran, N., Lavery, M. P. J., Steinhoff, N. K., Tur, M., Dolinar, S., Neifeld, M., Padgett, M. J., Boyd, R. W., Shapiro, J. H., & Willner, A. E. (2013). Atmospheric turbulence effects on the performance of a free space optical link employing orbital angular momentum multiplexing. *Optics Letters*, *38*(20), 4062. https://doi.org/10.1364/OL.38.004062

Roesler, C. S. (1998). Theoretical and experimental approaches to improve the accuracy of particulate absorption coefficients derived from the quantitative filter technique. *Limnology and Oceanography*, *43*(7), 1649–1660. https://doi.org/10.4319/lo.1998.43.7.1649

Röttgers, R., McKee, D., & Woźniak, S. B. (2013). Evaluation of scatter corrections for ac-9 absorption measurements in coastal waters. *Methods in Oceanography*, *7*, 21–39. https://doi.org/10.1016/j.mio.2013.11.001

Röttgers, R., Schönfeld, W., Kipp, P.-R., & Doerffer, R. (2005). Practical test of a point-source integrating cavity absorption meter: The performance of different collector assemblies. *Applied Optics*, *44*(26), 5549–5560.

Sandven, H., Kristoffersen, A. S., Chen, Y.-C., & Hamre, B. (2020). In situ measurements of the volume scattering function with LISST-VSF and LISST-200X in extreme environments: Evaluation of instrument calibration and validity. *Optics Express*, *28*(25), 37373. https://doi.org/10.1364/OE.411177

Seabird Scientific. (2022). *Ac-s In-Situ Spectrophotometer Datasheet*. Part AC-SSPECTRALABSORPTION&ATTENUATION datasheet. https://www.seabird.com/ac-s-spectral-absorption-and-attenuation-sensor/product-downloads?id=60762467715

Sequoia Scientific. (2017, January 4). *How LISST-VSF Works*. https://www.sequoiasci.com/article/lisst-vsf-operates/

Slade, W. (2005). *fastMie* [MATLAB]. University of Maine.

Slade, W. H., Agrawal, Y. C., & Mikkelsen, O. A. (2013). Comparison of measured and theoretical scattering and polarization properties of narrow size range irregular sediment particles. *2013 OCEANS - San Diego*, 1–6. https://doi.org/10.23919/OCEANS.2013.6740987

Slade, W. H., & Boss, E. (2015). Spectral attenuation and backscattering as indicators of average particle size. *Applied Optics*, *54*(24), 7264. https://doi.org/10.1364/AO.54.007264

Slade, W. H., Boss, E., Dall'Olmo, G., Langner, M. R., Loftin, J., Behrenfeld, M. J., Roesler, C., & Westberry, T. K. (2010). Underway and Moored Methods for Improving Accuracy in Measurement of Spectral Particulate Absorption and Attenuation. *Journal of Atmospheric and Oceanic Technology*, *27*(10), 1733–1746. https://doi.org/10.1175/2010JTECHO755.1

Slade, W. H., & Boss, E. S. (2006). Calibrated near-forward volume scattering function obtained from the LISST particle sizer. *Optics Express*, *14*(8), 3602. https://doi.org/10.1364/OE.14.003602

Sullivan, J. M., & Twardowski, M. S. (2009). Angular shape of the oceanic particulate volume scattering function in the backward direction. *Applied Optics*, *48*(35), 6811. https://doi.org/10.1364/AO.48.006811

ThorLabs. (n.d.). *Gratings Tutorial*. Retrieved October 23, 2024, from https://www.thorlabs.com/newgrouppage9.cfm?objectgroup_id=8626

Tyler, G. A., & Boyd, R. W. (2009). Influence of atmospheric turbulence on the propagation of quantum states of light carrying orbital angular momentum. *Optics Letters*, *34*(2), 142. https://doi.org/10.1364/OL.34.000142

Van Der Mark, M. B., Van Albada, M. P., & Lagendijk, A. (1988). Light scattering in strongly scattering media: Multiple scattering and weak localization. *Physical Review B*, *37*(7), 3575–3592. https://doi.org/10.1103/PhysRevB.37.3575

Volten, H., De Haan, J. F., Hovenier, J. W., Schreurs, R., Vassen, W., Dekker, A. G., Hoogenboom, H. J., Charlton, F., & Wouts, R. (1998). Laboratory measurements of angular distributions of light scattered by phytoplankton and silt. *Limnology and Oceanography*, *43*(6), 1180–1197. https://doi.org/10.4319/lo.1998.43.6.1180

Voss, K. J., & Austin, R. W. (1993). Beam-attenuation measurement error due to small-angle scattering acceptance. *Journal of Atmospheric and Oceanic Technology*, *10*(1), 113–121. https://doi.org/10.1175/1520-0426(1993)010%3C0113:BAMEDT%3E2.0.CO;2

Voss, K. J., & Fry, E. S. (1984). Measurement of the Mueller matrix for ocean water. *Applied Optics*, *23*(23), 4427. https://doi.org/10.1364/AO.23.004427

Watnik, A. T., Divitt, S., & Hart, M. (2023). Separation of coherent and incoherent light using image plane vortex phase masks. *Journal of the Optical Society of America A*, *40*(7), 1372. https://doi.org/10.1364/JOSAA.489683

Wolf, P.-E., & Maret, G. (1985). Weak Localization and Coherent Backscattering of Photons in Disordered Media. *Physical Review Letters*, *55*(24), 2696–2699. https://doi.org/10.1103/PhysRevLett.55.2696

Yao, A. M., & Padgett, M. J. (2011). Orbital angular momentum: Origins, behavior and applications. *Advances in Optics and Photonics*, *3*(2), 161. https://doi.org/10.1364/AOP.3.000161

Yentsch, C. S. (1962). MEASUREMENT OF VISIBLE LIGHT ABSORPTION BY PARTICULATE MATTER IN THE OCEAN1. *Limnology and Oceanography*, *7*(2), 207–217. https://doi.org/10.4319/lo.1962.7.2.0207

Young, T. (1804). I. The Bakerian Lecture. Experiments and calculations relative to physical optics. *Philosophical Transactions of the Royal Society of London*, *94*, 1–16. https://doi.org/10.1098/rstl.1804.0001

Zhang, X., Lewis, M., & Johnson, B. (1998). Influence of bubbles on scattering of light in the ocean. *Applied Optics*, *37*(27), 6525. https://doi.org/10.1364/AO.37.006525

Zhang, X., Lewis, M., Lee, M., Johnson, B., & Korotaev, G. (2002). The volume scattering function of natural bubble populations. *Limnology and Oceanography*, *47*(5), 1273–1282. https://doi.org/10.4319/lo.2002.47.5.1273

Zhang, Y., Wang, Y., Huang, A., & Hu, X. (2019). Effect of underwater suspended particles on the transmission characteristics of polarized lasers. *Journal of the Optical Society of America A*, *36*(1), 61. https://doi.org/10.1364/JOSAA.36.000061

Appendix A: Beam images during initial transmissometry set-up

During the initial transmissometer set-up described in Chapter 3, a CMOS camera was placed at the 0th order mode position of the diffraction grating in order to approximately monitor the beam alignment via the changing beam position on the camera. Some example images of the beam profile are included below, to demonstrate the beam quality after propagation through the cuvette.

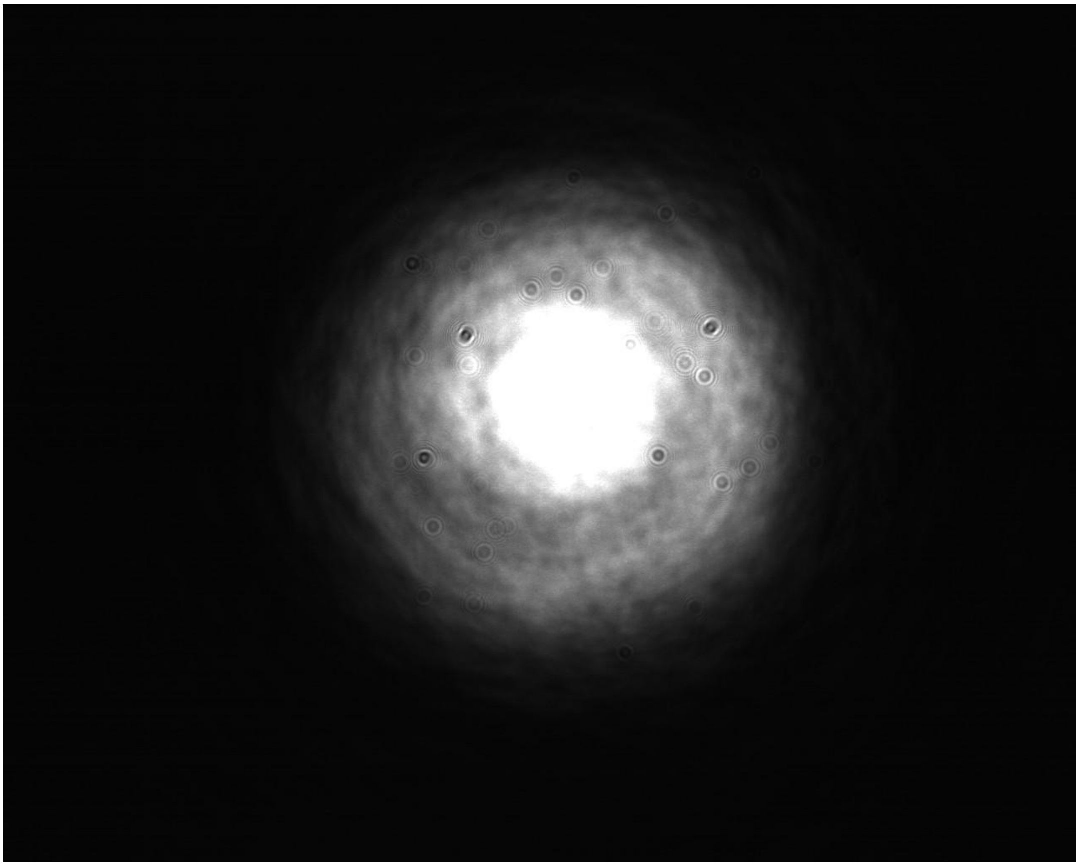

Figure A 1: Beam imaged at the 0th diffraction order after the beam has passed through a 10cm cuvette filled with Milli-Q.

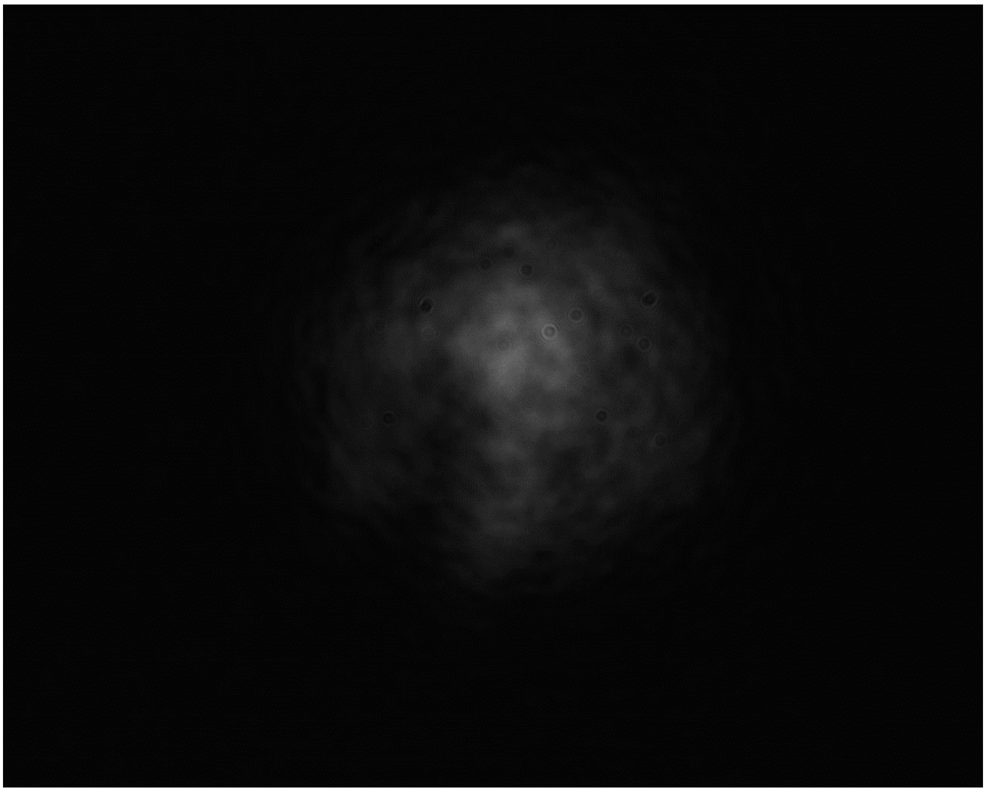

Figure A 2: Beam imaged at the 0th diffraction order after passing through a 10 cm cuvette filled with Thalassiosira sp. *at an attenuation of c = 12.3 m^{-1}, as measured by the standard lens-and-pinhole transmissometer.*

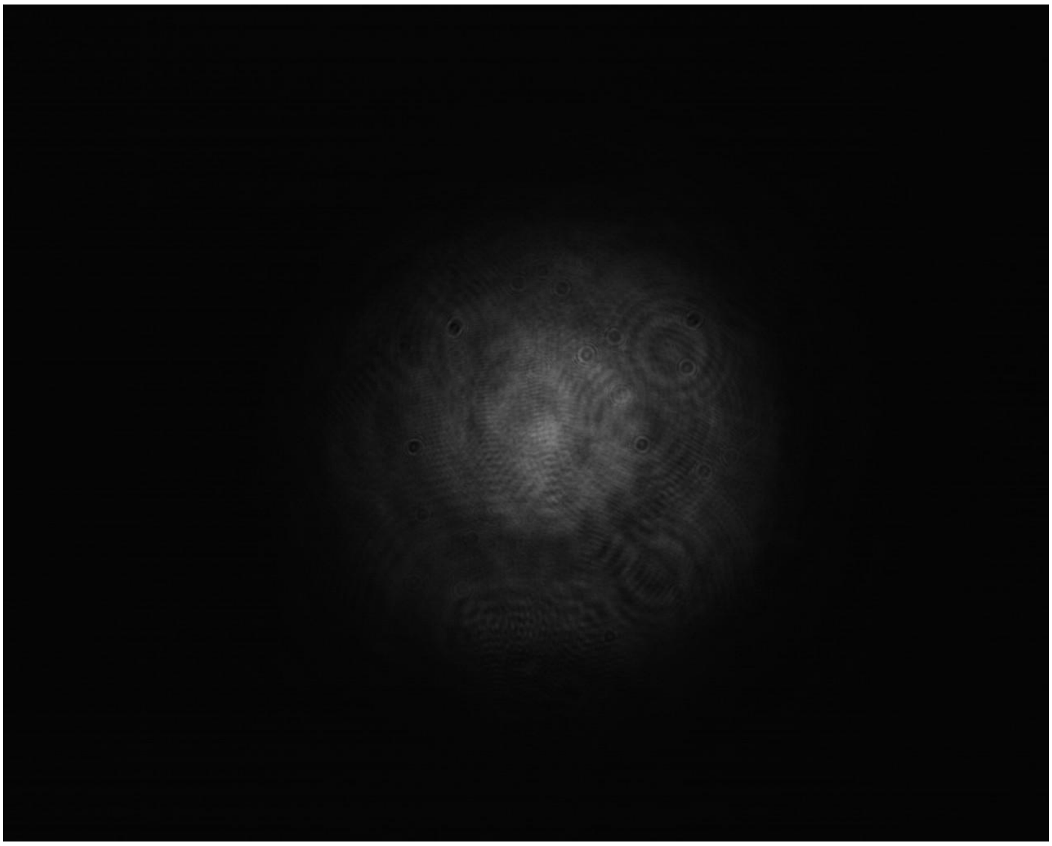

Figure A 3: Beam imaged at the 0th diffraction order after passing through a 10 cm cuvette filled with Equate-brand liquid antacid at an attenuation of c = 11.8 m-1, as measured by the standard lens-and-pinhole transmissometer.

After the beam passes through the cuvette filled with Milli-Q (Figure A1), the intensity of the beam imaged at the 0^{th} diffraction order is strong and is concentrated in the centre of the beam. For the image of the beam after passing through the liquid antacid sample (Figure A3), the intensity is lower due to the higher attenuation of the sample but the intensity is still primarily concentrated in the centre of the beam. On the other hand, for the beam that has passed through the *Thalassiosira sp*. sample of a similar attenuation (Figure A2), the profile is partially distorted with some vertical structures appearing in the beam. The exact cause of these structures are unknown but could potentially be caused by greater aggregation of the biological samples compared to the antacid.